

Measurement of the Proton Structure Function $FL(x, Q^2)$ with the H1 Detector at HERA

DISSERTATION

zur Erlangung des akademischen Grades

Dr. Rer. Nat.
im Fach Physik

eingereicht an der
Mathematisch-Naturwissenschaftlichen Fakultät I
Humboldt-Universität zu Berlin

von

M.Sc. Sebastian Piec
geboren am 24.09.1981 in Zawiercie

Präsident der Humboldt-Universität zu Berlin:
Prof. Dr. Christoph Marksches

Dekan der Mathematisch-Naturwissenschaftlichen Fakultät I:
Prof. Dr. Lutz-Helmut Schön

Gutachter:

1. Prof. Dr. Hermann Kolanoski
2. Prof. Dr. Max Klein
3. Dr. Alexander Glazov

eingereicht am: Juli 2009

Tag der mündlichen Prüfung: 6. November 2009

Abstract

A measurement of the inclusive cross section for the deep-inelastic scattering of positrons on protons at low four-momentum transfer squared Q^2 is presented. The measurement is used for the extraction of the longitudinal proton structure function F_L . The analysis is based on data collected by the H1 experiment during special, low energy runs in the year 2007. The direct technique of the F_L determination based on the extraction of the reduced DIS cross sections for three different centre-of-mass energies is used.

For the purpose of the analysis a dedicated electron finder has been developed and integrated with the standard H1 reconstruction software H1REC. The algorithm employs information from two independent tracking detectors the Backward Silicon Tracker and the Central Jet Chamber. The performance of the finder is studied.

The thesis presents the cross section and the F_L measurements in the range of $2.5 \text{ GeV}^2 \leq Q^2 \leq 25 \text{ GeV}^2$.

Zusammenfassung

In dieser Arbeit wird eine Messung des inklusiven tief-inelastischen Positron-Proton Wirkungsquerschnitts bei kleinen Impulsüberträgen Q^2 vorgestellt. Die Messung wird zur Bestimmung der longitudinalen Protonstrukturfunktion F_L benutzt. Es werden Daten analysiert, welche mit dem H1 Detektor in speziellen Perioden mit reduzierter Protonstrahlenergie im Jahre 2007 aufgezeichnet wurden. Die direkte Bestimmung der Strukturfunktion F_L basiert auf der Messung des reduzierten tief-inelastischen Wirkungsquerschnitt bei drei verschiedenen Schwerpunktsenergien.

Ein spezieller Rekonstruktionsalgorithmus für Elektronen wurde entwickelt, welcher die Informationen der zentralen Spurkammer CJC und des Siliziumdetektors BST kombiniert. Dieser wurde in die H1 Rekonstruktionssoftware H1REC integriert. Die Effizienz des Algorithmus wird untersucht.

Die Arbeit präsentiert den Wirkungsquerschnitt und die F_L Messung für Inelastizitäten im Bereich von $2.5 \text{ GeV}^2 < Q^2 < 25 \text{ GeV}^2$.

Contents

1	Introduction	1
2	Theoretical Overview of DIS	5
2.1	Kinematics of Events	5
2.2	DIS Cross Section	7
2.3	Quark Parton Model	8
2.4	Quantum Chromodynamics	9
2.5	QCD evolution	10
2.6	Radiative e-p Scattering	13
2.7	Longitudinal Proton Structure Function	14
3	The HERA Accelerator and the H1 Detector	17
3.1	HERA Accelerator	17
3.2	Detector Overview	19
3.2.1	Tracking Detectors	19
3.2.2	Calorimeters	23
3.2.3	Luminosity Measurement	24
3.2.4	Trigger System	25
3.3	SpaCal Calorimeter	26
3.4	Central Jet Chamber	27
3.5	Backward Silicon Tracker	29
4	Cross Section Measurement	37
4.1	Reconstruction of the Event Kinematics	37
4.2	Monte Carlo Simulation	41
4.3	Electron Identification	42
4.4	Background Identification and Subtraction	44
4.4.1	Charge Asymmetry	45
4.5	Cross Section Determination	46
4.5.1	Bin Selection	48
5	Data Selection and Treatment	53
5.1	Data Samples	53
5.2	Run Selection	55
5.3	Stability Studies	56
5.4	Online Event Selection	57
5.4.1	Subtrigger Definition	57

Contents

5.4.2	Trigger Efficiency	58
5.5	Alignment	59
5.5.1	SpaCal Alignment Check	60
5.6	DIS Event Selection	61
5.6.1	Cluster Reconstruction in the SpaCal	62
5.6.2	Event Vertex	64
5.6.3	Hadronic Final State	67
5.6.4	Fiducial Cuts	68
5.7	Track Linking Efficiency	69
5.8	Cross Section Results	71
5.8.1	Control Distributions	71
5.8.2	Uncertainties	71
5.9	FL(x,Q ²) Determination	73
6	Summary	85
	Tables of the Experimental Results	87
	Combined BST and CJC Electron Finder	93
1	Motivation	93
2	Description of the Algorithm	93
3	Implementation	95
4	Results and Comparisons	97

1 Introduction

One of the fundamental questions asked by humans is about the origin and structure of matter. Already ancient Greek philosophers suspected that every structure in the world consists of smaller elements. It was Empedocles who introduced four ultimate elements which make up the matter in the universe: air, earth, fire and water. Later on Democritus established the concept of the atom – small invisible particles which were the main constituent of the matter. Although most of early predictions occurred to be wrong, they formed a basis for theories developed centuries later.

Until the sixties it was believed that the universe is composed of three elementary particles: the electron, neutron and proton. However, in 1969 the first results on Deep Inelastic Scattering (DIS) at SLAC were published, changing this picture. The striking feature of the first DIS data was that the structure function F_2 , which parametrizes the structure of the proton seemed to be independent on the resolution power of the electron, i.e. Q^2 . A simple physical interpretation of this result was proposed by Feynman in the parton model. According to this model the proton is assumed to consist of non-interacting, point-like constituents (partons). Since the scattering center is a point one does not expect dependence of F_2 on Q^2 . The function depends only on the fraction of the proton momentum carried by the struck parton, so-called Bjorken x variable. In 1969 Bjorken and Paschos proposed the quark parton model, identifying partons as quarks – particles introduced by Gell-Mann and Zweig to explain the large number of mesons and baryons.

Although the quark parton model was able to successfully explain early DIS observations, many difficulties arose soon. It was observed in neutrino-nucleon experiments that the quarks carry only about half of the nucleon's momentum, which was evidence for the existence of additional constituents in the nucleon, which do not interact with the leptons. Moreover partons were never observed in the final state, which implied strong forces between them. On the other hand the quark parton model assumed no interaction between nucleon's constituents. Both problems were solved with the development of the theory of strong interactions Quantum Chromodynamics (QCD). The theory describes interactions between the quarks via exchange of gluons, particles which carry the missing momentum of the proton. Due to the non-Abelian structure of QCD the strength of the interaction between the quarks decreases towards small distance, which corresponds to large Q^2 . This behaviour is called asymptotic freedom. At large distances (small Q^2) the strength of the interaction rises and the so-called confinement of the quarks is observed.

The theory which unifies QCD with the theory of electroweak interactions is called the Standard Model. The model describes the elementary particles and fundamental interactions between them. In our present knowledge the most fundamental building blocks of the matter are two types of fermions, the leptons and the quarks. Three

1 Introduction

generations of leptons are distinguished: the electron (e) and the electron neutrino (ν_e), the muon (μ) and the muon neutrino (ν_μ), and the tau (τ) and the tau neutrino (ν_τ). Similarly the quarks belong to three groups: up (u) and down (d), strange (s) and charm (c), bottom (b) and top (t).

The interactions between all particles are mediated via the exchange of gauge bosons. Currently four types of interaction are known, these are gravitational, electromagnetic, weak and strong forces. Gravitation is too weak to influence interactions of elementary particles. The electromagnetic interaction involves the photon. The weak interaction is mediated by the gauge bosons Z^0 and W^\pm . Finally the strong interaction involves the gluons g . Each type of interaction is associated with a charge. Three leptons e , μ and τ as well as quarks are electrically charged, in addition all leptons and quarks carry a weak charge. Colour charge is characteristic for the strong interaction and is carried by the quarks and gluons.

In this thesis the direct measurement of the structure function $F_L(x, Q^2)$ in the low Q^2 region of the kinematics phase space is presented. As depicted in subsection 2.7 at low Q^2 and in the low x region of phase space the gluon contribution to F_L greatly exceeds the quark contribution. Thus the measurement of the longitudinal proton structure function is, to a very good approximation, the measure of gluon density in the proton. The precise knowledge of the gluon density for $x \approx 0.005$, corresponding for HERA kinematics to $Q^2 > 10 \text{ GeV}^2$ range, is used for prediction of W , Z as well as light Higgs production rates at the LHC. The measurements for $2.5 \text{ GeV}^2 \leq Q^2 \leq 8.5 \text{ GeV}^2$ access the region where the higher order QCD corrections become large and various models give different predictions

The model dependent technique used for the determination of the structure function F_L is based on the measurement of the reduced cross section for high y , and on assumptions on behaviour of the proton structure function F_2 . The direct determination assumes that for fixed x , Q^2 and y the DIS cross section has linear dependence on the structure functions F_2 and F_L . Therefore the measurement of F_L performed in this thesis is based on an extraction of the reduced DIS cross section, for given x and Q^2 , varying y . Having measured at least two cross sections for the same x and Q^2 , the straight line fit as a function of y can be performed. The slope of the fit is attributed to F_L , while the intercept to F_2 . The variation of variable y has been achieved by variation of the center of mass energy in special low energy runs in the year 2007.

The thesis is organised as follows:

- In chapter 2 a theoretical overview of DIS interactions is given. The double-differential cross section of neutral current scattering, basics of the theory of strong interactions (QCD), evolution equations and fundamentals of the measurement of the structure function $F_L(x, Q^2)$ are discussed.
- Chapter 3 presents the HERA collider and the H1 experiment, with particular attention paid to components relevant for this analysis.
- In chapter 4 the basics of the cross section measurement, including reconstruction of the kinematics, electron and background identification, as well as the bin

definition, are explained.

- Chapter 5 presents the identification and reconstruction of DIS events. Discussion on detector alignment, efficiency determination and results of the cross section and $F_L(x, Q^2)$ structure function measurements, is presented.
- Results of this thesis are summarized in chapter 6.

The thesis has two appendices devoted to the tables of the experimental results and to the combined electron reconstruction module BCREC, exploiting information from two independent tracking detectors.

2 Theoretical Overview of DIS

The scattering of a high energy lepton off a hadron with a large absolute momentum transfer, leading to a multihadronic final state, is called Deep Inelastic Scattering (DIS). DIS is the main tool to probe the inside of a hadron, and has therefore played an important role in the development of the theory of strong interactions, Quantum Chromodynamics.

In this thesis, discussion of DIS will be limited to electron-proton scattering, since this is the case for the HERA accelerator. The term 'electron' will be also used to denote positron, unless otherwise stated.

2.1 Kinematics of Events

The interaction of an electron with a proton is described in perturbative QCD via the exchange of virtual gauge bosons. In general, two different processes, depending on the intermediate particle, can take place. For Neutral Current (NC) events, a neutral gauge boson: photon (γ) or Z^0 is scattered off the proton producing a hadronic final state, X . For Charge Current (CC) events the gauge boson carries a charge (W^\pm) and the result of the interaction in this case is the hadronic final state and a (typically undetected) neutrino.

Since in the kinematic range considered, the cross section for processes with heavy boson exchange (W^\pm/Z^0) is negligible with respect to NC γ processes (see section 2.2), the former will not be discussed further.

The Feynman diagram of deep-inelastic electron-proton scattering with a single photon exchange is shown in figure 2.1. Here, the variable k (k') corresponds to the four-momentum of the incident (outgoing) electron. The four-momentum of the incoming proton is denoted by the variable P .

The kinematics of the DIS process is most conveniently described by the following three Lorentz invariant quantities:

- The absolute squared four-momentum transfer Q^2 :

$$Q^2 = -q^2 = -(k - k')^2 > 0, \quad (2.1)$$

representing the virtuality of the exchanged boson.

- The inelasticity y :

$$y = \frac{q \cdot P}{k \cdot P}, \quad (2.2)$$

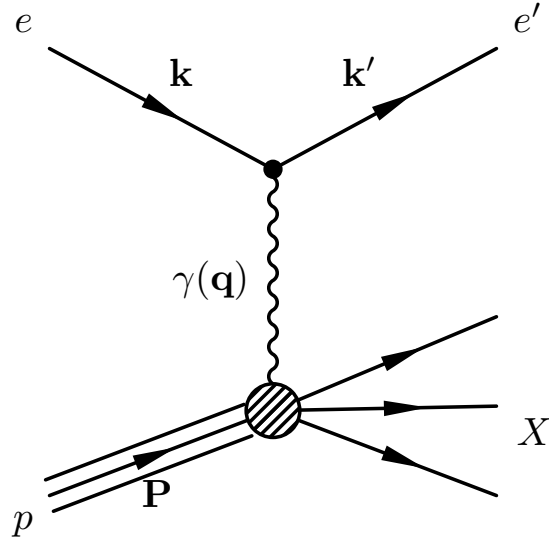


Figure 2.1: Lowest order Feynman diagram describing deep-inelastic electron-proton scattering and four-momenta assigned to the interacting particles.

corresponding, in the proton rest frame, to the fraction of the incident electron energy carried by the exchanged boson.

- The Bjorken variable x [9]:

$$x = \frac{Q^2}{2P \cdot q}, \quad (2.3)$$

which is the fraction of the nucleon momentum carried by the struck quark.

By definition, both Bjorken x and y variables are dimensionless and limited to the range $(0, 1)$.

For the kinematic variables the following approximate relation holds:

$$Q^2 = sxy, \quad (2.4)$$

where s is the square of the center of mass energy defined as $s = (k + p)^2$. Neglecting the particle masses, this can be evaluated as $s = 4E_e E_p$, where E_e (E_p) is the energy of the electron (proton) beam.

A further commonly used quantity is the center of mass energy of the intermediate boson-proton system:

$$W^2 = Q^2 \left(\frac{1}{x} - 1 \right) + m_p^2 \approx Q^2 \left(\frac{1}{x} - 1 \right) = sy - Q^2 = sy(1 - x), \quad (2.5)$$

where m_p denotes mass of the proton. One can see that the factor m_p can be safely neglected, since its value is insignificant w.r.t. the energy scale set by the HERA collider, $m_p \ll \sqrt{s}$.

The DIS kinematic region is defined by a four-momentum transfer $Q^2 > 1 \text{ GeV}^2$ and $W > 2 \text{ GeV}$. In the limit $Q^2 \rightarrow 0$, the electron-proton scattering process can be interpreted as an interaction of a real photon with a proton. This regime defines so-called photoproduction.

2.2 DIS Cross Section

The cross section for the DIS process can be expressed in terms of a tensor product:

$$\sigma \sim L_{\alpha\beta} W^{\alpha\beta}, \quad (2.6)$$

where $L_{\alpha\beta}$ denotes the leptonic tensor, describing the interaction of the electron with the virtual exchange boson and can be precisely calculated in electroweak theory. The interaction of the gauge boson with the proton is represented by the hadronic tensor, $W^{\alpha\beta}$. In contrast to the leptonic tensor, the form of $W^{\alpha\beta}$ is not completely known. However, using Lorentz invariance and current conservation, it can be expressed in terms of two functions related to the structure of the proton, by convention denoted $F_2(x, Q^2)$ and $F_L(x, Q^2)$.

The inclusive neutral current $e^\pm p$ double-differential cross section at low values of Q^2 , in the one-photon exchange approximation, can be then written as:

$$\frac{d^2\sigma}{dx dQ^2} = \frac{2\pi\alpha^2 Y_+}{xQ^4} \left(F_2(x, Q^2) - \frac{y^2}{Y_+} F_L(x, Q^2) \right), \quad (2.7)$$

where α is the fine structure constant and Y_+ is defined as:

$$Y_+ = 1 + (1 - y)^2. \quad (2.8)$$

From formula 2.7 one can immediately see that the dominant fraction of DIS events is observed for relatively low values of Q^2 , due to the factor $1/Q^4$. It is also obvious that for $Q^2 \ll M_{Z^0}^2, M_{W^\pm}^2$ contributions from Z^0 and W^\pm exchange can be neglected. Finally, from 2.7, it is clear that simultaneous measurement of both structure functions is only possible if the inelasticity y is varied, while values of x and Q^2 stay fixed. This requires a variation of the center of mass energy, \sqrt{s} , which technically can be achieved by changing the beam energies of the HERA collider (for details see section 2.7).

From the experimental point-of-view, it is convenient to omit the kinematic factor $2\pi\alpha^2 Y_+ / xQ^4$ and define the so-called reduced cross section, σ_r :

$$\sigma_r = F_2(x, Q^2) - \frac{y^2}{Y_+} F_L(x, Q^2). \quad (2.9)$$

The ep scattering process is often considered as the interaction of a flux of virtual photons with the proton [23]. The differential ep cross section can be then rewritten as:

$$\frac{d^2\sigma}{dx dQ^2} = \Gamma(y, Q^2) (\sigma_T(x, Q^2) + \epsilon(y)\sigma_L(x, Q^2)), \quad (2.10)$$

2 Theoretical Overview of DIS

where $\Gamma(y, Q^2) = Y_+ \alpha / (2\pi Q^2 x)$ denotes the flux factor, $\epsilon(y) = 2(1-y)/Y_+$ corresponds to the photon polarisation and σ_T, σ_L denote the absorption cross sections for the transversely and longitudinally polarised photons, respectively.

Comparing equations 2.7 and 2.10 one obtains the following relations of the cross sections to the structure functions:

$$F_2(x, Q^2) = \frac{Q^2}{4\pi^2\alpha} (\sigma_T(x, Q^2) + \sigma_L(x, Q^2)), \quad (2.11)$$

$$F_L(x, Q^2) = \frac{Q^2}{4\pi^2\alpha} \sigma_L(x, Q^2). \quad (2.12)$$

As can be seen from the above equations, $F_2(x, Q^2)$ contains contributions from both the longitudinally and transversally polarized photons, while the longitudinal proton structure function, $F_L(x, Q^2)$, is proportional to the absorption cross section of longitudinally polarized virtual photons only. Finally positivity of the cross sections σ_L and σ_T enforces the relation:

$$0 \leq F_L(x, Q^2) \leq F_2(x, Q^2). \quad (2.13)$$

Since the contribution of the longitudinal structure function to the DIS cross section is proportional to the factor y^2 , its value is sizeable only at very high values of inelasticity y . Thus, most of the DIS experimental data are interpreted as a measurement of the structure function $F_2(x, Q^2)$.

2.3 Quark Parton Model

The Quark Parton Model (QPM) was proposed by Feynman [16] in 1969 and was the first approach to interpret the data provided by early DIS experiments. In the QPM the proton is viewed from a frame in which it has infinite momentum and is assumed to consist of quasifree point-like particles called *partons*. In such a frame, the transverse momenta of the partons can be neglected. Thus, each constituent carries only longitudinal momentum $p' = \eta p$, which is a fraction of the total longitudinal momentum p of the proton.

The interaction of the electron and proton is interpreted in the QPM as an elastic scattering of the electron on one of the partons. The double differential ep cross-section can be then expressed as an incoherent sum over all such processes:

$$\frac{d^2\sigma}{dx dQ^2} = \sum_i \int_0^1 d\xi q_i(\xi) \left(\frac{d^2\sigma}{dx dQ^2} \right)_{eq_i \rightarrow eq_i}, \quad (2.14)$$

where $q_i(\xi)$ is called the *parton density function* and denotes the probability to find a parton i carrying the fraction ξ of the proton's momentum, before the interaction.

Such an approach to the problem simplifies the description, since the cross-section for

the elastic electron-quark scattering is precisely calculable within QED:

$$\left(\frac{d^2\sigma}{dx dQ^2} \right)_{e q_i \rightarrow e q_i} = \frac{4\pi\alpha^2}{Q^4} e_i^2 \frac{1}{2} (1 + (1-y)^2) \delta(x - \xi). \quad (2.15)$$

Inserting 2.15 into 2.14 and comparing with 2.7 the structure functions of the proton can be written in the following form:

$$F_2(x, Q^2) = \sum_i e_i^2 x q_i(x), \quad (2.16)$$

$$F_L(x, Q^2) = 0. \quad (2.17)$$

One can immediately see that both functions are independent of Q^2 in the QPM, i.e. are scale invariant. This behavior was observed in the first DIS experiments at SLAC for $x \approx 0.25$ and was predicted by Bjorken already in 1966 [8]. According to equation 2.17, also known as the *Callan-Gross relation*, the longitudinal structure function F_L is predicted to vanish. This expectation follows from helicity and momentum conservation, which does not allow absorption of longitudinally polarized photons on massless spin- $\frac{1}{2}$ partons.

The model also predicts that the sum over parton momenta should be equal to one:

$$\sum_i \int_0^1 x (q_i(x) + \bar{q}_i(x)) = 1. \quad (2.18)$$

While QPM helped to understand basic structure of the proton and was able to explain first DIS data, most of the expectations of the model were shown not to be valid in general.

2.4 Quantum Chromodynamics

In the same year as the QPM was proposed a violation of the scaling hypothesis, i.e. a weak, logarithmic dependence of the structure function F_2 on Q^2 was observed in the SLAC experiment. Moreover, the F_L structure function seemed to be non-zero and the sum over parton momenta was determined to be only about 1/2. All these effects were successfully explained in the framework of Quantum Chromodynamics (QCD) [37], a quantum field theory describing the strong interaction between quarks via intermediate massless vector bosons called *gluons*.

QCD is a non-abelian field theory based on the $SU(3)$ symmetry group. The quarks, besides electric charge, carry so-called color charge, conventionally denoted as "red", "green" and "blue". The interaction between quarks is mediated through the exchange of gluons, carrying combinations of colors. Unlike QED, where the photons are electrically neutral, the color charge enables gluons to couple to themselves. This feature of QCD leads to an antiscreening effect from vacuum polarization. As a result, the running

2 Theoretical Overview of DIS

coupling constant α_S decreases with an increasing scale of the interaction, Q^2 . In the leading order approximation the value of the constant is given by the equation:

$$\alpha_s(Q^2) = \frac{12\pi}{(33 - 2n_f) \ln\left(\frac{Q^2}{\Lambda_{QCD}^2}\right)}, \quad (2.19)$$

where n_f denotes the number of active quark flavours, with $m_q^2 < Q^2$. Λ_{QCD} is the scale parameter characterizing the energy scale at which the coupling constant escapes to infinity.

For $Q^2 < \Lambda_{QCD}^2$, which corresponds to large distances, the coupling constant increases, leading to the *confinement* of quarks and gluons. At high $Q^2 > 1 \text{ GeV}^2$ (DIS regime), α_S becomes small, which leads to weaker coupling between quarks, i.e. they are *asymptotically free*. In this regime, perturbative QCD (pQCD) calculations, using order-by-order expansions in α_S , can be applied.

The applicability of pQCD calculations to the DIS processes follows from the factorization theorem. It states that for the general case of lepton-hadron scattering the interaction of the exchanged vector boson with the hadron can be divided into two independent parts, a "short distance" part, which can be calculated perturbatively and a "long distance" part, which should be taken from experiment. Formally, factorisation implies that the structure functions can be expressed as a convolution of coefficient functions $C_a^{V,i}$, given by pQCD for a particular exchanged boson V , parton i and a structure function a and parton distributions $f_{i/h}(z)$, corresponding to the probability to find a parton i carrying a fraction z of the hadron's momentum. For the structure function F_2 , one obtains the formula:

$$F_2^{V,h}(x, Q^2) = \sum_{i=q,\bar{q},g} \int_x^1 dz C_2^i\left(\frac{x}{z}, \frac{Q^2}{\mu_r^2}, \frac{\mu_f^2}{\mu_r^2}, \alpha_s(\mu_r^2)\right) f_i(z, \mu_r^2, \mu_f^2). \quad (2.20)$$

In equation 2.20, two scales are present: the factorization scale parameter μ_f , which defines the boundary between the short and long distance part, and μ_r , needed to absorb the ultraviolet divergences of the higher orders in pQCD, the so-called renormalization scale parameter. Both parameters can be arbitrary chosen.

By convention, two schemes are most often used: the DIS scheme and the modified minimal subtraction scheme (\overline{MS}). In the former, the structure function F_2 is given by the parton model formula 2.16 to all orders of perturbation theory. In the latter scheme, the parton density functions are defined directly in terms of the hadronic matrix elements.

2.5 QCD evolution

An important consequence of factorisation is that measuring the parton density functions at one scale μ allows their prediction for any other scale μ' . This feature of the parton densities is referred to as evolution.

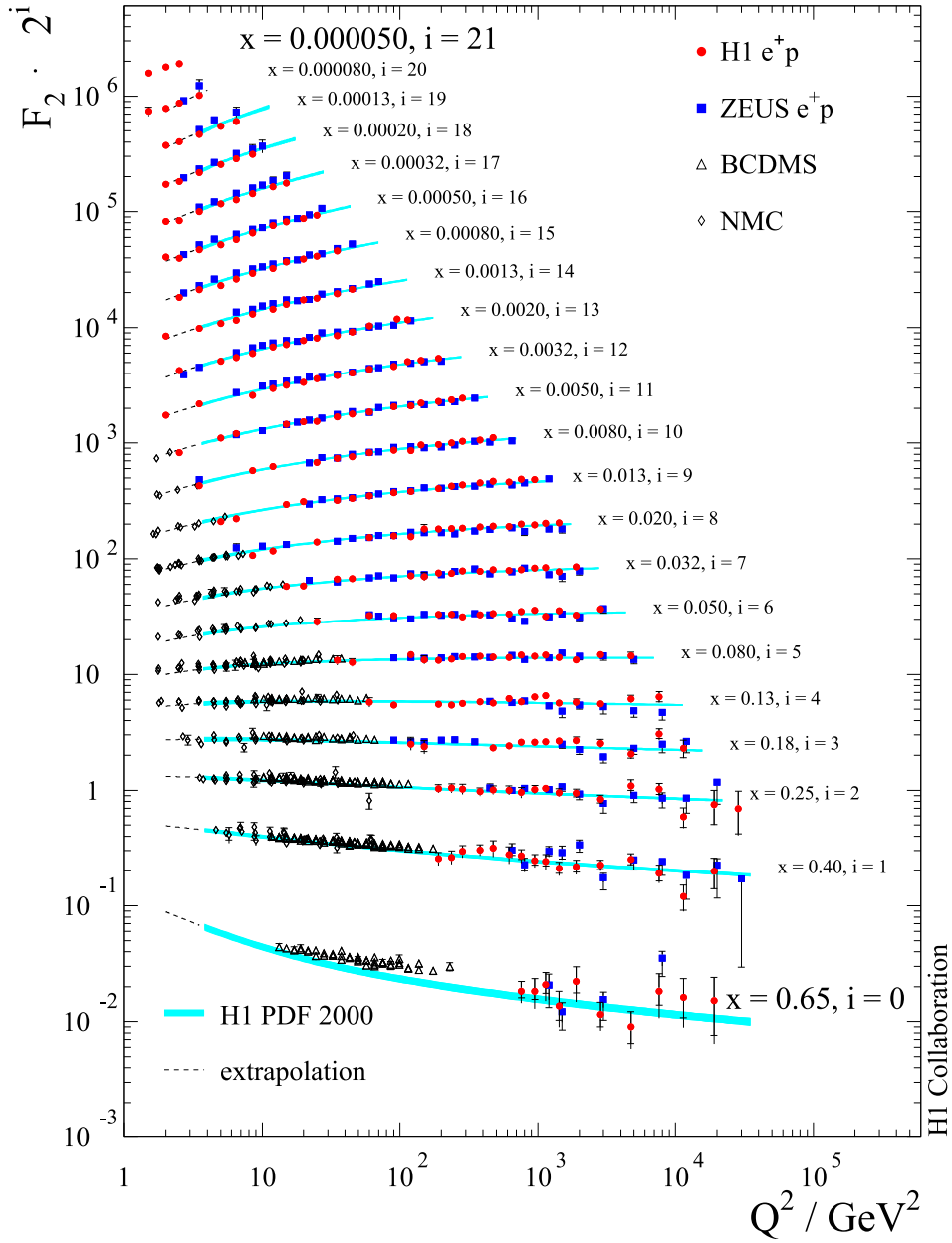


Figure 2.2: Data on F_2 from fixed target experiments and the HERA collider experiments together with a NLO QCD fit [4]. The measurements at different x are displaced vertically by a factor 2^i .

2 Theoretical Overview of DIS

The evolution equations describe how the quark and gluon distribution functions evolve with the scale. They can be derived directly from equation 2.20, exploring the structure functions independence of the factorisation and renormalization scale. Choosing $\mu_r = \mu_f = Q$ one obtains the DGLAP evolution equations, named after Dokshitzer, Gribov, Lipatov, Altarelli and Parisi [18, 13, 5]:

$$\frac{dq_i(x, Q^2)}{d \ln Q^2} = \frac{\alpha_s(Q^2)}{2\pi} \int_x^1 \frac{dz}{z} \left[\sum_j q_j(z, Q^2) P_{ij} \left(\frac{x}{z} \right) + g(z, Q^2) P_{ig} \left(\frac{x}{z} \right) \right], \quad (2.21)$$

$$\frac{dg(x, Q^2)}{d \ln Q^2} = \frac{\alpha_s(Q^2)}{2\pi} \int_x^1 \frac{dz}{z} \left[\sum_j q_j(z, Q^2) P_{gj} \left(\frac{x}{z} \right) + g(z, Q^2) P_{gg} \left(\frac{x}{z} \right) \right], \quad (2.22)$$

where $q_i(x, Q^2)$ and $g(x, Q^2)$ denote the quark and gluon density functions, respectively. The functions $P_{ij}(x/z)$ are known as the splitting functions and are calculable in pQCD as a power series of α_s :

$$P_{\alpha\beta}(z, \alpha_s) = \frac{\alpha_s}{2\pi} P_{\alpha\beta}^{(0)}(z) + \left(\frac{\alpha_s}{2\pi} \right)^2 P_{\alpha\beta}^{(1)}(z) + \dots \quad (2.23)$$

In the leading order approximation, splitting functions $P_{\alpha\beta}^{(0)}(x/z)$ describe the probability to find a parton of species i in a parton of species j with a fraction x of the longitudinal momentum of the originating parton and with transverse momentum squared much less than μ^2 . Figure 2.3 shows the graphs for all leading order splitting functions.

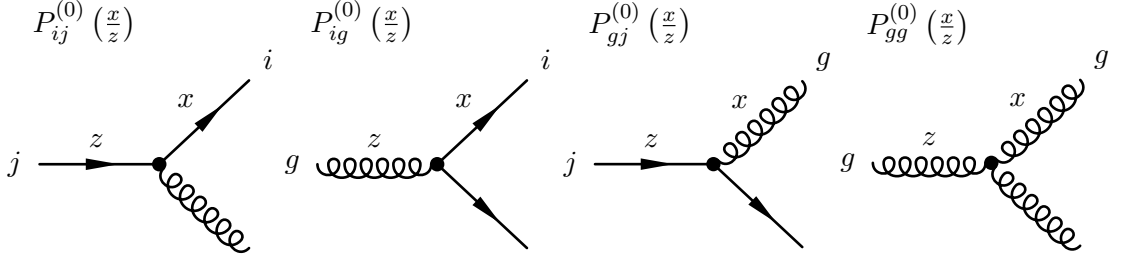


Figure 2.3: Diagrams for the lowest order splitting functions for the DGLAP equations.

Since the DGLAP approximation considers only powers of $\alpha_s \ln(Q^2/Q_0^2)$ from the perturbative QCD expansion, its predictions are only valid at large enough Q^2 where α_s is small and the $\ln(1/x)$ terms can be neglected.

Determination of the parton density functions from experimental data is performed according to the following procedure: the parton density functions are parametrised by smooth analytical functions at a low starting scale Q_0^2 as a function of x with few free parameters. The functions are evolved in Q^2 using DGLAP equations. Afterwards, predictions for the cross section (equation 2.7) and structure functions (equation 2.20) are calculated. The free parameters are determined by comparison of the calculation

with experimental data and minimisation of the χ^2 .

For the precise determination of the parton density functions the coefficient and splitting functions should be accurately known as they enter the calculation of the structure functions, see equation 2.20. Currently, most analyses of DIS data have used splitting and coefficient functions at next-to-leading order (NLO). Examples are global analyses performed by the CTEQ collaboration or the MRST group. Since 2005 the functions are known to next-to-next-to-leading order (NNLO), which should lead to better theory errors.

A set of F_2 measurements from fixed target and HERA experiments together with a fit by the H1 collaboration is shown in figure 2.2. Scaling predicted by the QPM is observed only in the region of $x \approx 0.25$ where the first SLAC measurements have been performed. At small (large) values of x , the structure function F_2 rises (decreases) with Q^2 , i.e. scaling is violated.

2.6 Radiative ep Scattering

The lowest order Feynman diagram for ep scattering is depicted in figure 2.1. The corresponding Born cross section, taking into account only the photon exchange, is given in equation 2.7. At higher orders, various radiative processes have to be considered, where the dominant contribution comes from the radiation of a real photon from the incoming or outgoing electron.

The Feynman diagrams for the photon emission from the lepton line are shown in figure 2.4. For the cross section calculation it is necessary to sum all diagrams of the respective order. The amplitudes for the considered processes are proportional to $\left((q'^2 - m_e^2)q^2\right)^{-1}$ and $\left((q''^2 - m_e^2)q^2\right)^{-1}$. Due to the structure of the amplitudes, the differential cross section exhibits maxima when one or both of these terms approaches zero. These maxima correspond to the following experimental observations:

- Initial State Radiation (ISR) or Final State Radiation (FSR) events, which are characterised by finite q^2 , but small $q'^2 \simeq 0$ or $q''^2 \simeq 0$ respectively. For ISR (FSR) events the radiated photon is emitted collinear with the incoming (scattered) electron while the virtuality $Q^2 = -q^2$ of the exchanged photon is large enough for the electron to be detected in the detector. Due to the photon radiation being before the interaction, ISR events can be interpreted as non-radiative ep scattering at a reduced centre of mass energy \sqrt{s} . This allows one to extract the structure function F_2 at lower values of Q^2 for a given x or at larger values x for a given Q^2 . For FSR events, the opening angle between the scattered electron and the radiated photon is too small for both particles to be separately reconstructed in the calorimeter. Therefore FSR events usually cannot be distinguished from non-radiative events.
- In events with $q^2 \approx 0$, but q'^2 and q''^2 finite, both the electron and photon have a sizeable transverse momentum and are almost back-to-back in the azimuthal angle.

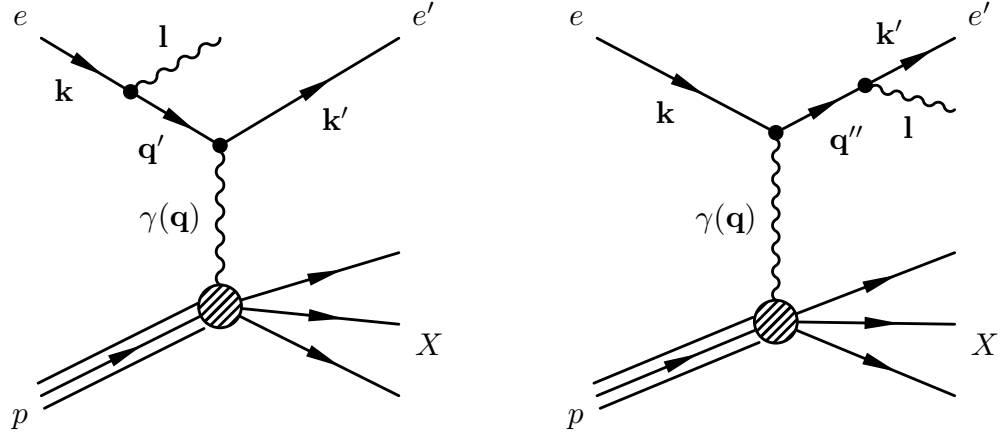


Figure 2.4: Lowest order diagrams for the process $ep \rightarrow eX\gamma$ with photon emission from the incoming and outgoing electron line, on the left and right respectively. The momenta assigned to the electron lines are labelled with \mathbf{k} , \mathbf{q}' , \mathbf{q}'' , and \mathbf{k}' respectively, the real photon has momentum \mathbf{l} , and the momentum assigned to the photon propagator is \mathbf{q} .

This process is called QED Compton Scattering (QEDC). QEDC events are rather easily identified experimentally as transverse momenta of both particles is sizeable. The back-to-back property of these events makes them particularly suitable for the detector alignments.

- Finally, the last maximum of the cross section corresponds to $q^2 \approx 0$, $q'^2 \approx 0$ and $q''^2 \approx 0$. This class of events is characterized by both the electron and radiated photon being scattered at very small angles. Hence they leave the detector without being detected. The dominant contribution comes from Bethe-Heitler events. The cross section for these events can be very precisely calculated in QED and is independent of the proton structure. For these reasons, the Bethe-Heitler process is used as a reference for the luminosity measurement in the H1 experiment, see section 3.2.3.

2.7 Longitudinal Proton Structure Function

As already pointed out in section 2.4, the longitudinal proton structure function $F_L(x, Q^2)$ is related to the γp interaction cross section of longitudinally polarised photons. While in the QPM $F_L(x, Q^2)$ is predicted to vanish, in Quantum Chromodynamics, the $F_L(x, Q^2)$ differs from zero. Due to the presence of gluons at the hadronic vertex it is possible to absorb longitudinally polarised photons and at the same time satisfy helicity and momentum conservation laws. At the next-to-leading order, F_L violates the

2.7 Longitudinal Proton Structure Function

Callan-Gross relation and takes the form:

$$F_L(x, Q^2) = \frac{\alpha_S Q^2}{4\pi} x^2 \int_x^1 \frac{dz}{z^3} \left[\frac{16}{3} F_2(z, Q^2) + 8 \sum e_q^2 \left(1 - \frac{x}{z}\right) z g(z, Q^2) \right], \quad (2.24)$$

where contributions from quarks and gluons are present.

At low x and in the Q^2 region of DIS the gluon contribution greatly exceeds the quark contribution to F_L . Therefore the function is a direct measure of the gluon distribution to a very good approximation:

$$F_L(x, Q^2) \propto x g(x, Q^2). \quad (2.25)$$

According to equation 2.7 the sensitivity to F_L is largest in the high y region of the phase space, as its contribution to the reduced cross section, σ_r , is proportional to the kinematic factor y^2/Y_+ . Since the following relation holds (see section 4.3):

$$y = 1 - \frac{E'_e}{E_e} \sin^2(\theta_e/2), \quad (2.26)$$

where E'_e and θ_e is the energy and the polar angle of the scattered electron, respectively, it is clear that at low Q^2 ($\theta_e \approx 180^\circ$), high y values correspond to low values of E'_e . However, small energy depositions can also be caused by hadronic final state particles leading to a fake electron signal, which makes the measurement of $F_L(x, Q^2)$ particularly challenging.

Indirect methods to determine F_L rely on the measurement of the reduced cross section σ_r and on assumptions on the behaviour of F_2 . Since the influence of F_L on the cross section is suppressed by the kinematic factor y^2/Y_+ , for low values of inelasticity y , σ_r is a direct measure of F_2 in this region. Having measured F_2 , a theoretical model is used to extrapolate the function to the high y region. The difference between the measured cross section and the F_2 model is attributed to F_L .

An alternative is the direct approach to determine F_L using several sets of DIS cross sections at fixed x , Q^2 and at different y . Having at least two different cross sections measured, the straight line fit can be performed:

$$\sigma_r(x, Q^2) = F_2(x, Q^2) - f(y) F_L(x, Q^2), \quad (2.27)$$

where the function $f(y) = y^2/Y_+$. The $F_L(x, Q^2)$, in this case, is extracted from the measurements of the reduced cross section as the slope of σ_r versus y^2/Y_+ , while the intercept with the y axis gives $F_2(x, Q^2)$. An illustration of the method is depicted in figure 2.5, where the reduced cross section is plotted for the three different energies.

It is clear that the precise measurement of $F_L(x, Q^2)$ requires the difference between $f(y)$ at high and low energy of the proton beams to be large, i.e. a large difference between the centre-of-mass energies is required. The precision varies as:

$$\frac{1}{f(y_{460})} \approx \frac{1}{y_{460}^2}, \quad (2.28)$$

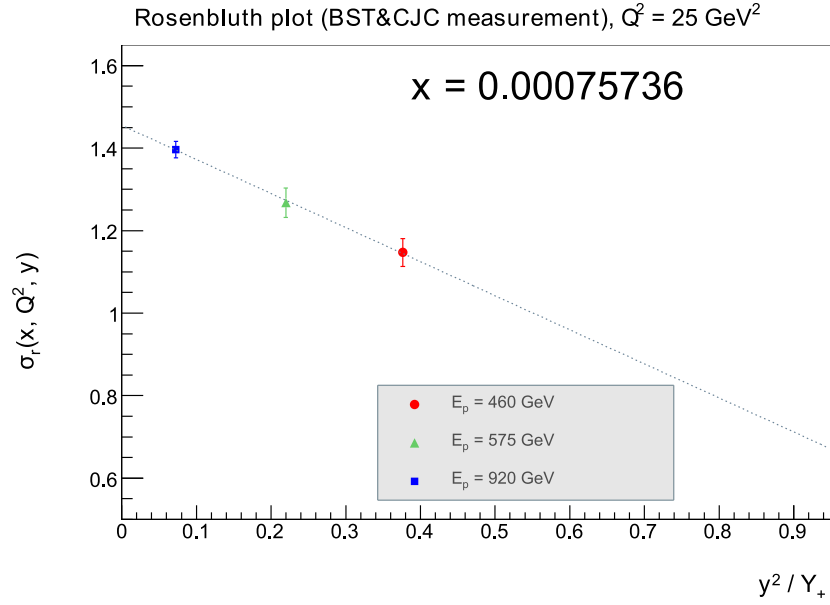


Figure 2.5: Measurement of the cross section for data at 920 GeV, 575 GeV and 460 GeV. The error bars represent statistical errors only.

where y_{460}^2 corresponds to the y value for $E_p = 460$ GeV. Thus, to reduce the error of the measurement it is necessary to reach the highest possible values of y for the lowest E_p run.

From January to June 2007, three data sets with different proton beam energies were collected. The largest energy of 920 GeV, the smallest energy of 460 GeV and an intermediate energy of 575 GeV, were used. The energies were chosen to give maximal and approximately equal span between the three resulting cross section measurements in y^2/Y_+ , while maintaining acceptable level of luminosity. For a detailed description of the data treatment and the measurement of $F_L(x, Q^2)$, see section 5.

3 The HERA Accelerator and the H1 Detector

3.1 HERA Accelerator

The HERA (Hadron-Elektron-Ring-Anlage) collider located at DESY (Deutsches Elektronen-Synchrotron) in Hamburg is the first and so far the only storage ring for electrons and protons. It started operation in 1992. Nominal beam energies are $E_e = 27.6$ GeV for the electrons and $E_p = 920$ GeV for the protons, respectively. This corresponds to a centre-of-mass energy available for electron-proton collisions of $\sqrt{s} \approx 320$ GeV, since the following approximate relation holds $s = 4E_e E_p$.

The particles in HERA are accelerated in two separate accelerator rings located in a tunnel of 6.3 km circumference (see figure 3.1). The electron ring is equipped with conducting dipole magnets at ambient temperature having a maximum field strength of 0.17 T. For the proton ring superconducting dipole magnets are used, with a field strength of 4.7 T. The magnetic field strength limits the reachable proton beam energy. The energy of the electron beam, on the other hand, is limited by the power of the radiofrequency system which is responsible for the acceleration.

Electrons and protons are stored in HERA in groups of particles called bunches. The circulating bunches, containing up to 10^{11} particles each, collide every 96 ns, which corresponds to a bunch-crossing frequency of 10.4 MHz. About 220 bunches of electrons and protons are circulating in the accelerator at the same time, according to the relation:

$$N_b = \frac{L}{\tau \cdot c} = \frac{6.3 \cdot 10^3 \text{m}}{96 \cdot 10^{-9} \text{s} \cdot 3 \cdot 10^8 \text{m/s}} \approx 220, \quad (3.1)$$

where L denotes the circumference of the accelerator and τ is the bunch-crossing time.

In order to directly determine the beam induced background in the interaction region, some electron and proton bunches are left unpaired. Therefore in addition to the colliding bunches there are so-called *pilot bunches* which don't have interaction partner. The basic parameters of the HERA collider are summarized in table 3.1.

At HERA data are delivered in periods corresponding to one filling of electron and proton bunches into the accelerator ring, so-called luminosity fills. Depending on the running conditions the average luminosity fill last up to ≈ 12 hours.

The main parameter of each collider is its luminosity. At HERA, the instantaneous luminosity depends on the number of particles N_e and N_p in the electron and proton bunches respectively, the bunch crossing frequency f and the cross sections of the beams

3 The HERA Accelerator and the H1 Detector

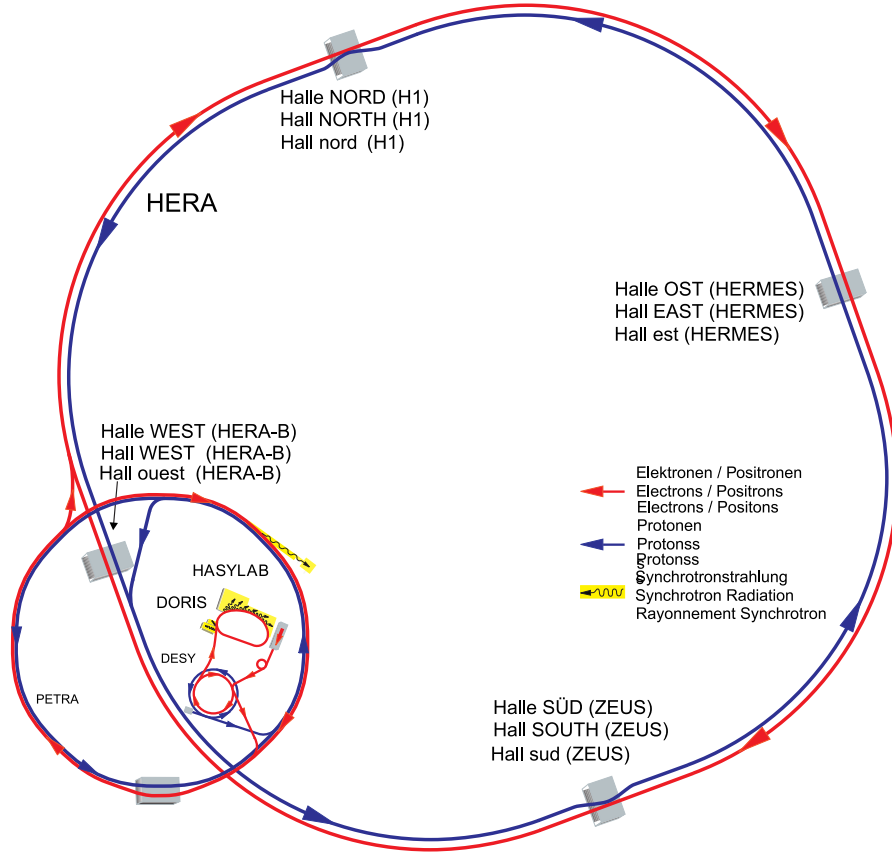


Figure 3.1: The HERA accelerator with the system of pre-accelerators.

	e-ring	p-ring	Unit
Nominal beam energy	27.5	920	GeV
Beam current	40	110	mA
Number of bunches	189	180	–
Number of particles per bunch	$4 \cdot 10^{10}$	$10.3 \cdot 10^{10}$	–
σ_z of the beam at IP	10.3	191	mm
Magnetic field strength	0.17	4.7	T
Acceleration period	200	1500	s
Peak luminosity		4.8	$10^{31} \text{cm}^{-2} \text{s}^{-1}$
Average luminosity		1.7	$10^{31} \text{cm}^{-2} \text{s}^{-1}$
Luminosity lifetime		12	h

Table 3.1: The HERA accelerator parameters.

σ_x and σ_y :

$$\mathcal{L} = \frac{f \cdot N_e \cdot N_p}{4\pi \cdot \sigma_x \cdot \sigma_y}. \quad (3.2)$$

The number of expected interactions N is proportional to the integrated luminosity $L = \int \mathcal{L} dt$ and is related to the cross section σ of any given process by:

$$N = L \cdot \sigma. \quad (3.3)$$

In September 2000 the first running phase of the HERA accelerator ended with a shut down to allow for an upgrade of the machine and the colliding beam experiments. The main goal of the upgrade was an increase of luminosity to enhance the physics potential of the experiments. To achieve this goal the HERA collider was equipped with four new super-conducting focusing magnets close to the experiments H1 and ZEUS to increase the collimation of the beams in the transverse direction σ_x, σ_y . Two of the magnets were installed in the H1 detector area for focusing the electron beam, these are: GO magnet in the forward region and GG magnet in the backward region. To avoid the background induced by the synchrotron radiation the former circular beam pipe within the H1 region had to be modified to an elliptical shape. Subsequently the innermost detectors had to be adapted to the new beam pipe geometry. One of the consequences is the non-symmetrical geometry of the BST tracker in the $X - Y$ plane, for details see section 3.5.

3.2 Detector Overview

The H1 detector is located at the northern interaction point of HERA. It was designed as a multipurpose detector capable to measure all aspects of high-energy electron-proton collisions. The detector provides a hermetic coverage of almost the entire solid angle around the interaction point (IP) and is arranged cylindrically symmetric around the beam axis. The imbalance in the energy of colliding beams ($E_p \gg E_e$) implies that the detector is asymmetric, with additional trackers in the outgoing proton direction – which, by convention, defines the positive z -direction of the H1 coordinate system. The origin of the reference system is situated in the nominal interaction point. A schematic view of the H1 detector with its coordinate system is depicted in figure 3.2.

The detector is capable to perform a number of essential tasks like: electron identification, hadron detection, charged particle tracking, muon identification, triggering and luminosity measurement. It is composed of three main parts: the forward region ($z \gtrsim 120.0$ cm), the backward region ($z \lesssim -120.0$ cm) and the central region in between. Each part consists of detectors responsible for the measurement of particle energy and its track parameters.

All subdetectors, except the muon system, are surrounded by the superconducting solenoid providing an uniform magnetic field of 1.15 T parallel to the z -axis. This allows the measurement of particle momenta and charge from the track curvature.

3.2.1 Tracking Detectors

The H1 tracking system is composed of two main components: the Central Tracking Detector (CTD) and the Forward Tracking Detector (FTD). The CTD covers the polar

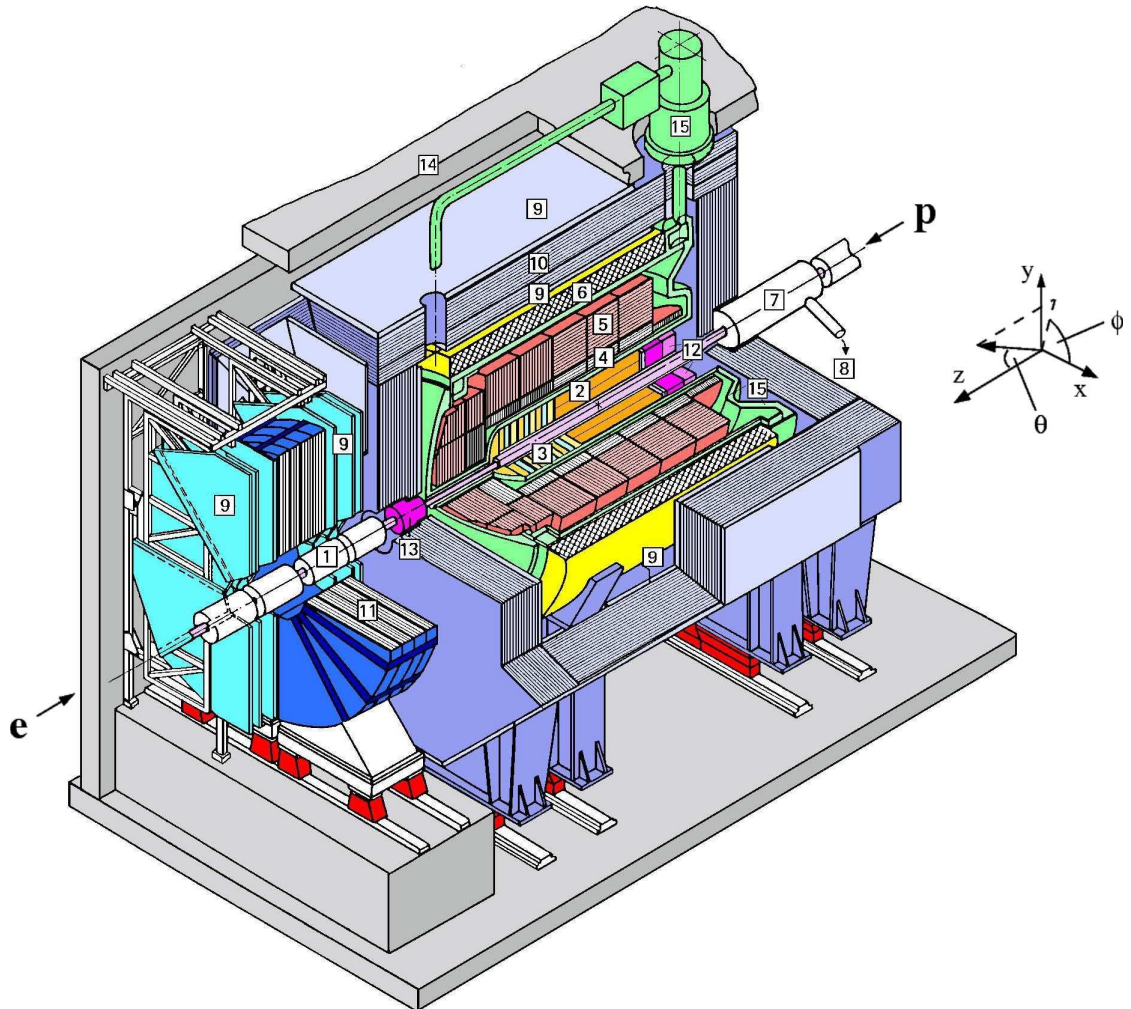


Figure 3.2: 3D view of the H1 detector. The main subsystems are: (2) central tracking chambers, (3) forward trackers, (4) electromagnetic LAr calorimeter, (5) hadronic part of the LAr calorimeter, (6) superconducting coil, (7) compensating magnet, (8) helium cryogenics system, (9) muon chambers, (10) instrumented iron, (11) muon toroid magnet, (12) warm electromagnetic calorimeter, (14) concrete shielding, (15) liquid Argon cryostat.

angle range of $15^\circ < \theta < 165^\circ$, while the FTD is sensitive for $7^\circ < \theta < 25^\circ$. In the backward region the Backward Proportional Chamber (BPC), used for accurate measurement of the calorimeter cluster position, is mounted.

On average the angular and transverse momentum resolution of the H1 tracking system are $\Delta\theta \approx 1$ mrad and $\Delta p_t/p_t^2 \approx 3 \cdot 10^{-3} \text{GeV}^{-1}$, respectively.

Central Tracking Detector

The CTD consists of drift and proportional chambers used for tracking and triggering. Nearest to the interaction point precise silicon trackers are placed, complementing track reconstruction in the central region. In the following some parameters of the detectors are summarised. A description of the CJC detector and the BST can be found in the sections 3.4 and 3.5, respectively.

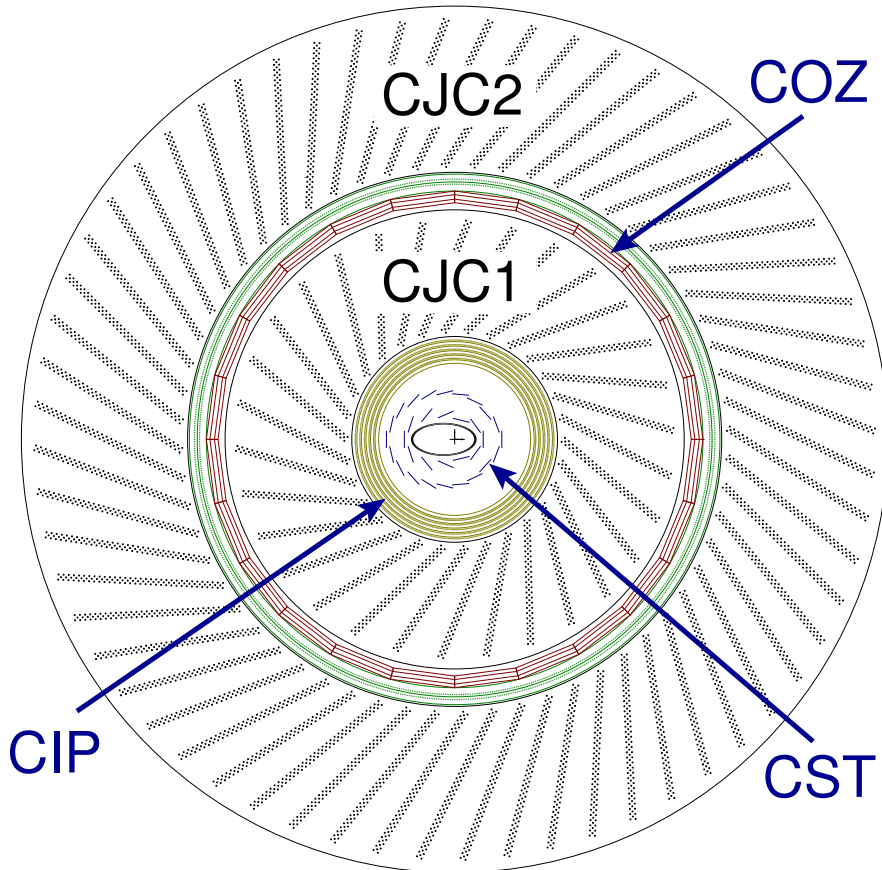


Figure 3.3: The H1 Central Tracker.

CIP

The Central Inner Proportional chamber (CIP) is a cylindrical multiwire proportional detector, mainly used for triggering purposes in the H1 experiment. The active length of the detector is in the range $-112.7 \text{ cm} < z < 104.3 \text{ cm}$.

The CIP consists of 5 layers of 480 anode wires strung parallel to the z -axis. Cathode planes mounted in 6 mm distance from the wires are made of capton coated with carbon. In addition to triggering the CIP can also be used for the interaction vertex measurement (employing complementary information about an electromagnetic cluster position). Large θ acceptance and relatively simple architecture make the CIP particularly well suited for this task.

COZ

The Central Outer z -chamber (COZ) surrounds the inner half of the CJC tracker. The sense wires of the chamber are strung in the r - ϕ plane, concentrically around the beam line. The resolution of the chamber is about $250 \mu\text{m}$ in the z -direction, while the r - ϕ coordinate is measured with about 2% accuracy using charge division technique.

CST

The CST is a silicon detector composed of two layers of double-sided silicon sensors. Its main purpose is an accurate measurement of the interaction vertex. The layers are made up of ladders of sensors. The inner layer consists of 12, while the outer of 20 ladders. The angular acceptance of the CST is $30^\circ < \theta < 150^\circ$.

The silicon modules of the detector have readout strips on both the p - and the n -side. The strips on the p -side are parallel to the z -axis and provide r - ϕ measurement with a resolution of $\sigma_{r\phi} \sim 12\mu\text{m}$. The ones on the n -side are perpendicular to the beam line and measure the z -coordinate with $\sigma_z \sim 22\mu\text{m}$.

Backward Proportional Chamber

The Backward Proportional Chamber (BPC) is a proportional gas chamber placed in front of the SpaCal calorimeter. It is composed of 3 super modules with sense wires strung perpendicularly to the beam axis, with a spacing of 2.5 mm. The super modules are tilted to each other by 45° , which ensures a stand alone measurement of the x , y coordinates.

Forward Track Detector

In the forward section of the H1 detector the tracking is complemented by the Forward Track Detector (FTD). It is designed to provide precise measurement of charged particle tracks in the range $4^\circ < \theta < 30^\circ$. The FTD consists of 9 planar chambers and 5 so-called Q-chambers, assembled in 3 super modules. The sensitive wires in both detectors are strung perpendicular to the beam line. The chambers have different orientations within one super module to ensure more accurate θ angle measurement.

FST

The Forward Silicon Tracker (FST) was designed to provide a precise measurement of the charged particle tracks in the forward direction of the H1 detector. It is also used for the determination of the interaction vertex.

The detector is composed of 5 carbon-fibre-composite wheels. They are equipped with the so-called ϕ -strip modules.

Every ϕ wheel consists of 12 modules on both sides. Since the modules are mounted back to back and their strips cross under the angle of 22.5° , full spatial hit reconstruction is possible. The geometrical parameters of the FST tracker are summarized in table 3.2.

Since the construction of ϕ modules is identical to a modules of the BST detector, see section 3.5 for further discussion.

Parameter	Value	Unit
Number of U/V disks	5	–
Number of sectors per disk	12	–
Minimal sensitive radius	5.877	cm
Maximal sensitive radius	11.966	cm
Nominal z -position of U sectors		
U disk 0	35.19	cm
U disk 1	38.49	cm
U disk 2	42.19	cm
U disk 3	46.19	cm
U disk 4	50.49	cm
z offset between U and V sensors	0.81	cm

Table 3.2: The geometrical parameters of the FST tracker.

3.2.2 Calorimeters

Liquid Argon Calorimeter

The Liquid Argon (LAr) Calorimeter is responsible for the energy measurement in the forward and central region of the H1 experiment. It covers the polar angle of $4^\circ < \theta < 154^\circ$. The detector is divided into two parts: an electromagnetic section (inner) and a hadronic one (outer), see figure 3.4.

Along the z -axis the LAr calorimeter is segmented in eight wheels of about 0.6 m length. The six barrel wheels (in the central region) are segmented in ϕ into eight octants.

The detector has a high granularity of about 45000 cells ensuring good spacial resolution of deposited energies. Each cell is basically defined by absorber material plates. In the electromagnetic section lead is used for this purpose, while in the hadronic section stainless steel is applied. Gaps between plates are filled with liquid argon working as

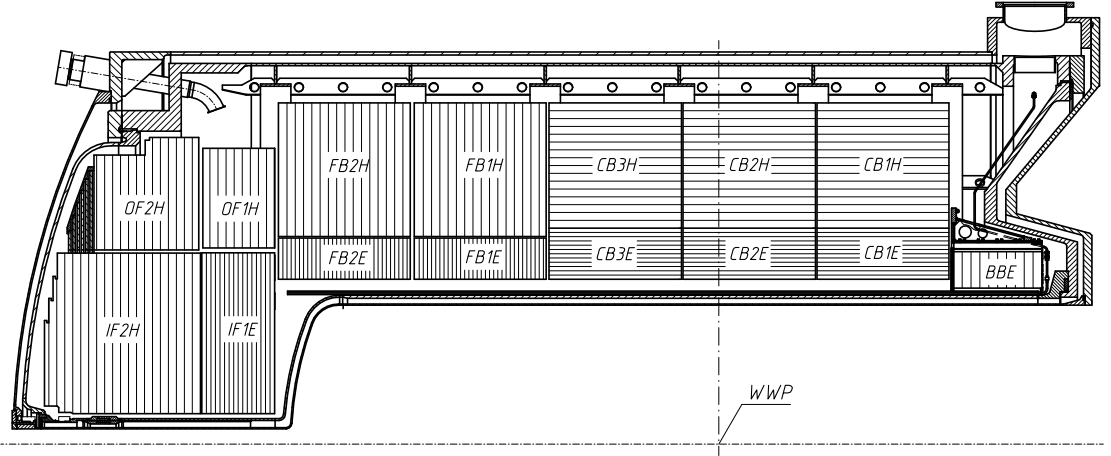


Figure 3.4: Side view of the Liquid Argon Calorimeter. The labels denote position of the particular sections: inner/outer forward (IF/OF), forward/central/backward barrel (FB, CB, BB).

active medium. In order to keep the medium fluid, the calorimeter is placed in a cryostat at about 90 K temperature.

The total thickness of the electromagnetic section varies between 20 and 30 radiation lengths for electrons and 1.0 – 1.4 interaction lengths for hadrons. The hadronic section depth build up about 5 – 8 interaction lengths.

The energy resolution has been determined to be $\sigma(E)/E = 11\% \sqrt{E/GeV} \pm 1\%$ for electromagnetically interacting particles, and $\sigma(E)/E = 50\% \sqrt{E/GeV} \pm 2\%$ for hadrons.

3.2.3 Luminosity Measurement

Instantaneous luminosity \mathcal{L} is the factor of proportionality between the observed event rate dN/dt and the cross section σ for a given process:

$$\frac{dN}{dt} = \mathcal{L}\sigma. \quad (3.4)$$

Since the total number of events is in the same way related to the integrated luminosity $L = \int \mathcal{L}dt = N/\sigma$, precise determination of the luminosity is required for the cross section measurement based on the registered number of events.

The luminosity is an important value characterizing the performance of each accelerator. Typically it is determined via the measurement of the event rate for a process with relatively high and precisely known cross section. In the H1 the Bethe-Heitler process of small-angle bremsstrahlung $ep \rightarrow E'\gamma p$ was employed for this purpose, since the cross section for the process is calculable to high precision within QED.

The angular distributions of the electrons and the radiated photons have a strong peak in the direction of the incoming electron, thus the components of the luminosity system have to be placed close to the electron beam line in negative z -direction. The

main components of the system are four calorimeters. Nearest to the nominal vertex, at $z = -5.4$ m, the Electron Tagger 6 (ET6) is situated. It is an electromagnetic calorimeter made out of lead and scintillator-fiber planes. At $z = -40.0$ m a total absorption Čerenkov calorimeter, the Electron Tagger 40 (ET40), is placed. The last two components: the Veto Counter (VT) and Photon Detector (PD) are mounted at $z = -101.4$ m and $z = -101.8$ m, respectively. The former is a water Čerenkov detector of 0.15 radiation lengths thickness. The latter is an electromagnetic calorimeter made of quartz-fibre planes between the tungsten absorber plates.

Besides luminosity determination the system is also used for tagging of photoproduction events and for the energy measurement of hard photons from the initial state QED radiation.

3.2.4 Trigger System

The bunch-crossing rate of the HERA accelerator, as mentioned in the paragraph 3.1, is 10.4 MHz. However, a large fraction of events with tracks reconstructed in the H1 detector, are background to ep interactions – mainly interactions of the electron or proton beam with the pipe wall or with residual gas atoms in the beam pipe. A fairly large background contribution comes as well from ep interactions at very low $Q^2 \sim 0$ (photoproduction events), cosmic muons and beam halo events. Depending on the beam quality, the amount of background events can exceed the ep signal by more than a factor of 10^3 . Due to the limited capabilities of the data acquisition system (DAQ) (limited readout rate, data transfer and storage), a rejection of background events is necessary, while at the same time keeping an efficient selection of ep interactions, is necessary.

The H1 uses a 4-level trigger system for this purpose. Figure 3.5 depicts its architecture with associated input rates and decision times.

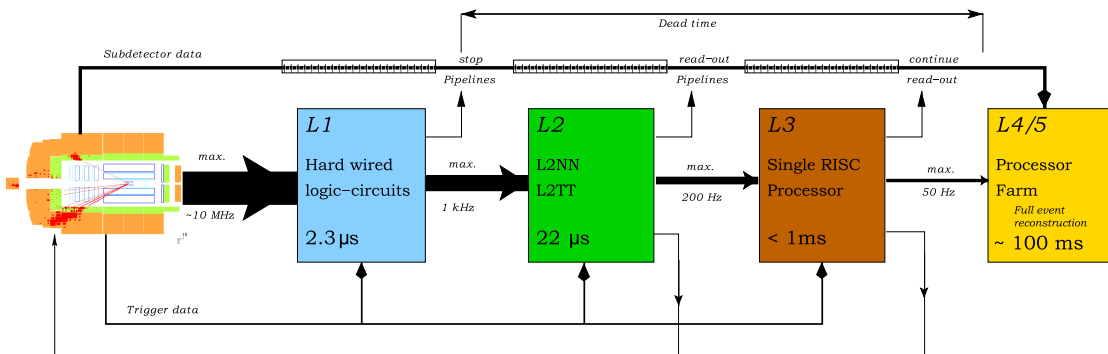


Figure 3.5: The H1 trigger system.

- L1** The first trigger level selects the events within $2.3 \mu\text{s}$. The selection is based on information provided by the different subdetectors in form of 256 Boolean values – trigger elements. Since the time of the decision is longer than the bunch crossing time, the trigger information is buffered in so-called pipelines, having a circular

structure, with a depth corresponding to 30 bunch crosses. The trigger elements are sent to the Central Trigger, where they are combined to 128 raw subtriggers via logical operations. Since some subtriggers tends to have higher rate than the others, prescale factors are very often applied, forming *actual subtriggers*. A prescale with value n means that only every n -th event is kept, even if the raw subtrigger decision is positive. The L1 decision is taken based on the actual subtriggers. If at least one of them signals a positive decision, the event is kept.

- L2** The neural network (L2NN) and topological trigger (L2TT) are used at level 2. Both systems provide up to 16 trigger elements, which are combined with the L1 subtriggers. A decision is made within $20 \mu\text{s}$. In case the event is accepted, the readout of the data stored in the pipelines is started and the period of detector insensitivity to further ep interactions begins (*dead time*). If the decision is negative pipelines stopped on L1 are resumed.
- L3** The third level trigger is based on the *Fast Tracking Trigger* (FTT). It consists of a PowerPC farm, used to combine track information provided by FTT at trigger level 2. L3 needs about $100 \mu\text{s}$ to make the decision. The event is either rejected or sent to the L4 system. After that the data taking starts again. Thus, L3 is the last system contributing to the dead time of the detector.
- L4** The main purpose of the fourth trigger level is a reduction of storage space needed and classification of events. L4 performs a full event reconstruction running the software package H1REC [22], on a RISC processors farm. Trigger decision is taken asynchronously to the data taking and hence do not contribute to the dead time. This trigger level was not used for the low and the medium data taking periods in 2007.

3.3 SpaCal Calorimeter

The SpaCal (Spaghetti Calorimeter) was designed for the precise measurement of the energy and impact position of the scattered electron in the backward region of the H1 detector. Figure 3.7 depicts the X - Y intersection of the SpaCal calorimeter. In figure 3.6 the position of the SpaCal within H1 detector is shown.

The detector has the polar angle acceptance of $153^\circ < \theta < 177.5^\circ$. It is composed of an electromagnetic and a hadronic section. The electromagnetic part consists of 1192 cells with a dimension of $4.05 \times 4.05 \text{ cm}^2$. In the z direction the depth of each cell is 25 cm, which corresponds to about 27 radiation lengths – sufficient for the complete confinement of electromagnetic showers. Individual cells in the electromagnetic part are combined to 4×4 groups, so-called super modules.

The hadronic section consists of 136 cells of size $11.9 \times 11.9 \times 25 \text{ cm}^3$, corresponding to about one interaction length. Its construction is analogical for the electromagnetic section.

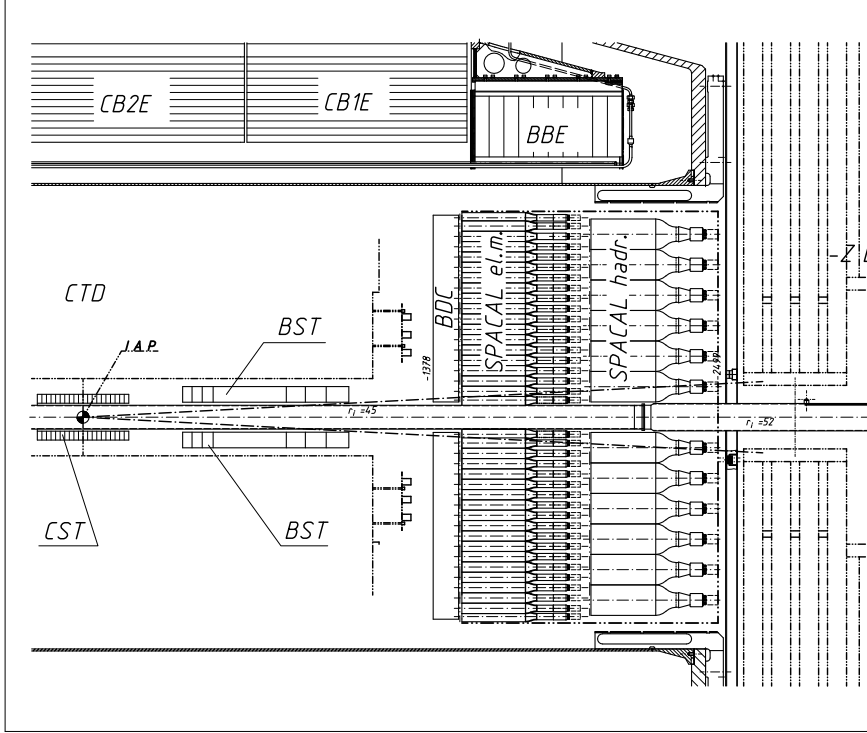


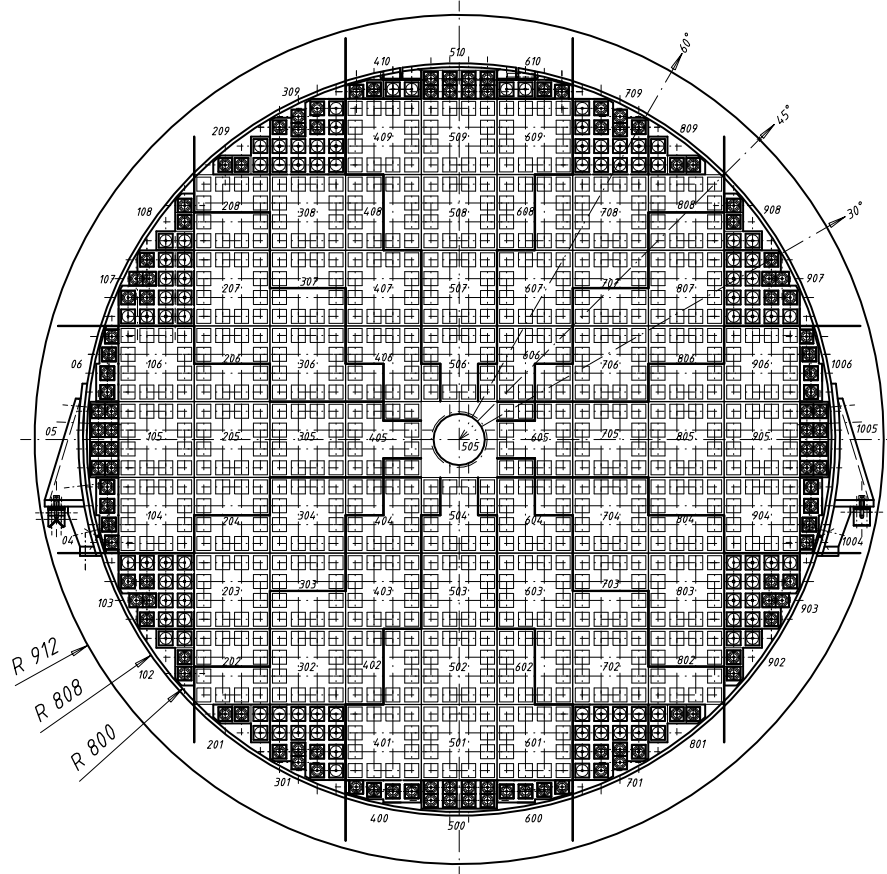
Figure 3.6: The backward section of the H1 experiment.

The Spacal is an example of a sampling calorimeter, i.e. different materials are used for the absorption and detection of particles. The cells of the detector are made of lead sheets, working as an absorber, with embedded scintillating fibres - the active material. The working principle of the detector is the following: the incident particle induces a shower of secondary particles in the lead, this causes the fibres to scintillate, then the light is mixed in an 80 mm long acrylic light mixer, and finally registered by a photomultiplier tube. The amount of registered light is proportional to the energy of the primary particle.

An energy resolution of $\sigma_E/E = 7.1\%/\sqrt{E/GeV} \pm 1.0\%$ is achieved. The spacial resolution was determined to be $\sigma_{xy} = 4.4 \text{ mm} / \sqrt{E/GeV} \pm 1.0 \text{ mm}$.

3.4 Central Jet Chamber

The Central Jet Chamber (CJC) is the main tracking device in the H1 experiment. It consists of two separate sections: the inner CJC1 and the outer CJC2. Both are concentric drift chambers having an active length of 220 cm and a radial extension of $20.3 \text{ cm} \leq r \leq 45.1 \text{ cm}$ (CJC1) and $53.0 \text{ cm} \leq r \leq 84.4 \text{ cm}$ (CJC2). The CJC1 consists of 30 cells with 24 sense wires each, the CJC2 is composed of 60 cells with 32 wires each. The wires are strung parallel to the beam axis, see figure 3.3 showing a X-Y intersection


 Figure 3.7: Electromagnetic part of the SpaCal calorimeter in x - y plane.

through the H1 tracking system.

The particle detection is based on the ionisation of a gas mixture ($\text{Ar} - \text{CO}_2 - \text{CH}_4$) by the through passing charged particles. The free electrons created by ionisation, in the presence of the electric field, drift to the anode wires. Since the wire cells have an inclination of about 30° w.r.t. the radial direction and due to the magnetic deflection, the drift direction is almost perpendicular to the wires. This guarantees an optimal track resolution of $\sigma_{r\phi} \approx 170 \mu\text{m}$ in the $r - \phi$ plane.

The z -coordinate is measured using a charge division technique, taking into account signals read out from both wire ends. For the details see section 5.6.2. The achieved resolution in the z direction is $\sigma_z < 5 \text{ cm}$.

The CJC allows measuring dE/dx with an accuracy of about 10 %, the transverse momentum p_t of a charged particles is measured with a resolution parametrized to:

$$\frac{\sigma(p_t)}{p_t} = 0.01 \cdot p_t[\text{GeV}]. \quad (3.5)$$

3.5 Backward Silicon Tracker

The Backward Silicon Tracker (BST) was built to serve for the precise measurement and identification of the scattered electron in the backward region of the H1 detector. The BST is also capable to reconstruct the interaction vertex independently of the Central Tracker. Figure 3.8 depicts the r - z view of the BST in its configuration of the years 2006-2007.

Parameter	Value	Unit
Number of U/V disks	6	–
Number of sectors per disk	12	–
Minimal sensitive radius	5.900	cm
Maximal sensitive radius	12.044	cm
Nominal z -position of U sectors		
U disk 0	-39.15	cm
U disk 1	-42.85	cm
U disk 2	-46.85	cm
U disk 3	-51.15	cm
U disk 4	-55.95	cm
U disk 5	-61.15	cm
z offset between U and V sensors	0.842	cm

Table 3.3: The BST geometrical parameters as taken from BGAS data base bank.

The detector is divided into an active part with silicon sensors, mounted closer to the interaction point and the part with readout electronics, mounted behind. The latter is connected to the supply cables and cooling system via the so-called contact ring. The frame of the BST is covered by a capton-copper foil for shielding the electronics and protecting sensitive parts.

The active part consists of six wheels equipped with the ϕ -strip modules. Each wheel is equipped with 12 such modules on both sides, forming two planes (u -type – for the sensors facing nominal vertex and v -type mounted with the back to the interaction point). The ϕ modules have trapezoidal shape as shown in figure 3.9. Strips of the neighbouring modules cross under the angle 22.5° , which allows full spatial hit reconstruction. Furthermore the modules on one side are staggered in the z -direction to ensure their overlap of $\approx 1^\circ$.

The radial extension of the BST is defined by the available space between the beam pipe and the neighbouring cylindrical proportional chamber (see figure 3.3). Thus the active area of each ϕ sensor is limited by the radial range of $59.0 \text{ mm} < r < 119.9 \text{ mm}$ and by the borders parallel to the left and right edge of the sensor. For the summary of the geometrical layout of the BST see table 3.3.

The borders between an active area and the right and outer edge of the sensor are 1.5 mm wide. The strips have variable lengths, as they are parallel to one edge of the sensor. The surface of the sensor is passivated by a polyimide layer. The strips are 12.5

μm wide with the same gap between adjacent ones. Every third strip is read out by the aluminium strip contacted via a contact pad in the upper part of sensor to the front-end electronics. The contact pads are gathered into five groups of 128 pads at the top of the sensor.

Due to the elliptical shape of the beam pipe only $3/4$ of a full ϕ acceptance is covered by the sensors, see figure 3.10.

BST Data Reconstruction

The BST data reconstruction is a two-step procedure: online hit finding and offline track reconstruction. The online hit finding is performed during the H1 data taking. The algorithm is implemented in C programming language and executed on the RIO 8092 boards [31]. The hit finding routine works on the digitized strip pulses from the PMC boards. The main purpose of the procedure is to distinguish signals induced by passing particles from the noise pulses originated from different sources.

The main contribution to the noise in the raw data is pedestal, which mainly accounts for the leakage current characteristically for every single strip. The pedestals are constantly updated, since their magnitudes depend on many factors, like for example the temperature of the sensors. Other factors, which have influence on the value of the pedestal, are constant – like the relative geometrical position of the strip in the hybrid, the length of the strip, and related to that, the capacity. By subtraction of the pedestals nonlinearities in the amplitude distribution and spikes in the raw data caused by dead strips are suppressed, which is essential in the follow-up step of reconstruction.

The other sources of noise are the Common Mode (CM) and the Common Slope (CS), which account for fine fluctuations in the sensor depletion voltage and the supply voltage of the APC preamplifiers which lead to a common shift per APC. The CM and CS parameters are used in a linear function $f(i) = CM + CS \cdot i$ fitted on the pedestal-subtracted APC amplitude spectra and describe the noise contribution as a linear function of the strip number i in a given APC module. After the pedestal, the common mode and the common slope subtraction from the raw data in a strip without a hit, the only component left is random electronic noise (N).

The amplitude of a possible signal hit in a given event can be calculated using the following formula:

$$A_i = Rd_i - Ped_i - (CM_a + i \cdot CS_a), \quad (3.6)$$

where Rd_i is the raw data signal of the strip i , Ped_i describes its pedestal, CM_a and CS_a are common mode and common slope for a given APC chip a , respectively. After pedestal subtraction a linear function is fitted per each APC, which gives values of the CM_a and CS_a . Subsequently, the amplitude of the signal is calculated using equation 3.6. If the signal on a given strip meets the conditions:

$$A_i > 0, \quad (3.7)$$

$$A_i^2 > N^2 \cdot C, \quad (3.8)$$

where C is a confidence level constant used to suppress the noise, the hit information are written out as an entry in the H1 BOS [10] bank SIFE, together with the strip position and the level of noise. The signal finding procedure is repeated again excluding this time already found hits in the first instance from the common mode calculation, thus enhancing the integrity of signal determination. The data without found hits are used for pedestals and noise N update. An example of the hit finding procedure for one channel of BST is presented in figure 3.11. The hits found at this stage form the basis for the next step of the reconstruction: the track finding.

The track finding is performed by the reconstruction package H1BSTREC, which is a part of the standard H1 reconstruction software H1REC. A dedicated electron finder utilizing information provided by the BST and CJC trackers has been developed (see appendix B) serving specifically for the current analysis. Therefore standard BST track finding will be only briefly discussed here.

The track reconstruction is done in two steps: 2D pattern recognition and 3D track finding. In the first step the precise impact point position of the particle is calculated combining neighbouring hits into so-called clusters. Afterwards all reconstructed cluster coordinates are fitted by parabolas applying a χ^2 minimisation procedure.

In the next step the 3D track finding is performed using a Kalman filter procedure. The parabolas obtained in 2D pattern recognition are combined together to determine hit space points. A parabola combination where any of the obtained space points is outside the geometrical acceptance is excluded. Afterwards the calculated space points are fitted by a helix. The tracks obtained are sorted according to the following criteria:

- **Number of linked hits:** tracks with the highest number of hits are preferred.
- **Vertex pointing:** tracks pointing to the parabola fitted vertex are of higher priority.
- **χ^2 requirement:** obtained tracks are sorted according to the χ^2 of the fit.

The points and parabolas of the best track are excluded from the further treatment. The procedure of combining parabolas is repeated until at least one track with minimum number of hits required for the helix fit is available.

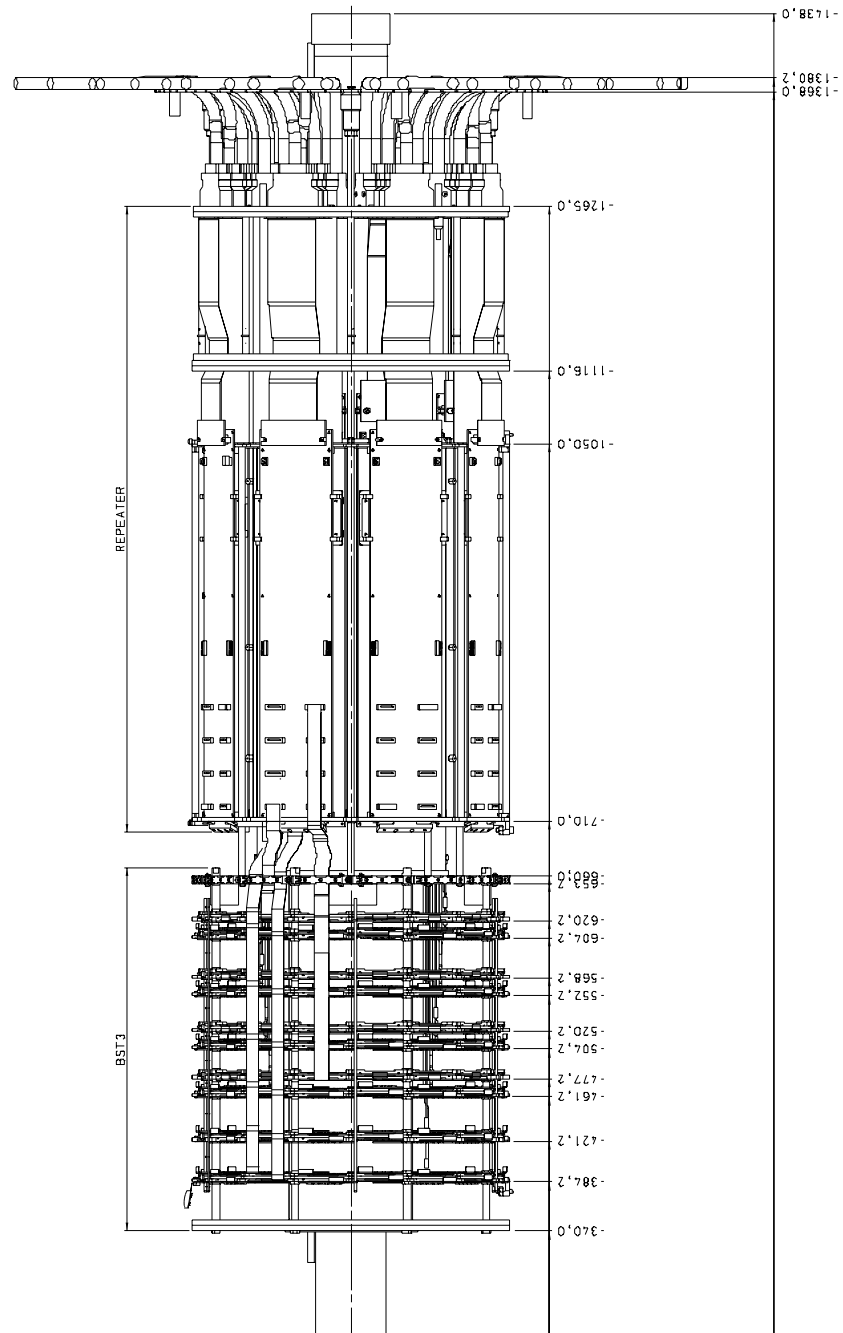


Figure 3.8: The side view of the Backward Silicon Tracker with depicted contact ring, front-end electronics and the active part.

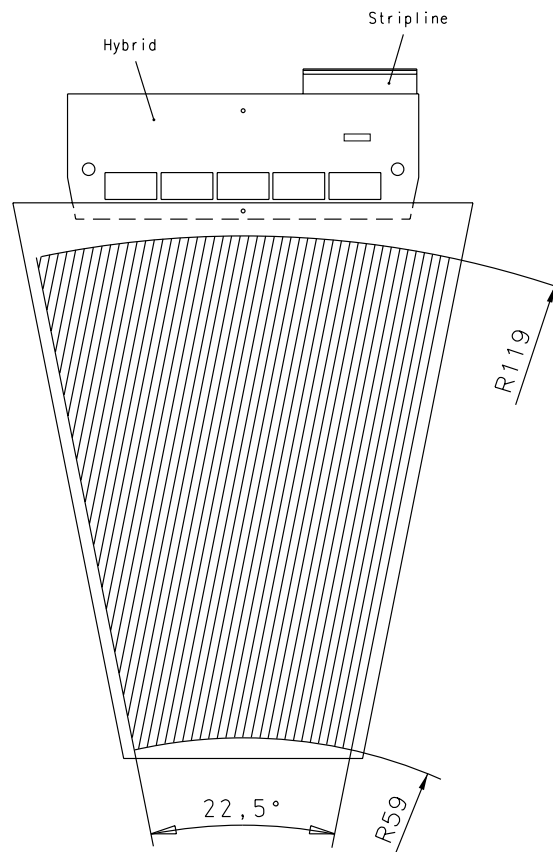


Figure 3.9: The ϕ module of the BST with depicted strips and attached readout electronics.

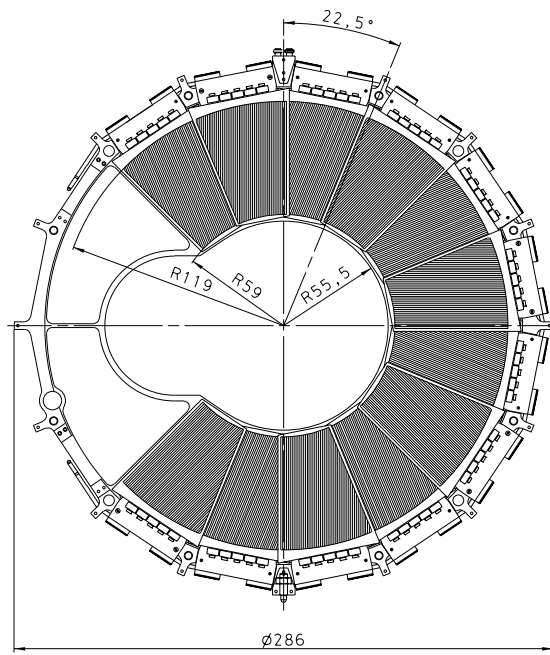


Figure 3.10: The BST disk equipped with detector modules.

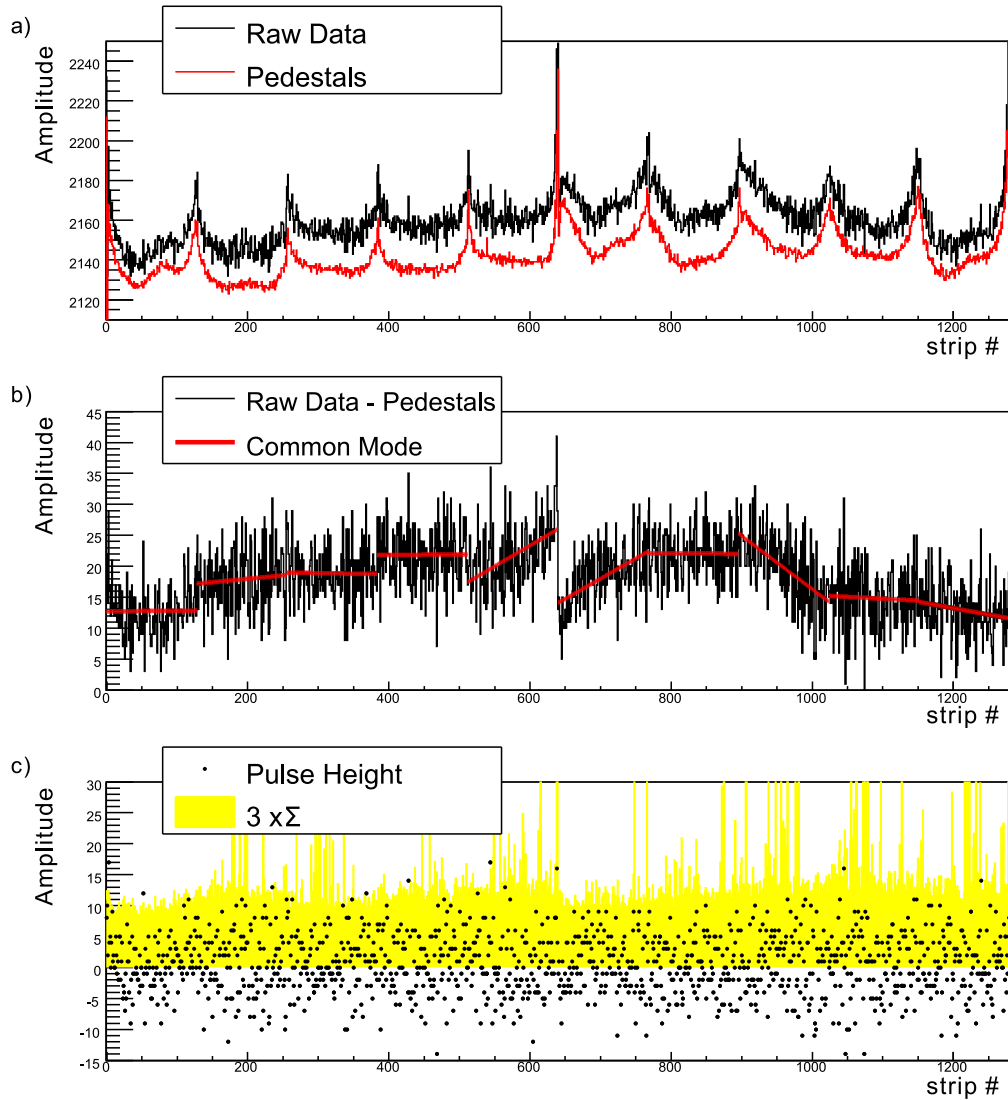


Figure 3.11: Hit finding procedure for one channel of the BST. a) Raw data, b) raw data with subtracted pedestals and fitted common mode c) data with subtracted pedestals and depicted region of $3x\Sigma_i$.

4 Cross Section Measurement

4.1 Reconstruction of the Event Kinematics

The measurement of the deep-inelastic cross section requires an accurate reconstruction of the kinematic variables x , y and Q^2 . For a fixed center of mass energy $s = 4E_e E_p$, where E_e and E_p denote energies of the incoming electrons and protons respectively, only two of these variables are independent due to the relation $Q^2 = sxy$.

From an inclusive point of view, the total final state of the scattering process consists of the electron and the hadronic final state (HFS), which refers to the measurement of all particles excluding the identified electron. Since H1 is a collider experiment and the detector covers almost the entire solid angle, both the scattered electron as well as the hadronic final state particles are reconstructed. Therefore several reconstruction methods, relying either on the scattered electron or on HFS, are available. This redundancy allows for a choice of the method providing the best resolution in a certain region of the kinematic phase space. In the following various reconstruction methods are briefly discussed.

Electron Method

For the Electron Method only the scattered electron energy E'_e and its polar angle θ_e are used:

$$y_e = 1 - \frac{E'_e}{E_e} \sin^2 \frac{\theta_e}{2}, \quad (4.1)$$

$$Q_e^2 = 4E'_e E_e \cos^2 \frac{\theta_e}{2} = \frac{E_e'^2 \sin^2 \theta_e}{1 - y_e}. \quad (4.2)$$

The prefix e is used here to denote name of the method. The variable x is calculated as $x_e = Q_e^2 / sy_e$.

From the given formulae a few conclusions can be drawn: for a large scattering angles $\theta_e > 150^\circ$, the inelasticity variable y depends predominantly on the scattered electron energy E'_e . Hence, the large y domain corresponds to low energies E'_e . For low values of y the virtuality Q^2 is almost solely defined by the polar angle θ_e .

Performing an error propagation for formulae 4.1 and 4.2 results in the following equations:

$$\frac{\delta Q^2}{Q^2} = \frac{\delta E}{E} \oplus \tan \frac{\theta_e}{2} \delta\theta_e, \quad (4.3)$$

$$\frac{\delta x}{x} = \frac{1}{y} \frac{\delta E}{E} \oplus \tan \frac{\theta_e}{2} \left(x \frac{E_p}{E} - 1 \right) \delta\theta, \quad (4.4)$$

$$\frac{\delta y}{y} = \frac{1-y}{y} \frac{\delta E}{E} \oplus \frac{1-y}{y} \cot \frac{\theta_e}{2} \delta\theta_e. \quad (4.5)$$

Based on these equations it can be concluded, that the Electron Method should be employed only in a high y region of the kinematics phase space. At low y resolutions of x and y deteriorate, due to the factor $1/y$, and usually other reconstruction methods are used.

Hadron Method

As already mentioned, apart from the electron side, the kinematics of the scattering process can be reconstructed from the measurement of the hadronic final state. However, since it is impossible to build a completely hermetic detector, leakage of particles is unavoidable. Due to the large difference in beam energies, effects of particles leakage along the outgoing proton beam are more important. For the reconstruction of the kinematics, variables as insensitive as possible to losses are chosen, these are the total transverse momentum:

$$p_{t,h} = \sqrt{\left(\sum_i p_{x,i}\right)^2 + \left(\sum_i p_{y,i}\right)^2}, \quad (4.6)$$

and the energy, longitudinal momentum difference:

$$\Sigma = \sum_i E_i - p_{z,i} = \sum_i E_i (1 - \cos \theta_i). \quad (4.7)$$

In these equations the variables E_i , $p_{x,i}$, $p_{y,i}$ and $p_{z,i}$ are the components of the four-vector of the hadronic final state particle i and the summation is performed over all particles of the hadronic final state.

Due to energy and momentum conservation the following relations are satisfied:

$$p_{t,e} - p_{t,h} = E_e \sin \theta_e - p_{t,h} = 0, \quad (4.8)$$

$$E - p_z \equiv (E_e - p_{z,e}) + \Sigma = E_e (1 - \cos \theta_e) + \Sigma = 2E_e. \quad (4.9)$$

Finally one can define a hadronic angle γ_h , which in Quark Parton Model is equivalent to the polar angle of the struck parton:

$$\tan \frac{\gamma_h}{2} = \frac{\Sigma}{p_{t,h}}. \quad (4.10)$$

4.1 Reconstruction of the Event Kinematics

Using Σ and $p_{t,h}$ the equations 4.1 and 4.2 can be transformed to the following:

$$y_h = \frac{\Sigma}{2E_e}, \quad (4.11)$$

$$Q_h^2 = \frac{p_{t,h}^2}{1 - y_h}. \quad (4.12)$$

This approach to determine the event kinematics is denoted as Hadron Method, since it relies on the measurement of the hadronic final state only. In general the resolution of the method is worse than the electron method and depends on a good reconstruction of the HFS, on the other hand it is the only method applicable for charged current events, since it incorporates no information about the scattered electron.

Sigma Method

Due to the presence of the electron beam energy E_e in equations 4.1 and in 4.11, both of the above methods are sensitive to collinear real photon emission from the incoming lepton, which lowers the energy available for the process. For these initial state radiation events, both methods fail to reconstruct the kinematics correctly. However, according to equation 4.9, variable E_e can be replaced by $(E - p_z)/2$. One then obtains the following relations:

$$y_\Sigma = \frac{\Sigma}{\Sigma + E'_e(1 - \cos \theta_e)}, \quad (4.13)$$

$$Q_\Sigma^2 = \frac{E_e'^2 \sin^2 \theta_e}{1 - y_\Sigma}. \quad (4.14)$$

These formulae define the so-called sigma method. The sigma method provides a good resolution in a relatively wide kinematic range, but is inferior to the electron method at high y .

Double Angle Method

The double angle method uses the polar angle of the scattered electron θ_e and of the struck quark γ_h , assuming that the quark forms a single massless jet:

$$y_{DA} = \frac{\sin \theta_e (1 - \cos \gamma_h)}{\sin \gamma_h + \sin \theta_e - \sin(\theta_e + \gamma_h)}, \quad (4.15)$$

$$Q_{DA}^2 = \frac{4E_e^2 \sin \gamma_h (1 + \cos \theta_e)}{\sin \gamma_h + \sin \theta_e - \sin(\theta_e + \gamma_h)}, \quad (4.16)$$

$$x_{DA} = \frac{Q_{DA}^2}{s y_{DA}}. \quad (4.17)$$

This method is sensitive to photon emission from the primary electron. On the other hand, it is mostly independent of the calorimeter energy scales. Therefore the double angle method is suitable for the check and improvement of the energy calibration and the hadronic system measurement.

Since the electron method is superior to all others in high y domain, where the measurement of the structure function $F_L(x, Q^2)$ is performed, this method is used by default in the following analysis.

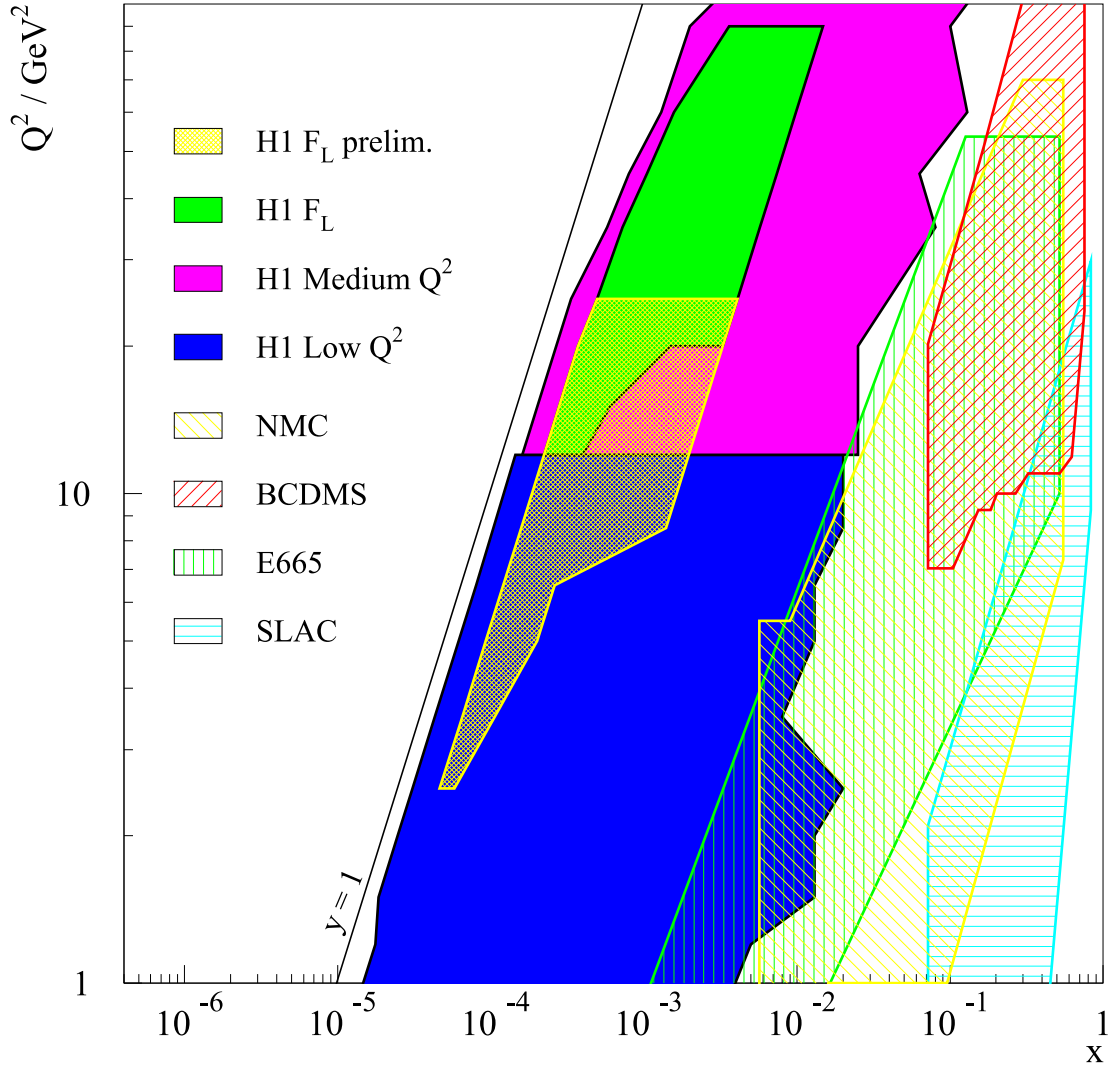


Figure 4.1: The H1 coverage of the kinematic phase space in comparison to previous fixed-target experiments.

The structure functions describing the DIS process depend on the kinematic variables x and Q^2 . The kinematic phase space covered by the H1 experiment is shown in figure

4.1 in comparison with the fixed-target experiments. As can be seen, HERA provides extensive access to a wide kinematic range. The DIS data of H1 covers roughly the range of $1 \text{ GeV}^2 \lesssim Q^2 \lesssim 5 \cdot 10^4 \text{ GeV}^2$ and $10^{-5} < x < 0.65$. The yellow area in figure 4.1 depicts the range covered by this analysis with $2.5 \text{ GeV}^2 \leq Q^2 \leq 25 \text{ GeV}^2$.

4.2 Monte Carlo Simulation

The measurement of the DIS cross section requires correction for the limited detector efficiencies and acceptances. Furthermore effects like migration of events due to finite resolution or photon radiation have to be taken into account. It is usually very difficult to determine all corrections directly from the data sample. To avoid complicated unfolding procedure so-called Monte Carlo techniques are employed to perform a simulation of the ep interactions in the H1 detector. If detector effects are correctly implemented the unfolding procedure can be replaced by a comparison of the number events observed in data and simulation, see section 4.5.

The MC simulation consists of two parts: the generation of the pure physics process and the simulation of the detector response. The result of the former are the four-momenta of all final state particles. The generation of events is performed using the following procedure: before the event generation the total cross section σ_{tot} for the ep scattering is calculated. Afterwards a point (x, Q^2) of the kinematic phase space is chosen randomly for each event with probability $(d\sigma/dxdQ^2)/\sigma_{tot}$. In the first step elementary scattering process for the event is generated. Subsequently, additional partons, so-called parton cascades are calculated. Finally, in the hadronisation phase the partons are transformed into observable hadrons.

DIS events used in this analysis are generated using the DJANGO 1.4 [35] event generator which includes leading order QED radiative effects as implemented in HERACLES [28]. For the event generation, leading order parton distribution functions define F_2 while F_L is set to zero. The structure functions are subsequently reweighted to the fractal model parameterisation of F_2 and to F_L . The final state parton showers are simulated using the Colour Dipole Model [20, 6] as implemented in ARIADNE 4.1 [29]. Events with a very low mass of the hadronic final state ($W < 5\text{GeV}$) are simulated using SOPHIA [30], which includes a detailed description of low mass final states, including the resonance region. The fragmentation into hadrons is performed with JETSET 7.4 [36]. Photoproduction background is generated with the PHOJET 1.6 [14] program, which uses a two-component dual parton model [12] including diffractive processes and vector meson production. The simulation of QED radiative corrections includes photon emission from the lepton. Radiation from quarks, which is estimated to be small for low x , is not simulated. The simulation of QED radiative corrections is checked using the analytical calculation package HECTOR [7]. An agreement to better than 0.5% is found in the kinematic range of this measurement.

The generated events are passed through a simulation of the H1 detector response based on the GEANT3 [11] package. Tracing of the particles in the trackers up to the calorimeters is based on a detailed description of the detector material. The response

of the calorimeters to electromagnetic particles is simulated using a fast shower parameterisation technique H1FAST [19], while the hadronic response is simulated using GHEISHA [15]. The level of noise and beam related background in the calorimeters is determined using events from dedicated runs with random triggers which are overlaid on the simulated events. Spurious hits in the BST are added to the simulation based on randomly triggered events.

The Monte Carlo events are subjected to the same reconstruction and analysis procedure as the data. Also, for consistency of the analysis, the calibrations of the SpaCal and the LAr, as well as the BST alignment, are performed for the reconstructed MC events in the same way as for the data.

4.3 Electron Identification

As shown in section 4.3 correct identification of the scattered electron is crucial for reconstruction of the event kinematics. Without an identified electron also the hadronic final state is not well defined. The starting point for the electron identification are the energy depositions (clusters) in the backward calorimeter. However, for high inelasticities of $y \gtrsim 0.1$ also hadronic particles deposit energy in the SpaCal as the hadronic angle γ_h enters its acceptance. Figure 4.2 depicts typical high y event with the hadronic final state particles detected in the SpaCal. These energy depositions can mimic the signature of the scattered electron, which makes its identification not straightforward in the high y region of the kinematic phase space.

According to equation 4.8 the transverse momentum of the scattered electron is balanced by the sum of the transverse momenta of the hadronic final state particles. Therefore the particle with the largest transverse momentum is in most cases the scattered electron, which is the main selection criterion used in the present analysis. In the following only energy depositions of more than 3.4 GeV in the SpaCal are considered. The background contribution from hadrons is further reduced by the requirement of a small transverse size of the cluster R_{log} , which is estimated using a logarithmic energy weighted cluster radius, as the clusters coming from hadrons have in general larger radii. Additionally a cut on the energy behind the cluster, measured in the hadronic section of the SpaCal, is used. The contribution from neutral particles and wrong charge particles is reduced by the requirement of a reconstructed track linked to the cluster, with a charge corresponding to the charge of the lepton beam.

An additional suppression of the photoproduction background is achieved by requiring longitudinal energy-momentum conservation (see equation 4.9), which for genuine, non-radiative DIS events is approximately equal to $2E_e$. This requirement also reduces contribution from events with hard initial state photon radiation. Finally, QED Compton events are excluded using a topological cut against two back-to-back clusters in the SpaCal.

For more detailed discussion of the selection criteria used for the electron identification see chapter 5.

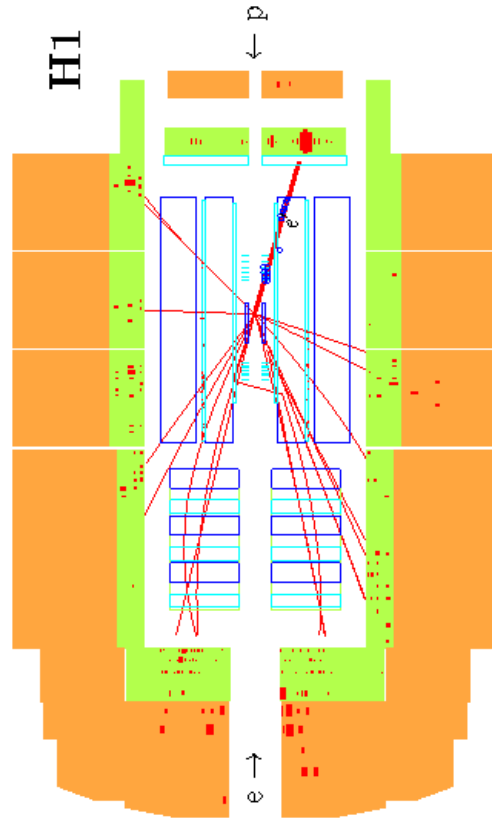


Figure 4.2: A view of a high y event reconstructed in the H1 detector. The positron and proton beam directions are indicated by the arrows. The central tracker consists of the silicon tracker, the drift chambers CJC1 and CJC2, it is surrounded by the liquid argon (LAr) calorimeter. The detector operates in a solenoidal magnetic field of 1.16 T. The scattered positron trajectory is reconstructed in the backward silicon tracker BST and the CJC1. The charge of the particle is determined using the track curvature. The positron energy is measured in the electromagnetic part of the SpaCal calorimeter.

4.4 Background Identification and Subtraction

In the high y range, corresponding to a low energy of the scattered electron E'_e , the remaining background contribution after the event selection may be still comparable to or even exceeding the DIS signal. The method of background identification used in this analysis relies on the determination of the electric charge of the electron candidate from the curvature of the associated track.

Figure 4.3 depicts E/p distribution of the scattered electron from e^+p interaction with the energy E measured in the SpaCal and the momentum p of the linked track determined by the combined CJC and BST electron finder, see appendix B. Due to the good momentum resolution distributions for negative and positive charges are well separated. Tracks with a negative charge are assigned a negative E/p . Since the charge of the lepton beam was positive, these tracks represent almost pure background, and are termed wrong sign tracks. The higher peak of E/p distribution contains the genuine DIS signal superimposed on the remaining positive background. The size of the latter, to first approximation, equals the wrong sign background.

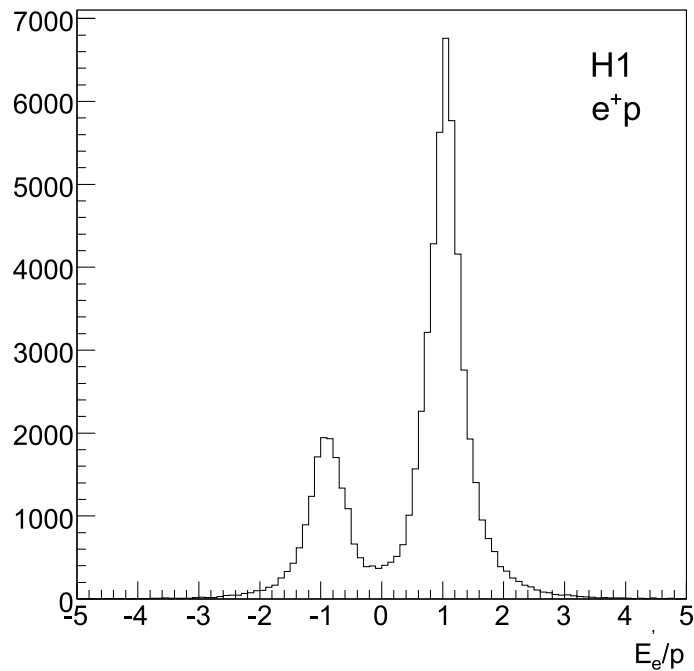


Figure 4.3: E/p distribution of energy over momentum for tracks linked to clusters in the SpaCal. Energy of the scattered electron candidate is limited to the range from 3.4 GeV to 10 GeV.

The basic technique of background subtraction, and thus measurement of the DIS

cross section in the high y range, consists of the subtraction of the wrong sign from the right sign event distribution in each x, Q^2 interval.

4.4.1 Charge Asymmetry

The background subtraction based on the charge measurement requires a correction for a charge asymmetry in the positive and negative background samples, as has been already observed by H1 [3]. The main reason for the charge asymmetry lies in the enhanced energy deposited by anti-protons compared to protons at low energies.

This charge asymmetry is determined from the measurement of tagged photoproduction events. The main selection criterion used is the requirement of energy deposited in Electron Tagger and not in Photon Tagger. Additionally a cut on tagger acceptance is applied. To avoid background from overlap of Bethe-Heitler and normal DIS events, a cut on total energy momentum balance $E - p_z$ is used. Residual DIS background is estimated from comparison of tagged and DIS events at high energies of the scattered electron of $E'_e > 17$ GeV. The summary of cuts used for this study is given in table 4.1. The rest of the selection criteria are the same as for the standard DIS selection, see table 5.5.

With use of tagged events, the asymmetry factor can be defined as a ratio of tagged events with positive track charge N_{tagged}^+ to events with negative charge N_{tagged}^- :

$$\kappa = \frac{N_{tagged}^+}{N_{tagged}^-}. \quad (4.18)$$

The ratio κ , as a function polar angle θ is shown on figure 4.4.

Independent studies proved that the effect of applying θ -dependent asymmetry factor compared to constant value is negligible [34] for the cross section measurement. Therefore, constant asymmetry factor of 0.98 for data and of 0.944 for Monte Carlo, respectively, are used in the analysis.

Quantity	Comment
$E_e^{tagged} > 2$ GeV	Energy deposited in electron tagger
$E_\gamma^{tagged} < 2$ GeV	Minimal energy deposit in photon tagger
TE(115)	Corresponding trigger element required
$(E - p_z)^{tot} < 80$ GeV	Avoid overlap of Bethe-Heitler and DIS events
$X^{tagged} > -2.8$ cm $E_e^{tagged} > 6$ GeV	Cut on tagger acceptance

Table 4.1: Summary of the cuts used to select tagged photoproduction events.

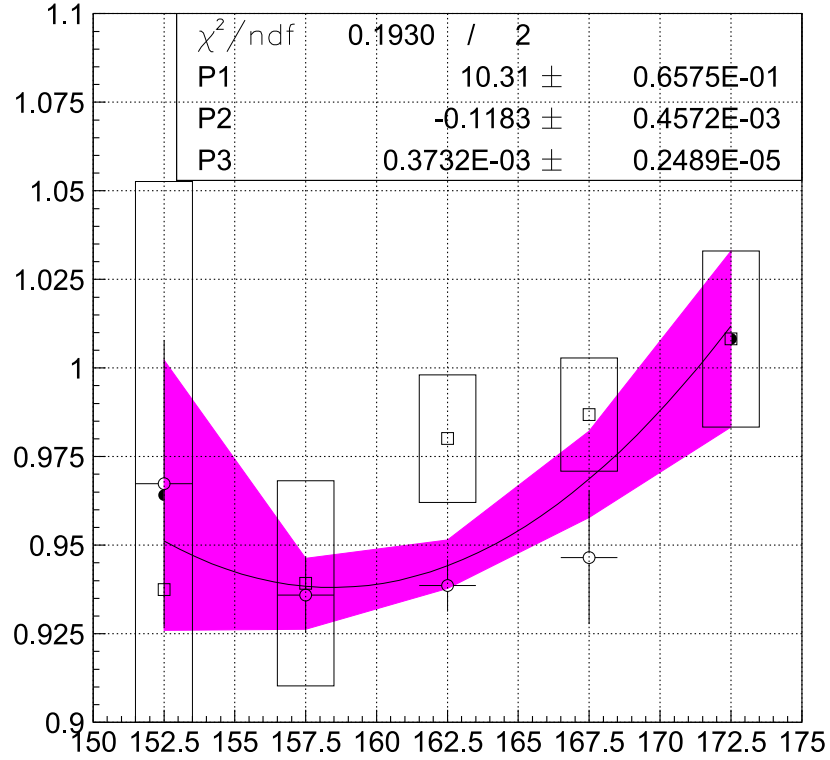


Figure 4.4: θ dependence of the asymmetry factor κ determined with tagged events.

4.5 Cross Section Determination

The measurement of the cross section is performed in bins of y and Q^2 . The reason for choosing y instead of Bjorken x , is that the former is more appropriate for the high y region of the kinematic phase space, where the measurement of structure function F_L is performed. Furthermore many detector effects, like resolution and vertex efficiency determination, are y -related.

Boundaries and centers of the analysis bins are listed in tables 4.2, 4.3 and 4.4. As can be seen high y values up to ≈ 0.85 are reached in the analysis. The same Q^2 binning was chosen for the whole range of y considered and for both low and medium energy running periods.

The cross section measurement in a particular bin is performed using the integrated luminosity \mathcal{L}_{Data} and the number of events collected in the bin N_{Data} , according to the relation $\sigma = N_{Data}/\mathcal{L}_{Data}$. However, in the real experiment various corrections have to be applied, which finally results in the following formula:

$$\frac{d^2\sigma_r}{dx dQ^2} = \frac{N^{Data} - N^{BG}}{\mathcal{L}^{data}} \frac{1}{A} \frac{1}{\epsilon} \frac{1}{1 + \delta} \beta_{BC}, \quad (4.19)$$

Bin Centers Q^2 / GeV^2					
2.5	3.5	5.0	6.5	8.5	12.0
15.0	20.0	25.0			

Bin Boundaries Q^2 / GeV^2					
2.371	3.162	4.217	5.623	7.499	9.9999
13.34	17.78	23.71	31.62		

Table 4.2: Q^2 bin central values and boundaries. Q^2 binning is the same for low and medium energy running periods.

Bin Centers y					
0.85	0.75	0.65	0.49	0.31	0.20
0.12	0.078	0.049	0.031	0.020	0.012
0.007					

Bin Boundaries y					
0.90	0.80	0.70	0.60	0.38	0.24
0.15	0.095	0.060	0.038	0.024	0.015
0.0095	0.0050				

Table 4.3: Y bin central values and boundaries, for low energy ($E_p = 460$ GeV) running period.

Bin Centers y					
0.848	0.76	0.68	0.60	0.52	0.392
0.248	0.16	0.096	0.0624	0.0392	0.0248
0.016	0.0096	0.0056			

Bin Boundaries y					
0.896	0.80	0.72	0.64	0.56	0.48
0.304	0.192	0.12	0.076	0.048	0.0304
0.0192	0.012	0.0076	0.0040		

Table 4.4: Y bin central values and boundaries, for medium energy ($E_p = 575$ GeV) running period.

4 Cross Section Measurement

where:

- N^{Data} Total number of events which passed DIS selection criteria per analysis bin.
- N^{BG} Total number of background events accumulated in the analysis bin which fulfil the DIS selection. The amount of such events is estimated using wrong sign tracks.
- A Detector acceptance which is quantified using Monte Carlo simulation, as the ratio of the number of reconstructed to the number of generated events $A = N_{rec}/N_{gen}$.
- \mathcal{L}^{data} Total integrated luminosity using the luminosity detector measurement.
- δ Radiative corrections on the Born level cross section estimated from the Monte Carlo simulation as $\delta = \sigma_{rad}^{MC}/\sigma_{Born}^{MC} - 1$. Here σ_{rad}^{MC} , σ_{Born}^{MC} denote the bin integrated full and Born level cross sections respectively.
- ϵ Extra efficiency corrections not included in Monte Carlo simulation.
- β_{BC} Bin centre correction, which transforms the bin integrated value to the double differential value at the chosen bin centre (x_c, Q_c^2) . It can be calculated as $\beta_{BC} = \frac{d^2\sigma}{dx dQ^2} / \sigma_{Born}$.

Since radiative corrections are already included in the simulations, one can exploit:

$$N_{gen}^{MC} = \mathcal{L}^{MC} \sigma_{rad}^{MC}, \quad (4.20)$$

which leads to the formula to determine the cross section via the Monte Carlo method:

$$\frac{d^2\sigma_r}{dx dQ^2} = \frac{N^{Data} - N^{BG}}{N^{MC}} \frac{\mathcal{L}^{MC}}{\mathcal{L}^{data}} \frac{d^2\sigma_r^{MC}}{dx dQ^2}. \quad (4.21)$$

According to equation 4.21 the measured cross section is proportional to that used in MC simulations re-weighted by the ratio of the number of DIS events in a particular analysis bin in data and simulation. The ratio is normalised to data and Monte Carlo luminosities.

4.5.1 Bin Selection

As introduced in the previous section, the cross section measurement is performed in intervals of Q^2 and y . To control the migration effects two quantities are defined: the purity P and the stability S . They are determined for the Monte Carlo sample and defined as the ratio of the number of events generated and reconstructed $N^{MC,rec\&gen}$ in analysis bin to the total number of events reconstructed $N^{MC,rec}$ (generated $N^{MC,gen}$) in the bin:

$$P = \frac{N^{MC,rec\&gen}}{N^{MC,rec}}, \quad (4.22)$$

$$S = \frac{N^{MC,rec\&gen}}{N^{MC,gen}}. \quad (4.23)$$

The purity denotes the probability that an event reconstructed in a certain bin has been generated in that bin as well. The stability is the probability that an event generated in a given bin is reconstructed in the same bin. Therefore, the purity denotes the migration of events from neighbouring bins into certain bin, while the stability expresses the migration out of that bin. By definition both quantities can only take values between 0 and 1.

Figures 4.5 and 4.6 depict the purity and stability for the Monte Carlo simulation for the low energy running period. Figures 4.7 and 4.8 denote both variables for the medium energy running period.

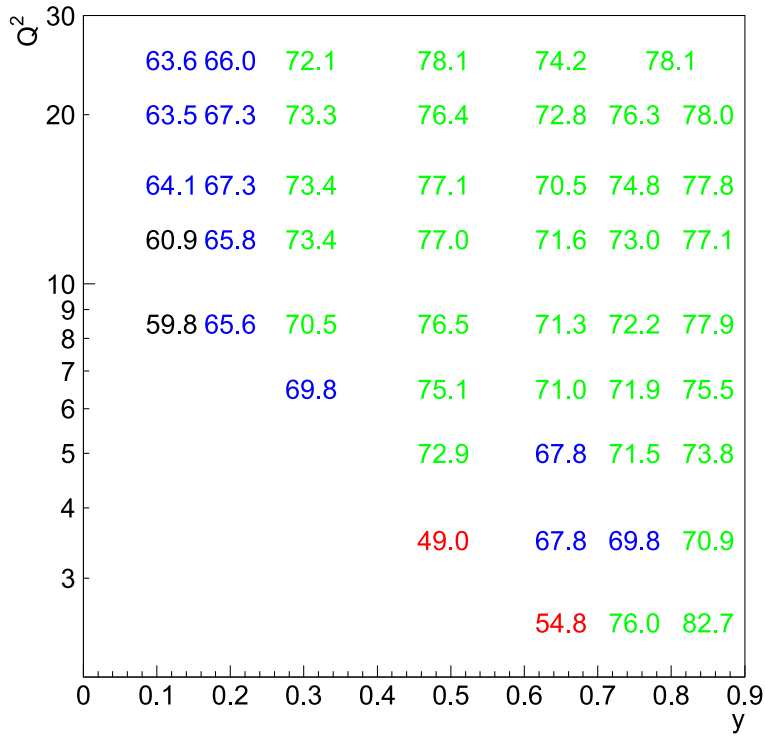


Figure 4.5: Purity P in per cent for each analysis bin for the low energy running period.

4 Cross Section Measurement

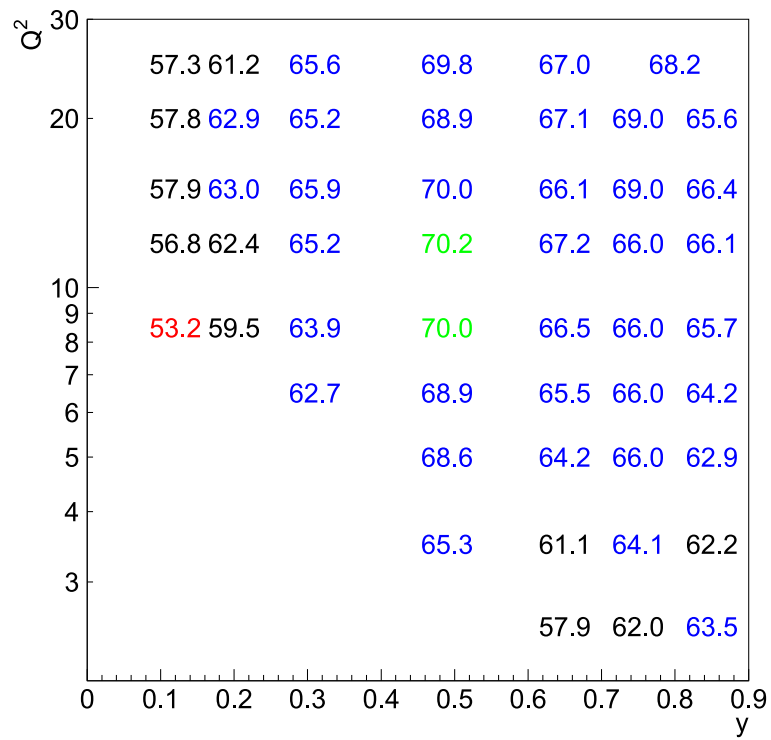


Figure 4.6: Stability S in per cent for each analysis bin for the low energy running period.

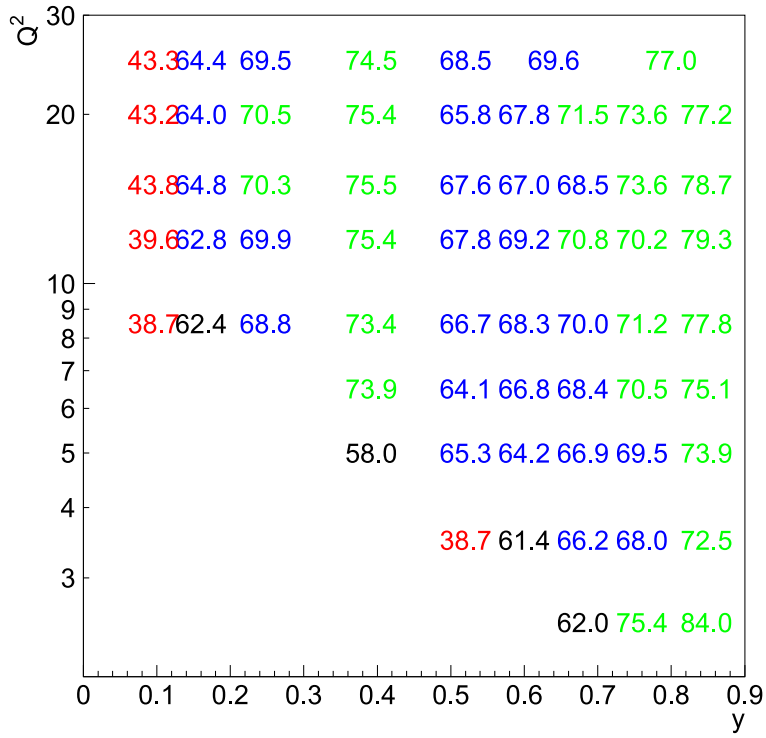


Figure 4.7: Purity P in per cent for each analysis bin for the medium energy running period.

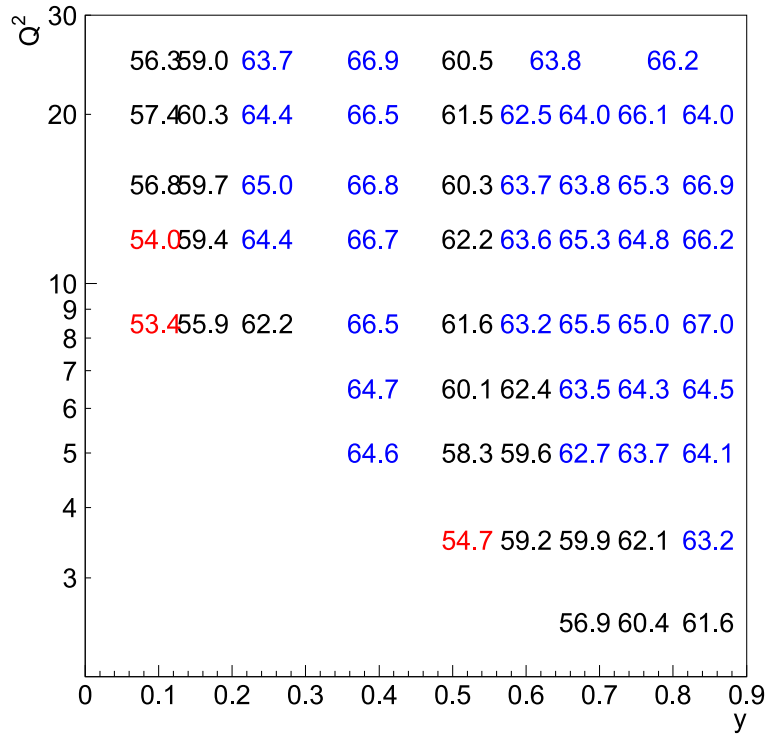


Figure 4.8: Stability S in per cent for each analysis bin for the medium energy running period.

5 Data Selection and Treatment

The determination of the DIS cross section relies on a comparison of the number of events for data and Monte Carlo sample in each analysis bin, as already explained in section 4.5. However employing this method of measurement is justified only if the efficiencies for the event selection and reconstruction are well described by the Monte Carlo simulation. To keep the fraction of background events small adequate selection criteria have to be applied. Additionally for the data the background contribution, which is estimated using wrong charge tracks (see section 4.4), has to be subtracted beforehand.

In the following chapter data treatment method including run and event selection, efficiency determination, alignment and cross section extraction is presented.

5.1 Data Samples

The nominal energy of the proton beam in the HERA collider is 920 GeV. As mentioned in section 2.7, the direct measurement of the structure function $F_L(x, Q^2)$ requires variation of the center of mass energy $s = 4E_e E_p$. Therefore, from January to June 2007 two additional data sets with lowered proton beam energies were taken. These are $E_p = 460$ GeV and $E_p = 575$ GeV, referred to as low and medium energy runs. The value 460 was chosen as a compromise to achieve lowest possible energy and to collect enough luminosity. The run with proton beam energy $E_p = 575$ GeV was chosen for an approximately equal span between the three resulting cross section measurements in y^2/Y_+ see equation 2.27.

For the $E_p = 920$ GeV measurement the data taken with the H1 detector in the years 1999 and 2000 have been used. The data collected in the year 2000 correspond to an integrated luminosity of 22 pb^{-1} . The cross section measurement for this year is restricted to the region of low and intermediate inelasticities y , where the background is low. In this domain the cross section is mostly identical to the proton structure function F_2 . About one order of magnitude in the photon virtuality, $10 \text{ GeV}^2 < Q^2 < 180 \text{ GeV}^2$, and three orders of magnitude in the Bjorken scaling variable, $1.3 \cdot 10^{-4} < x < 0.15$, are covered. The accuracy in this range is mainly limited by systematic uncertainties. None of the considered systematic error sources dominates the total uncertainty in the bulk of the measurement. Only at the lowest y the measurement is limited by the achieved control over measurement of the hadronic final state. The errors of the cross section measurement for this period are typically on the level of 2%, for details see [26]. An extension of the 920 measurement to lower $Q^2 < 12 \text{ GeV}^2$ is possible with the data obtained with the H1 detector in the year 1999. During this running period events were collected with a dedicated trigger on low Q^2 DIS events at the nominal interaction vertex position. The measurement was performed in a wide range of inelasticity y , from 0.0015

to 0.8. The collected data cover a Q^2 range from 0.2 to 12 GeV² and correspond to an integrated luminosity of 2.1 pb⁻¹ [2].

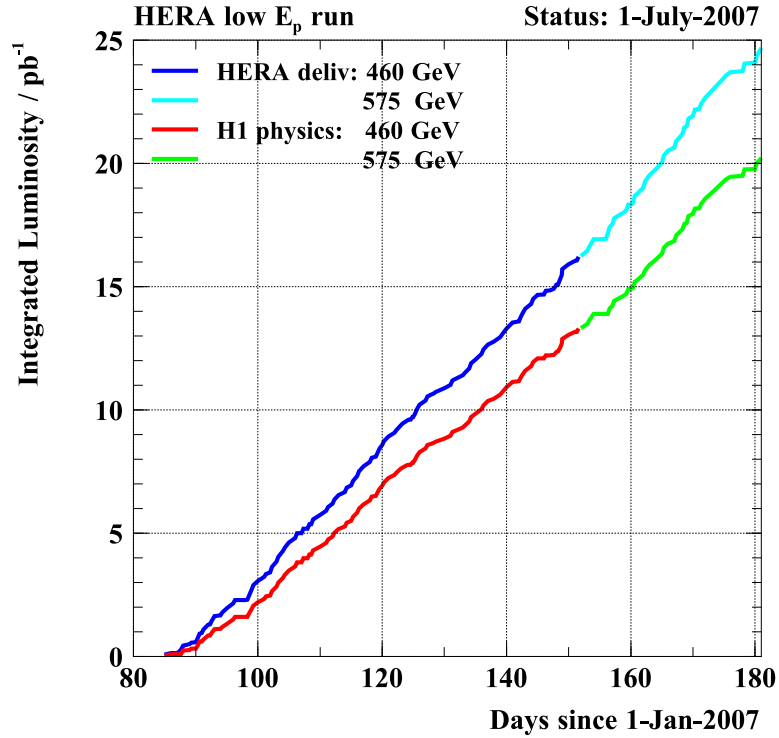


Figure 5.1: Total integrated luminosity provided by the HERA accelerator and collected by the H1 detector, during the low and medium energy running periods.

In figures 5.1 and 5.2 the luminosity collected by the H1 detector during the low and medium runs and the total integrated luminosity for the whole HERA running period are shown. A detailed summary of the analyzed data sets with used triggers and corresponding luminosities is presented in table 5.1.

	460 GeV	575 GeV
Run range	500918 – 507824	507843 – 511079
Trigger used	S7, S8	S7, S8
Luminosity pb ⁻¹	12.291	5.952
Date	26.03.07 – 1.06.07	1.06.07 – 30.06.07

Table 5.1: Data samples used in the presented analysis. The 3rd row depicts total integrated luminosity for the corresponding running period.

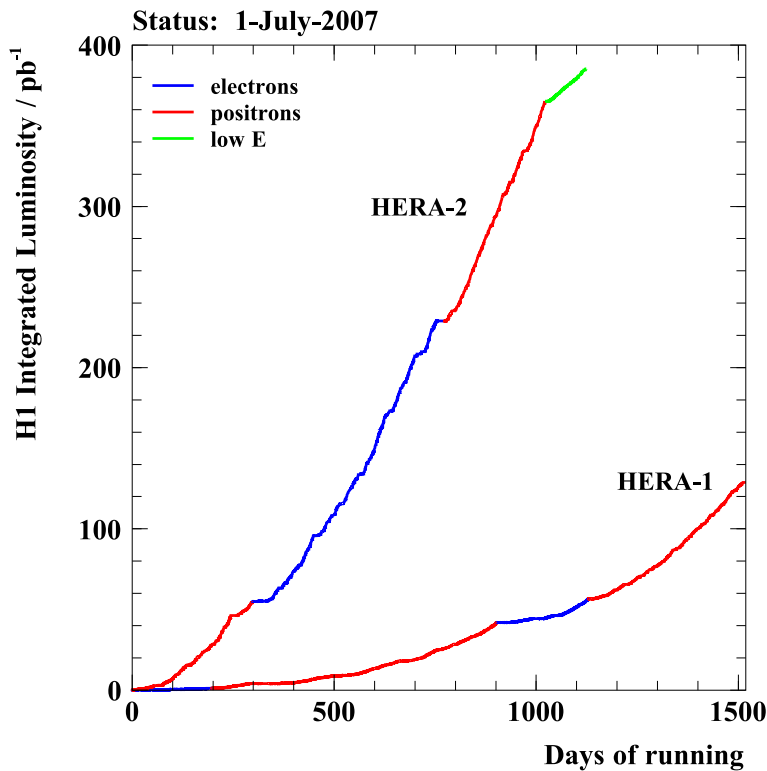


Figure 5.2: Total integrated luminosity collected by the H1 detector for the whole HERA running period.

5.2 Run Selection

The operation cycle of the HERA accelerator splits the stream of data into so-called luminosity fills. A luminosity fill begins as soon as first collisions between protons and leptons have been established and ends if one of the beams is dumped or lost. The duration of a luminosity fill is up to 12 hours and is limited by the life time of the electron beam. The H1 data acquisition system splits the data further into luminosity runs, which are sets of events collected under similar conditions. Each run contains typically 10,000 – 100,000 events and its duration is from a few minutes up to about one hour. One should mention, that various important pieces of information like beam or detector conditions are treated as being run dependent and are stored separately for different runs in the H1 database system.

The first step of the analysis is a preselection of runs. Only luminosity runs, when the detector was in a stable condition, are considered. This ensures that the hardware problems are not downgrading the quality of the measurement. In this analysis the following criteria were applied:

- **Hardware Status.** All relevant detector components must be operational and

included in the readout. If the high voltage of the subdetector is below its nominal value for a significant amount of time, it indicates instabilities, usually due to a large rate of background events. Therefore such runs are rejected. The same is done for runs in which one of the important readout branches has not been operating properly. The high voltage and readout status is checked for the subdetectors SpaCal, LAr, CJC, CIP, TOF, BST and the luminosity system.

- **Trigger Phase.** At the beginning of the luminosity fill the beam currents are high and the beam parameters are still optimised by the HERA shift crew. In this phase, which is called trigger phase 1, large prescale factors are applied to triggers as a response to the large beam induced background. At this time tracking detectors have still not reached their nominal high voltage settings. Once this is achieved a new run is started and trigger phase 2 is selected. To make optimal use of the limited bandwidth of the DAQ system the autoprescale procedure is used regularly at this stage. The procedure was tuned for low energy runs to select SpaCal triggers, allowing for very low values of prescales for subtriggers $s8$ and $s7$. Only runs with trigger phase 2 are considered in this analysis.
- **Run Quality.** According to the operation status of the main detector components each run is classified as good, medium or poor. In runs where the quality flag "Poor" has been assigned an obvious hardware or software problem was found. Such runs are excluded from the analysis. Furthermore short runs with a total luminosity of less than 1 nb^{-1} are rejected as well.

Due to readout problems with BST tracking detector, run range 508805 – 508913 is explicitly excluded from the analysis.

5.3 Stability Studies

An important check of the data quality is the measurement of the stability of the detector performance. This is typically done using the total event count per unit of luminosity, the so-called event yield, as a function of the luminosity fill or run number.

In addition to the standard event selection, the energy of the electron candidate for this study is required to be in a more restricted range of $15 \text{ GeV} < E'_e < 25 \text{ GeV}$, which ensures selection of events in the intermediate y domain, where the contribution of background is small and the vertex reconstruction efficiency the highest. To avoid variations of the mean and spread of the z -coordinate of the interaction vertex, an equal SpaCal acceptance for DIS events is required. This is satisfied by a restriction of the polar angle of the electron to the range $160^\circ < \theta_e < 172^\circ$. Figures 5.3 and 5.4 depict the event yield as a function of the run number for low and medium energy running periods, respectively. As can be observed, no significant deviations of the yield are observed, thus no additional run range is excluded except the one mentioned in the previous subsection.

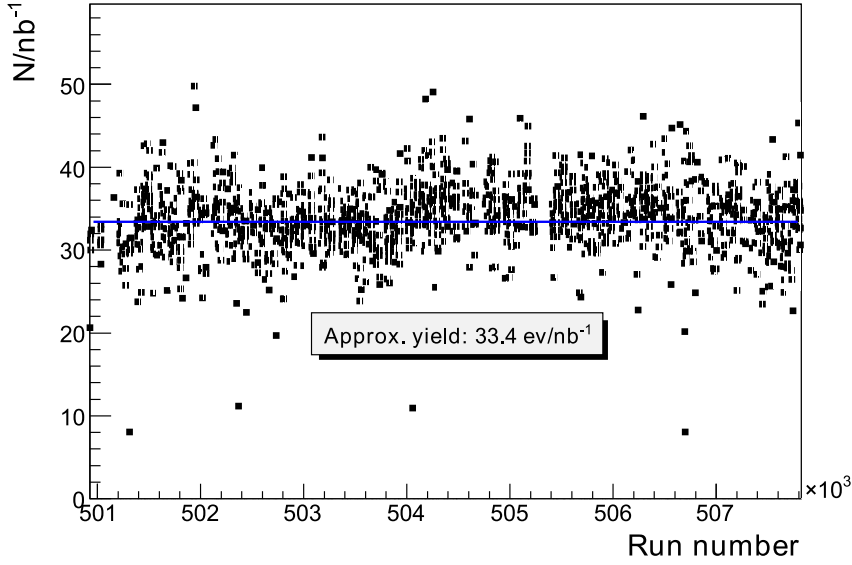


Figure 5.3: Event yield as a function of run number for the $E_p = 460$ GeV running period.

5.4 Online Event Selection

In the region of the kinematic phase space considered in this analysis the scattered electron is detected in the backward part of the H1 detector. Therefore the online event selection is mainly based on the energy depositions in the SpaCal calorimeter as counted by the Inclusive Electron Trigger (IET). The definition of the L1 subtriggers relevant for this analysis, their validation on L2 and efficiency are covered in the following subsection.

5.4.1 Subtrigger Definition

The L1 subtriggers used in the analysis are depicted in table 5.2. As can be seen all used subtriggers contain at least one of the SpaCal IET elements.

Subtrigger	L1 Definition	L2 Definition
S0	SPCLe_IET > 1	SPCL_R20
S7	SPCLe_IET > 0 & STT_R_gt_20 & STT_Spac_BST	–
S8	SPCLe_IET > 0 & STT_R_gt_20 & CIP_T0	–

Table 5.2: The definition of the subtriggers used in the analysis. The symbol & denotes logical AND operation.

For triggering purposes the SpaCal is segmented into groups of 2×2 readout cells,

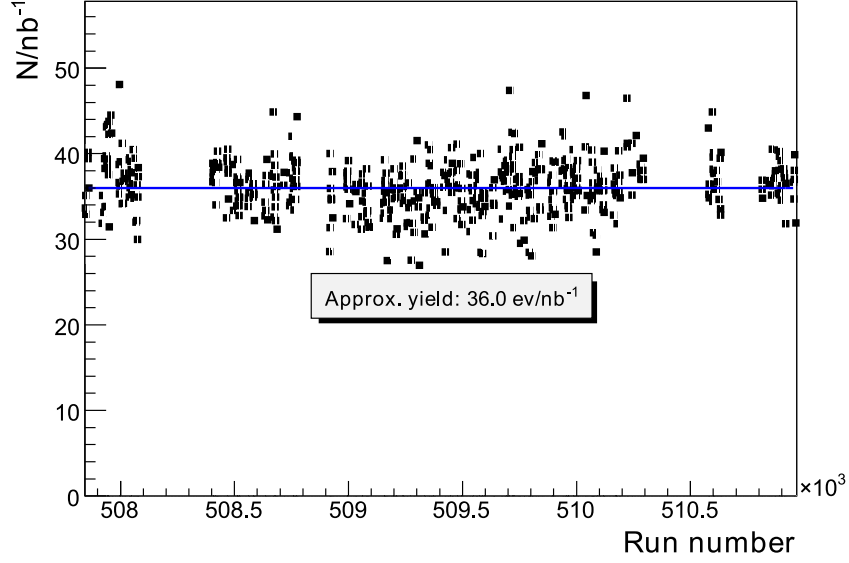


Figure 5.4: Event yield as a function of run number for the $E_p = 575$ GeV running period.

so-called trigger cells. The energy of a trigger cell is calculated by summing up energy depositions of the readout cells, which belong to it. Subsequently trigger cells are combined into 2×2 groups, into so-called cluster bits. Energy attributed to the cluster bit is compared to predefined thresholds. Information on whether the energy of a certain cluster bit exceeds the threshold is encoded in bit patterns. The bits of 4×4 cluster bits are combined with the logical operation OR to a so-called Local Inclusive Electron Trigger (LIET) region. If the energy of at least one cluster bit belonging to an LIET region exceeds a predefined threshold the bit of the corresponding LIET region is set.

IET elements considered in this analysis are: $SPCLe_IET > 0, 1$ corresponding to energies of the electron candidate of $E'_e > 2, 3$ GeV, respectively.

5.4.2 Trigger Efficiency

For the low y range ($y < 0.38$) the $s0$ subtrigger is used. Figure 5.5 depicts the efficiency of this trigger as a function of $x - y$ position of the electron cluster in the SpaCal calorimeter. The overall efficiency of the $s0$ trigger is close to 100%. An inefficient region for $X_{SpaCal} \approx -18$ cm and $Y_{SpaCal} \approx 18$ cm is excluded by a fiducial cut, see section 5.6.4.

The main condition used in the high y range ($y > 0.38$) is the logical OR combination of $s7$ and $s8$ subtriggers. The study of the efficiency of $s8$ and of the combination $s7$ OR $s8$ is performed without requiring a central vertex. Instead the Z_{vertex}^{BC} position determined by BCREC finder is used. Moreover kinematics are determined according to

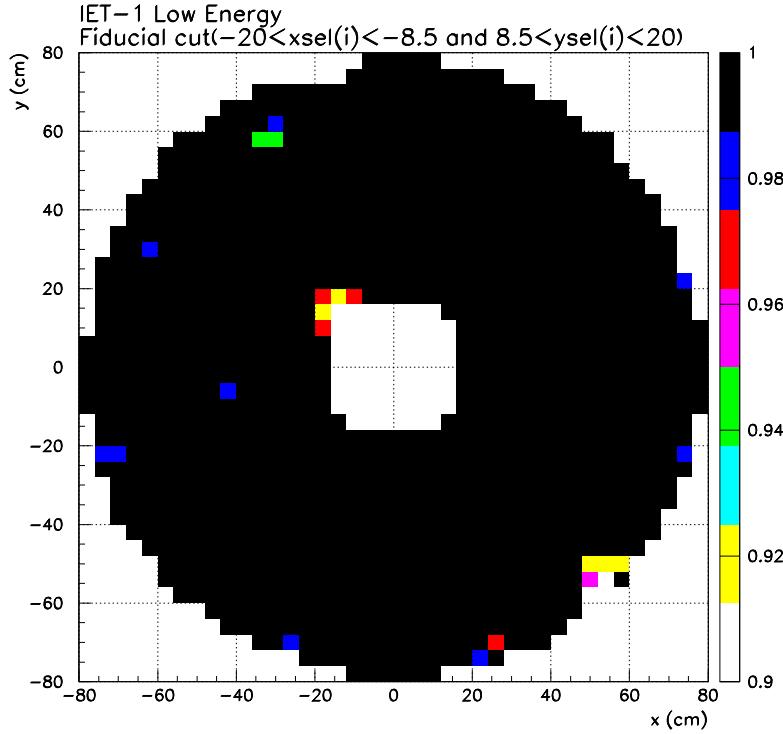


Figure 5.5: The efficiency of the trigger s_0 for the low energy running period plotted as a function of the electron cluster position in the SpaCal calorimeter.

Z_{vertex}^{BC} . As a monitor sample events selected by subtrigger s_0 are used. In figure 5.6 the inefficiency of trigger s_8 as a function of R_{SpaCal} is shown. As can be observed at low R_{SpaCal} inefficiency gets larger. The reason for this behaviour is the CIPT0 condition which is contained in s_8 , which reduces the efficiency at low R_{SpaCal} when the electron is outside the CIP acceptance. However, for the low radius s_7 recovers trigger efficiency and the overall efficiency of the combination of subtriggers is around 99%.

The trigger efficiency correction used in this analysis is a simple R -dependent function. For $R_{SpaCal} < 30$ cm a constant correction of $\epsilon_1 = 0.997$ is used. Similarly for $R_{SpaCal} > 44$ cm a constant of $\epsilon_2 = 0.987$ is applied. In the transition range $30 \text{ cm} < R_{SpaCal} < 44$ cm a linear function $\epsilon_3(R_{SpaCal}) = (\epsilon_2 - \epsilon_1)/(44 - 30) * (R_{SpaCal} - 30) + \epsilon_1$ is used.

5.5 Alignment

Precision measurements of the deep-inelastic cross section requires the kinematic variables to be reconstructed accurately. For this purpose the determination of the absolute detector positions is essential.

As introduced in section 3.2 the H1 detector coordinate system is defined by the central drift chambers in the Central Tracker. Therefore, all other subdetectors are aligned with respect to the central tracker. In this section the alignment check of the

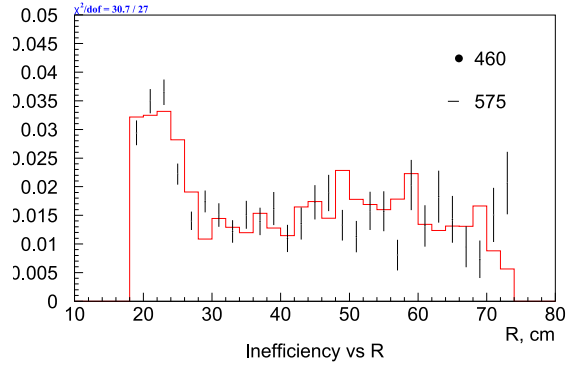


Figure 5.6: The inefficiency of the trigger $s8$ for the low energy running period (black dots) and for the medium energy running period (red histogram) plotted as a function of the electron cluster position in the SpaCal calorimeter.

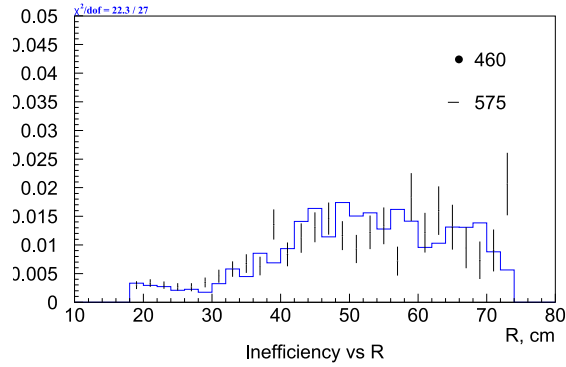


Figure 5.7: The inefficiency of the combination of triggers ($s7$ OR $s8$) for the low energy running period (black dots) and for the medium energy running period (blue histogram) plotted as a function of the electron cluster position in the SpaCal calorimeter.

backward calorimeter SpaCal is discussed.

5.5.1 SpaCal Alignment Check

The check of alignment of the SpaCal calorimeter is performed using QED Compton events. In these events the outgoing electron, which is almost parallel to the beam pipe due to the very low Q^2 transfer, radiates a real photon with rather large transverse momentum p_T . If $p_T \sim 4$ GeV both electron and photon are detected under large polar angles θ . Since their total p_T is close to zero, they enter the SpaCal almost back-to-back in azimuth. The procedure used for the determination of the alignment constants is based on an algorithm [17]. The principal idea of the algorithm is to connect both electron and photon SpaCal clusters in a sample of QED Compton events with lines

in the $x - y$ plane. The density of the lines connecting both clusters is largest at the (x, y) position where the beam crosses the SpaCal z -plane. Thus, variation of this point from the expected $(0, 0)$ position would indicate misalignment of the calorimeter. The summary of the cuts applied for QED Compton events selection is given in table 5.3.

Quantity	Comment
$A < 10^\circ$	Acoplanarity
$E_1 > 4 \text{ GeV}$	Energy of the scattered electron
$E_2 > 4 \text{ GeV}$	Energy of the photon
$E_1 + E_2 > 18 \text{ GeV}$	Total energy of the photon and the electron
$R_{log} < 5 \text{ cm}$	Logarithmic radius of the electron cluster
$ Z_{vertex} < 35 \text{ cm}$	z position of the central vertex

Table 5.3: The cuts used to select QED Compton events sample used for the SpaCal alignment.

Here the variable A , called acoplanarity, is defined as:

$$A = |180^\circ - \Delta\phi|, \quad (5.1)$$

where $\Delta\phi = |\phi_{electron} - \phi_{photon}|$ is a difference of azimuthal angles of the electron and the photon clusters.

The alignment check was performed for both low and medium energy running periods. Figures 5.8 and 5.9 depict the results. These histograms were fitted with a two-dimensional Gaussian function. In table 5.4 the summary of the alignment constants is given.

Running period	Δx [cm]	Δy [cm]
460	0.013 ± 0.002	0.012 ± 0.003
575	0.088 ± 0.003	0.038 ± 0.005

Table 5.4: The alignment constants for the SpaCal calorimeter determined using QEDC events.

As can be seen the density plot is centered around $(0, 0)$ coordinates, which implies that the detector is properly aligned. The precision of the alignment is better than 1 mm. Therefore, no additional correction for the detector position is applied.

5.6 DIS Event Selection

The aim of the event selection is to provide a sample of DIS events which contains only a small fraction of background events while keeping the number of selection criteria as limited as possible.

The background contribution to the cross section measurement comes mainly from photoproduction events and interaction of the beams with the residual gas molecules

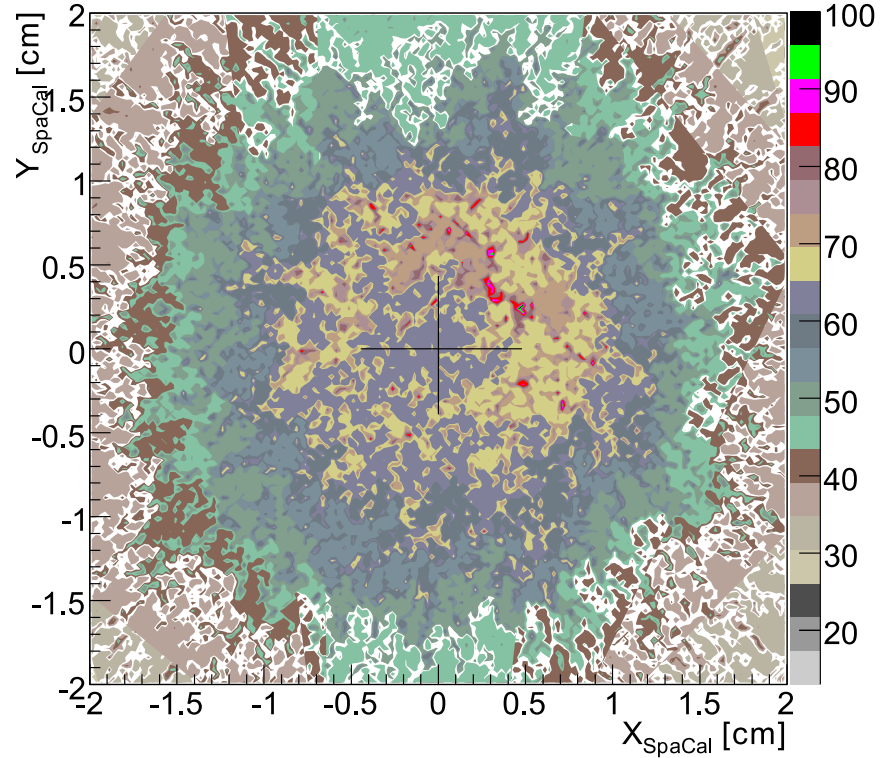


Figure 5.8: A density contour plot of lines connecting electron and photon clusters in a sample of QED Compton events for the low energy running period $E_p = 460$ GeV.

or the beam pipe walls. Most of the background is rejected during the online event selection.

In the following section selection criteria used to obtain a clean DIS sample are discussed. The summary of applied cuts is depicted in table 5.5. In table 5.6 the total number of events for data and Monte Carlo, before and after DIS selection, is shown.

5.6.1 Cluster Reconstruction in the SpaCal

As explained in section 4.3, the scattered electron is mainly identified by an electromagnetic cluster in the SpaCal. Reconstruction of the cluster starts from cells showing a local maximum of the energy deposition. Adjacent cells with an energy above a certain threshold are subsequently added to these seeds, forming a cluster. The main property of the cluster is its energy, calculated as a sum of all energy depositions in contained cells.

As the SpaCal is not segmented in the z -direction, for the spatial reconstruction, the

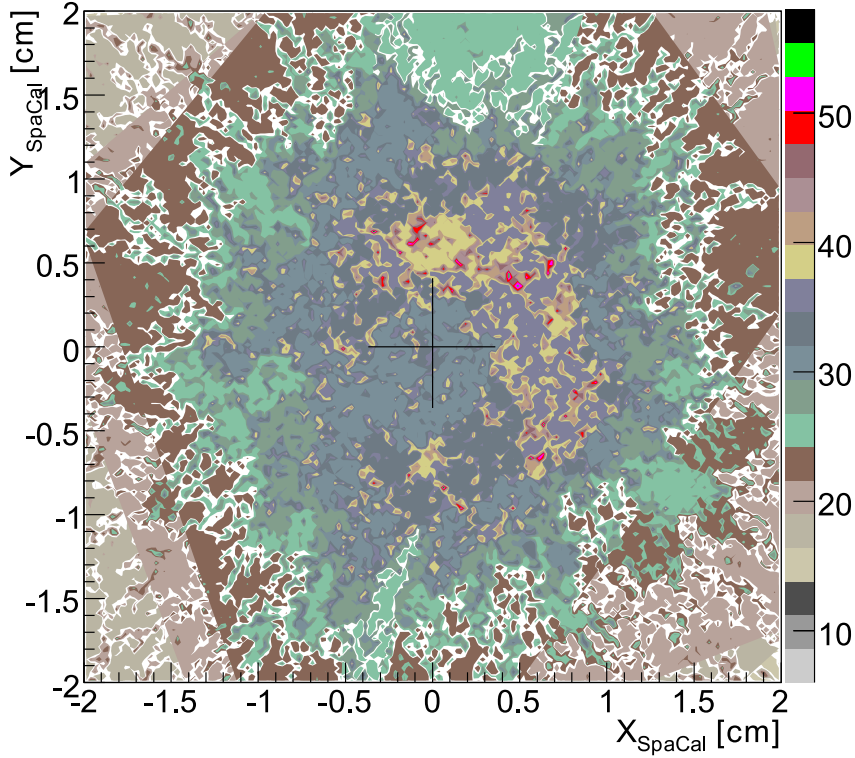


Figure 5.9: A density contour plot of lines connecting electron and photon clusters in a sample of QED Compton events for the medium energy running period $E_p = 575$ GeV.

Quantity	Subdetector	Comment
$3.4\text{GeV} < E'_e$	SpaCal	Electron candidate energy
$r_{log} < 5\text{cm}$	SpaCal	Photoproduction background reduction
$E_{had}/E'_e < 15\%$	SpaCal	Photoproduction background reduction
$(E - p_z)_{tot} > 28\text{GeV}$	combined	Photoproduction background and ISR reduction
$ z_{vtx} < 35\text{cm}$	Central Tracker	Precise θ_e , non ep background
$\Delta z_{vtx} < 8\text{cm}$	Central Tracker	
$Q^2 > 2.371\text{GeV}^2$	combined	Analysis phase space
$y > 0.1$	combined	
QED Compton	SpaCal	Anti-QED Compton events cut

Table 5.5: Summary of the cuts used to select DIS events.

Data	$E_p = 460$ GeV	$E_p = 575$ GeV
Total number of events	36,444,311	14,964,868
Number of events after DIS selection	414,125	239,500
Monte Carlo	$E_p = 460$ GeV	$E_p = 575$ GeV
Total number of events	14,999,984	14,999,984
Number of events after DIS selection	1,138,040	1,161,590

Table 5.6: Total number of events before and after DIS selection.

centre of gravity \vec{r} of the cluster, i.e. its position in the xy -plane, is used. The cluster position is calculated as a weighted sum over the position of its cells i

$$\vec{r} = \frac{\sum_i w_i \vec{r}_i}{\sum_i w_i}. \quad (5.2)$$

Weights w_i of the individual cell centres \vec{r}_i are determined taking into account their energy E_i according to the following relation

$$w_i = \max\left(0, w_0 + \ln \frac{E_i}{\sum_i E_i}\right), \quad (5.3)$$

which is called the logarithmic weighting scheme. As shown in [17] this scheme gives the best results for the position reconstruction. The cutoff parameter w_0 is setup to 4.8, which excludes cells below a certain energy threshold from the calculation.

As already mentioned the SpaCal has no segmentation in the z -direction and no information on lateral shower shape is available. Therefore, the z -position of the cluster is derived from a parameterisation:

$$z_{depth}[\text{cm}] = 0.001956 \cdot E_e'[\text{GeV}] + 0.8529 \cdot \ln(2479 \cdot E_e'[\text{GeV}]). \quad (5.4)$$

The variable z_{depth} is defined with respect to the SpaCal surface and corresponds to the depth of the particle shower. To first approximation it is assumed to depend logarithmically on the cluster energy E_e' . The absolute value of the z -coordinate can be calculated from z_{depth} taking into account the angle of incidence.

An additional quantity used for the reduction of the background from hadrons is the energy deposited behind the cluster in the hadronic section of the SpaCal, the so-called hadronic energy. The ratio of the hadronic energy and the total energy of the cluster, i.e. E_{had}/E_e' , is required to be less than 15%. Relevant distributions of E_{had}/E_e' and r_{log} , with values of cuts used in this analysis, are shown in figure 5.10.

5.6.2 Event Vertex

Precise reconstruction of the event vertex is essential for the determination of the kinematics. In particular the z -position of the vertex is directly used for the measurement of the polar angle of the scattered electron θ_e . Depending on the kinematic domain the vertex can be determined using electron track or hadronic final state particles.

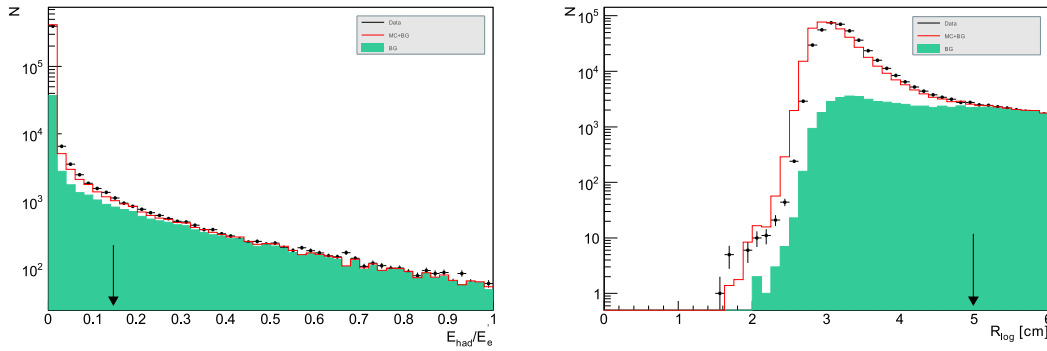


Figure 5.10: Distribution of hadronic fraction and logarithmic cluster radius with cuts denoted by arrows.

In the presented analysis the primary vertex reconstructed by the Central Tracker is used. The estimated precision of the z -coordinate measurement is required to be better than $\Delta z_{vtx} < 8$ cm. This requirement rejects badly reconstructed events. The z -position of reconstructed event vertex is restricted to the range $|z_{vtx}| < 35$ cm, which rejects contributions from the satellite bunches and background processes, such as cosmic or beam induced background. The requirement corresponds approximately to 3σ of the gaussian z_{vertex} distribution, which is expected for the ep physics interactions.

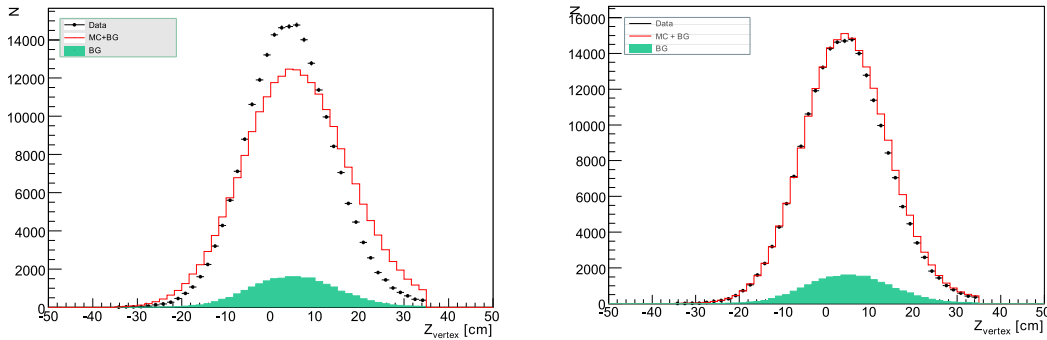


Figure 5.11: Z vertex distributions for data and Monte Carlo events before and after reweighting of the MC. The simulation is normalised to the luminosity.

Due to the longitudinal size of the proton and electron bunches, which are $\sigma_z(p) \approx 13$ cm and $\sigma_z(e) \approx 2$ cm respectively, the primary vertex is spread out in z around the nominal interaction point. The distribution of the z vertex is approximately Gaussian, with mean depending on the beam settings of the accelerator. In figures 5.12 and 5.13 the mean and spread of the z vertex distribution for the low energy running period as a function of run number are depicted.

For practical reasons the Monte Carlo events are simulated with a fixed z vertex

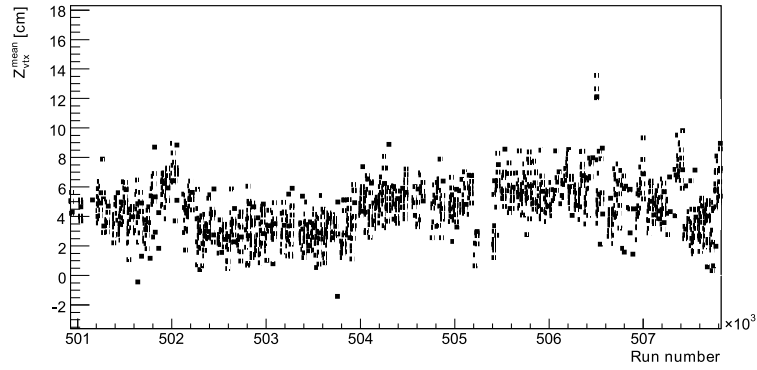


Figure 5.12: Mean of Z_{vertex} as a function of run number for the low energy running period.

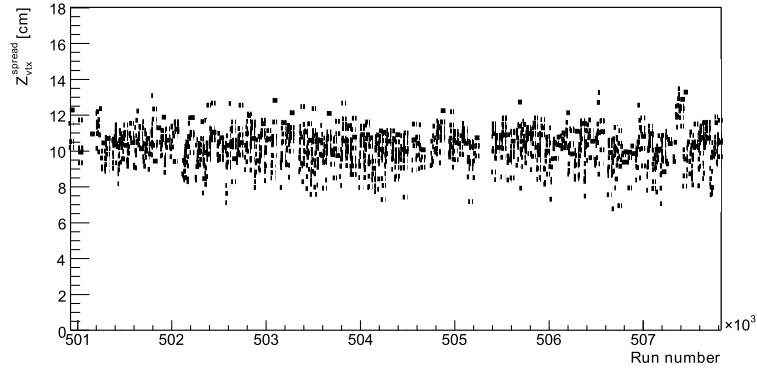


Figure 5.13: Spread of Z_{vertex} as a function of run number for the low energy running period.

distribution corresponding to a Gaussian function with a mean $z_{mean}^{MC} = 0.01$ cm and a spread $\sigma^{MC} = 13$ cm. To match the data distribution simulated events are reweighted in z . For this purpose unbiased z_{vertex} distributions are determined for data and MC and fitted with a smooth function. A typically chosen function is a Gaussian plus a 10th order polynomial to properly fit the tails of the distribution in the range $|z_{vertex}| < 40$ cm. These functions are normalised to contain the same number of events in the considered interval and the factor $(z_{vertex}^{Data}/z_{vertex}^{MC})$ is used as an additional event weight in the Monte Carlo depending on the generated position of the vertex $z_{vertex,gen}^{MC}$, as long as its value is in $|z_{vertex}| < 40$ cm interval.

The z vertex distribution of the data and Monte Carlo events before and after reweighting is shown in figure 5.11

5.6.3 Hadronic Final State

The DIS selection used in this analysis requires $(E - p_z)_{tot} > 28$ GeV. This condition reduces initial state radiation effects and the contribution from the photoproduction background. The HFS consists of typically many particles with complicated topologies. Therefore, due to possible ambiguities, the reconstruction is usually not straightforward. In this section some details concerning the HFS identification are presented.

The inclusive hadronic final state is reconstructed using information from the LAr calorimeter, Central Tracker and the SpaCal calorimeter. The reconstruction is performed by the HFS finder within the H100 framework [21], using the HADROO2 algorithm [33]. In the first step a cone in the SpaCal around the electron candidate cluster is excluded. The cone axis is defined by the vertex position and the centre-of-gravity of the SpaCal cluster. Other particles, including electron candidates and muons which are not flagged as isolated, are considered as belonging to the hadronic final state and are added to the initial list of selected particle candidates.

The algorithm starts with the list of selected tracks and clusters. The aim is to combine track and cluster measurements, both of which exist for charged particles, in order to obtain an optimal reconstruction of the HFS. For charged particles the resolution of each track is compared to the expected resolution for a calorimeter deposit of the corresponding energy and is used to decide which measurement is taken. The fact that the resolution of tracking detectors decreases with an increase of the track momentum, while the relative resolution of the calorimeters improves, is taken into account. Only the vertex-fitted tracks measured in the Central Tracker are considered.

To decide which measurement should be used, the tracks are associated with a cluster by extrapolating the track up to the calorimeter surface, using a helix parameterization. Inside the calorimeter tracks are approximated by a straight lines. The calorimetric energy $E_{cylinder}$ is calculated as the sum of all clusters inside a cone of 67.5° and two cylinders of radius 25 cm in the electromagnetic and 50 cm in the hadronic section. Afterwards, the calorimeter energy $E_{cylinder}$ is compared to the track energy E_{track} . The resolution of track energy is given by the following formula:

$$\frac{\sigma_{E_{track}}}{E_{track}} = \frac{1}{E_{track}} \sqrt{\frac{P_{T,track}^2}{\sin^4 \theta} \cos^2 \theta \sigma_\theta^2 + \frac{\sigma_{P_T}^2}{\sin^2 \theta}}, \quad (5.5)$$

where σ_{P_T} and σ_θ are errors on P_T and θ of the track. The error on the calorimetric measurement is given by the hadronic energy resolution:

$$\frac{\sigma_e}{E} = \frac{\sigma_{E,expectation}}{E_{track}} = \frac{0.5}{\sqrt{E_{track}}}. \quad (5.6)$$

The estimated uncertainties of the track and calorimetric measurements are compared. If the following relation holds:

$$\frac{\sigma_{E_{track}}}{E_{track}} < \frac{\sigma_{E,expectation}}{E_{track}}, \quad (5.7)$$

the track measurement is used to make a particle candidate and the four-vector of the

particle is set to E_{track} . If the calorimetric measurement is better the calorimeter energy is used and the energy is set to $E_{cylinder}$. The track together with its associated cluster is removed from the input list and the algorithm continues with the next track.

Once all tracks are considered, the remaining particles are reconstructed by the calorimetric measurements only. These particles correspond either to neutral particles or to charged particles with a wrongly measured or non-reconstructed track.

5.6.4 Fiducial Cuts

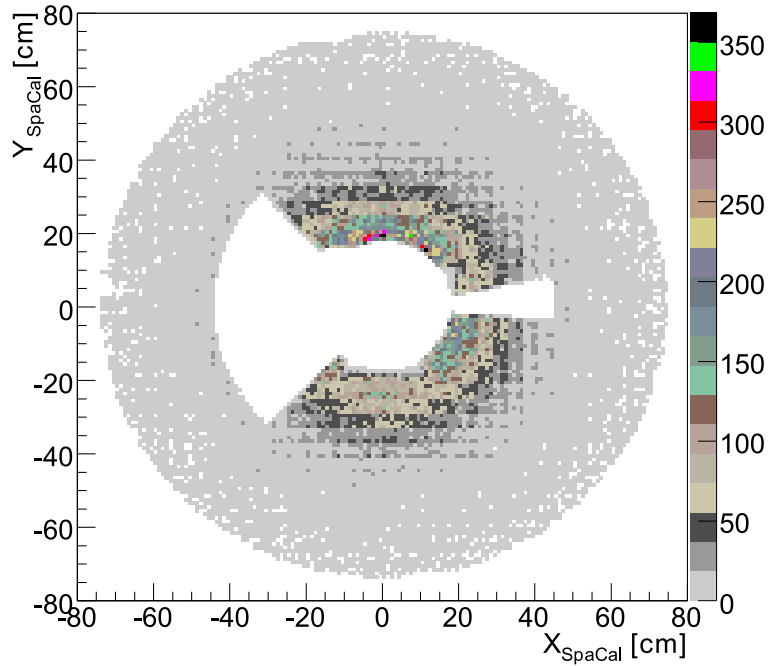


Figure 5.14: Position of the SpaCal cluster in $X - Y$ plane. The gap for $|\phi| > 135^\circ$ corresponds to BST geometry. The region with $\phi \sim 0^\circ$ is excluded due to inefficient BST sectors.

The fiducial cuts ensure the precise identification of the scattered electron. To obtain reliable measurements of the cluster position, good resolution and correct electron identification, inefficient regions have to be explicitly excluded. The fiducial volume definition is applied according to the impact position of the scattered electron.

Figure 5.14 depicts the distribution of the electron candidate position in the SpaCal calorimeter in $x - y$ plane. As can be seen the complicated fiducial volume cut is applied according to the following:

- **Geometrical acceptance of the SpaCal** – $18 \text{ cm} < R_{SpaCal} < 74 \text{ cm}$.

- **Geometrical acceptance of the BST** – $-134^\circ < \phi < 134^\circ$.
- **Geometrical acceptance of the CJC in BST ϕ range** – $R_{SpaCal} > 45$ cm.
- **Inefficient BST sectors** – the region excluded: $-2^\circ < \phi < 15^\circ$.
- **Trigger inefficiency** – the region excluded: -16 cm $< X_{SpaCal} < 9$ cm && -9 cm $< Y_{SpaCal} < 16$ cm.

5.7 Track Linking Efficiency

One of the main selection criterion used in this analysis is the requirement for the track matching to the electromagnetic cluster. Moreover, the sign of the charge of the reconstructed track is used for background determination. Therefore, determination of the efficiency of the track linking and correct implementation in the Monte Carlo simulation is crucial.

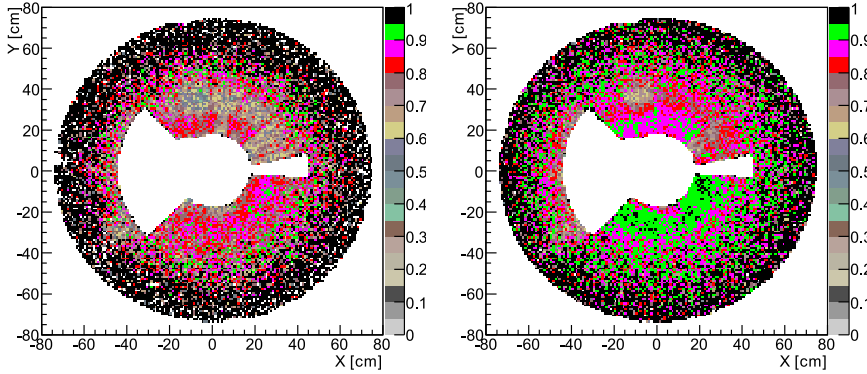


Figure 5.15: Track linking efficiency for data (left plot) and Monte Carlo simulation (right plot) for the low energy running period as a function of the electron cluster position in the SpaCal calorimeter.

The efficiency of the track link requirement is defined as follows:

$$\epsilon_{track} = \frac{\text{Events with associated track}}{\text{All events}}, \quad (5.8)$$

where the denominator includes also events with no track linked to the electron candidate cluster.

The track is associated with an electromagnetic cluster if the following criteria are satisfied:

- distance between the center of gravity of the cluster and extrapolation of the track

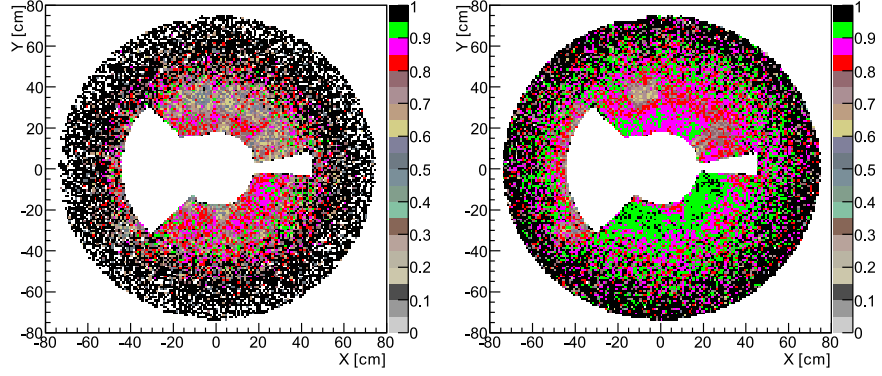


Figure 5.16: Track linking efficiency for data (left plot) and Monte Carlo simulation (right plot) for the medium energy running period as a function of the electron cluster position in the SpaCal calorimeter.

to the SpaCal surface is below 4 cm:

$$D = \sqrt{(X_{spacal} - X_{track})^2 + (Y_{spacal} - Y_{track})^2} < 4\text{cm} \quad (5.9)$$

- number of BCREC space points is at least 2,
- R_{cjc} (R_{spacal} for -112.5 cm) and R_{bst} (R_{spacal} for -50 cm) dependent requirement on the number of hits:
 - number of CJC hits > 9 , for $R_{cjc} > 40$ cm,
 - number of CJC hits has a linear dependence on R_{cjc} : $N_{cjc} > R_{cjc} - 30$ (for the transition range between BST and CJC, i.e. $30 \text{ cm} < R_{cjc} < 40 \text{ cm}$,
 - number of CJC hits < 15 , for the BST range acceptance $R_{cjc} < 30$ cm,
 - number of BST hits at least 2, for BST range acceptance $R_{bst} < 13$ cm.

The efficiency is determined for both data and Monte Carlo. The overall efficiency for data is about 85%, for the Monte Carlo the value is higher and exceeds 92%. Consequently the MC events are weighted according to the ratio of the efficiencies for data and MC.

The efficiency correction is applied as a function of both R_{SpaCal} and ϕ_e . For R_{spacal} corresponding to the acceptance of the BST tracker, the SpaCal surface is divided into twelve ϕ regions with 2 cm steps in R_{SpaCal} . In the transition region $30 \text{ cm} < R_{SpaCal} < 54 \text{ cm}$, thirteen ϕ sectors with 2 cm R_{SpaCal} step are used. Here the thirteenth sector corresponds to the range $\phi_e < -134^\circ$, $\phi_e > 134^\circ$. In the CJC acceptance range no segmentation in ϕ_e is used and the correction is only R_{SpaCal} dependent.

5.8 Cross Section Results

5.8.1 Control Distributions

Figures 5.17 to 5.20 demonstrate the agreement between data and Monte Carlo simulation for the quantities reconstructed in the analysis. The data is compared to the sum of the prediction of DJANGO for the DIS signal and background estimated using wrong sign tracks. The normalisation is adjusted according to the luminosities of the DJANGO sample and the data sample. Appropriate charge asymmetry factors are applied for the background sample and negative charge Monte Carlo. The Monte Carlo simulation is reweighted to the H1 PDF 2009 parameterization.

In figures 5.17 and 5.19 a sets of control plots related to the scattered electron for the low and medium energy running periods, respectively, are shown. Figures 5.18 and 5.20 depict other quantities like Z_{vertex} distribution and basic track parameters reconstructed by the combined electron finder. In general good agreement between data and Monte Carlo simulation is observed. The distribution of the azimuthal angle ϕ_e reflects the complicated fiducial cut used in the analysis. The drop in ϕ_e distribution for $\approx 0^\circ$ is related to inefficient BST sectors excluded from the analysis. Good agreement between data and MC for the E'_e distribution indicates proper calibration of the electromagnetic energy. Similarly the Monte Carlo simulation for all kinematic variables describes the data well.

5.8.2 Uncertainties

The uncertainties quoted for the cross-section determination are presented in this subsection. In general they can be divided into four different categories:

- **Statistical errors** - Statistical uncertainty of the data depends on the kinematic region and the running period.
- **Correlated systematic errors** - Sources of systematic errors classified as correlated have influence on the cross section measurement in different analysis bins in a correlated way. Typical example of correlated error is the energy scale of the scattered electron, since it affects different bins in a similar way.

The method used for the determination of the correlated systematic errors is the following: for each of the sources the relevant quantities i are varied in a positive and negative direction, σ_r^{i+} and σ_r^{i-} . The reduced cross sections for the former σ_r^+ and latter case σ_r^- are redetermined and the relative systematic uncertainty is evaluated as

$$\delta_i = \frac{\sigma_r^{i+} - \sigma_r^{i-}}{2\sigma_r^0}, \quad (5.10)$$

where σ_r^0 denotes the reduced cross section from the nominal analysis.

- **Uncorrelated systematic errors** - Influence the measurement independently in each bin. A typical source of uncorrelated error is the available MC statistics.
- **Global normalisation uncertainties** - Affect all measurements by the same amount. The most important global normalisation error is the luminosity uncertainty.

Source	Uncertainty
Energy scale	0.4% at 27.6 GeV linearly to 1% at 1 GeV
θ_e	1 mrad
LAr scale	4%
LAr noise	15%
Hadronic SpaCal scale	0.5 GeV

Table 5.7: Sources of systematic errors for the presented analysis.

Source	Uncertainty	
	$y > y_{trans}$	$y < y_{trans}$
Trigger efficiency	1%	0.5%
Track link efficiency	2%	2%
Charge determination efficiency	2x1%	2x1%
Electron ID efficiency	2%	0.5%
Background asymmetry	2%	2%

Table 5.8: Sources of systematic y -dependent errors for the presented analysis, where $y_{trans} = 0.38$.

The value of the total uncertainty δ_{tot} of a measurement is given as a quadratic sum over all sources of the uncertainties

$$\delta_{tot} = \sqrt{\sum_i (\delta_{cor}^i)^2 + \delta_{unc}^2 + \delta_{sta}^2}. \quad (5.11)$$

The systematic uncertainty on the cross section is derived from various contributions. The uncertainties leading to kinematic correlations are:

- The uncertainty on the SpaCal electromagnetic energy scale, estimated with the double-angle method, is 0.4% at the kinematic peak degrading to 1% at 1 GeV energy. This is verified at the kinematic peak, where E_e' has to be close to E_e , and at lower energies with $\pi^0 \rightarrow \gamma\gamma$, $J/\Psi \rightarrow e^+e^-$ decays and with elastic QED Compton events.
- The uncertainty on the electron polar angle is 1 mrad, estimated using independent track information from the BST and the CJC.

- The hadronic energy scale, calibrated using electron-hadron transverse and longitudinal momentum balance, has an uncertainty of 4%.
- The background charge asymmetry is known to 2% based on studies of wrong charge data in $e^\pm p$ scattering and tagged photoproduction events.
- The central track-cluster link efficiency is verified with an independent track reconstruction using BST and CJC hit information. The uncertainty of this link efficiency combined with the interaction vertex reconstruction efficiency is estimated to be 2%.
- The hadronic SpaCal calibration utilises the conservation of $E - p_z$. Hadronic SpaCal scale uncertainty is estimated to be 0.5 GeV.
- A topological finder is used to identify and subtract LAr noise. The fraction of hadronic energy attributed to noise is described by the simulation to within 15%, which is taken as a systematic uncertainty.

The uncorrelated systematic uncertainties originate from the Monte Carlo statistical errors and from the following sources:

- The uncertainty on the charge measurement is determined from data to Monte Carlo comparisons at low y and cross checked with radiative events which are background free in the low energy region. As the charge misidentification causes signal events to be subtracted as background, a 1% uncertainty on σ_r is obtained.
- The trigger efficiency, determined from independent monitor triggers, is known to within 1% for the combined CIP-SpaCal trigger and 0.5% for the inclusive SpaCal trigger.
- Comparisons between different electron identification algorithms and between data and simulations yield an estimated uncertainty of 2% (0.5%) on the electron identification at high (low) y in the SpaCal calorimeter.

A summary of the systematic errors having influence on the cross section measurement is presented in tables 5.7 and 5.8. For full error tables of the measurement see Appendix A.

5.9 $F_L(x, Q^2)$ Determination

As already discussed in chapter 2 the longitudinal proton structure function $F_L(x, Q^2)$ is extracted from the measurements of the reduced cross section as the slope of σ_r versus y^2/Y_+ , see equation 2.27. The procedure is demonstrated in figure 2.5, where for a fixed Q^2 and x , σ_r is a linear function of y^2/Y_+ . Lowest values of x are generally accessed by combining only $E_p = 920$ GeV and $E_p = 575$ GeV measurements. At larger x , cross sections from all three data sets are available.

5 Data Selection and Treatment

The technique of the measurement used in the current analysis permits the F_2 structure function to be determined as well. The measurement of $F_2(x, Q^2)$ is shown in figure 5.25, the values are listed in tables 5 and 6. Similarly the F_2 measurement is compared to the H1 PDF 2009 fit [27]. For the highest Q^2 bins in the high y region the measurements slightly exceed the model. In general the data are in good agreement with the F_2 parameterization.

The measurement of $F_L(x, Q^2)$ is shown in figure 5.26, the values are listed in tables 5 and 6. Statistical and total uncertainties of the measurement are depicted. The data are compared to the H1 PDF 2009 parameterization. Within the experimental errors the data are consistent with the predictions. Only for higher Q^2 bins of 20 GeV² and 25 GeV² do the data undershoot the prediction, where the experimental errors are large. This result is consistent with other determinations of F_L [1].

In general the new measurement of the structure function F_L is in good agreement with the NLO QCD predictions [27] for $Q^2 \geq 12$ GeV² data. This provides an independent cross check of DGLAP equations validity. The direct measurement of $F_L(x, Q^2)$ will improve the gluon determination. The precise knowledge of the gluon density for $x \approx 0.005$, corresponding for HERA kinematics to $Q^2 > 10$ GeV² range, is used for the prediction of W , Z as well as light Higgs production rates at the LHC. The measurements for $2.5 \text{ GeV}^2 \leq Q^2 \leq 8.5 \text{ GeV}^2$ access the region where the higher order QCD corrections become large and various models give different predictions [39]. The direct measurement of $F_L(x, Q^2)$ will help to discriminate between theories. The determined precision of the cross section measurement is on the level of 2-5% and the overall precision of the longitudinal proton structure function F_L determination is about 0.1.

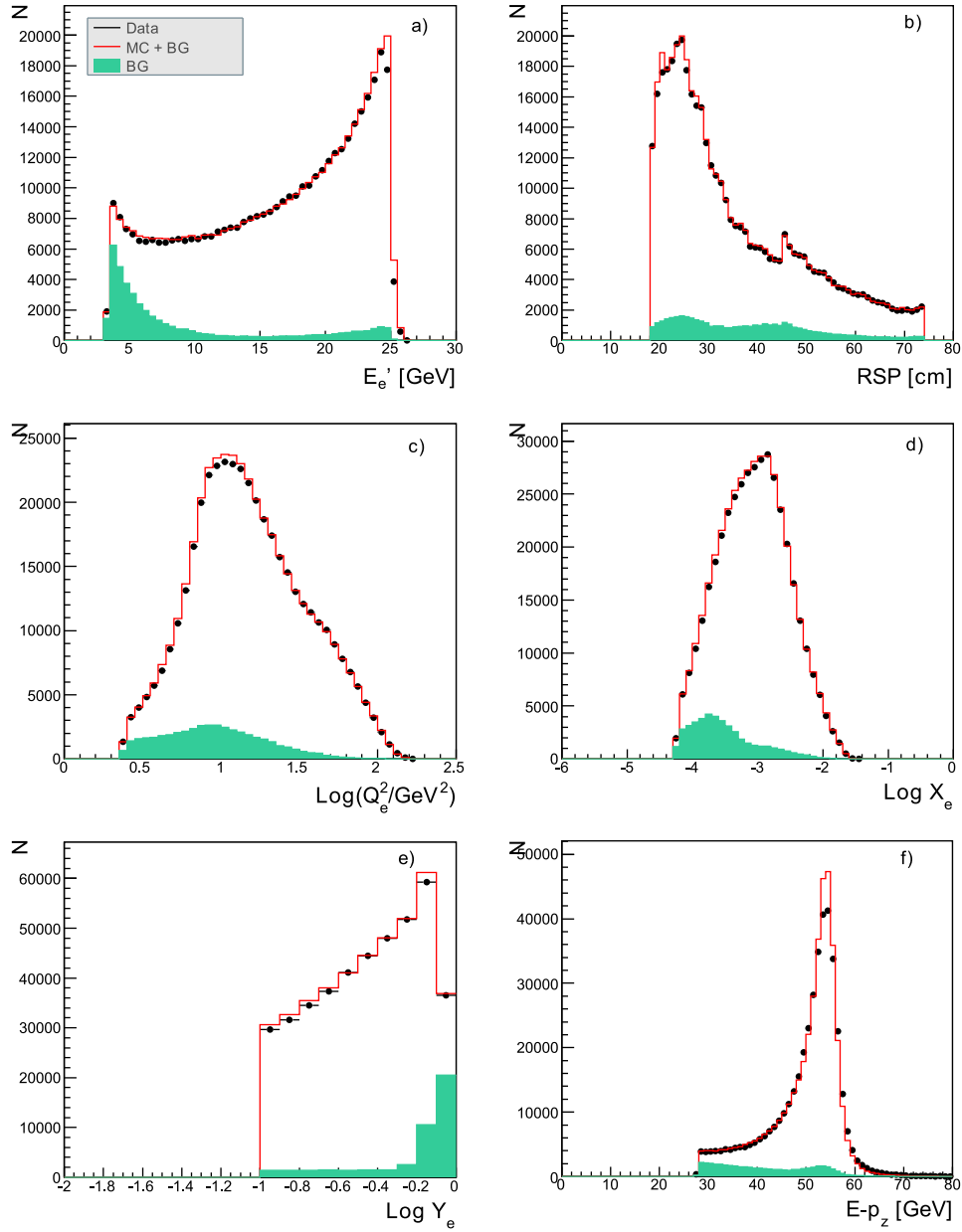


Figure 5.17: Control distributions related to the scattered electron for the low energy running period. Dots represent the data, the full histograms depict the prediction of the simulation, the green histograms denote background determined with the wrong sign tracks. The normalisation is adjusted to the luminosity. a) energy of the scattered electron, b) radius in SpaCal, c) squared momentum transfer, d) Bjorken- x , e) inelasticity, f) energy, longitudinal momentum difference.

5 Data Selection and Treatment

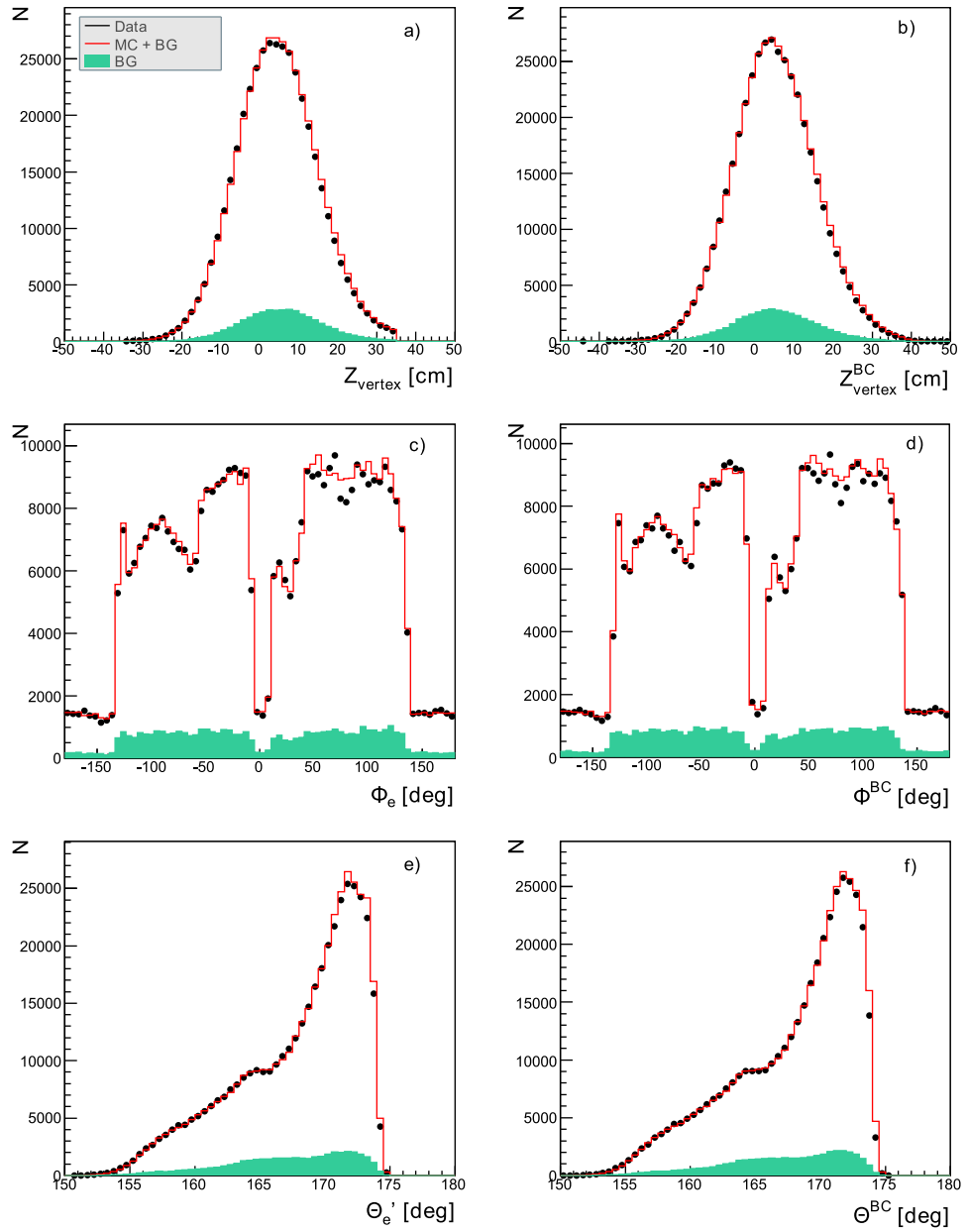


Figure 5.18: Control distributions of other basic observables for the low energy running period. Dots represent the data, the full histograms depict the prediction of the simulation, the green histograms denote background determined with the wrong sign tracks. The normalisation is adjusted to the luminosity. a) Z_{vertex} distribution, c) azimuthal angle of the electron, e) polar angle of the electron. Histograms b), d) and f) show distributions of the corresponding variables determined with the combined electron finder.

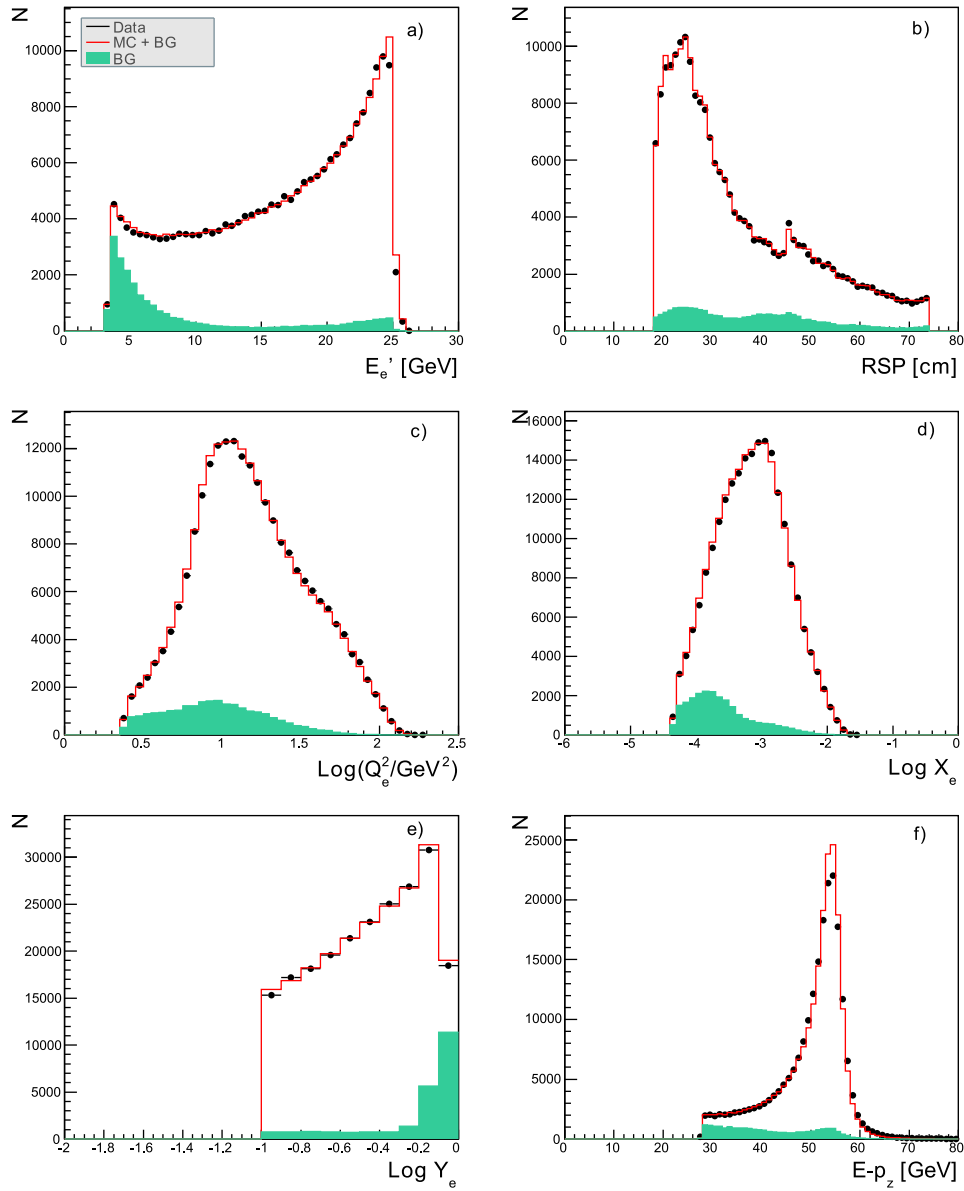


Figure 5.19: Control distributions related to the scattered electron for the medium energy running period. Dots represent the data, the full histograms depict the prediction of the simulation, the green histograms denote background determined with the wrong sign tracks. The normalisation is adjusted to the luminosity. a) energy of the scattered electron, b) radius in SpaCal, c) squared momentum transfer, d) Bjorken- x , e) inelasticity, f) energy, longitudinal momentum difference.

5 Data Selection and Treatment

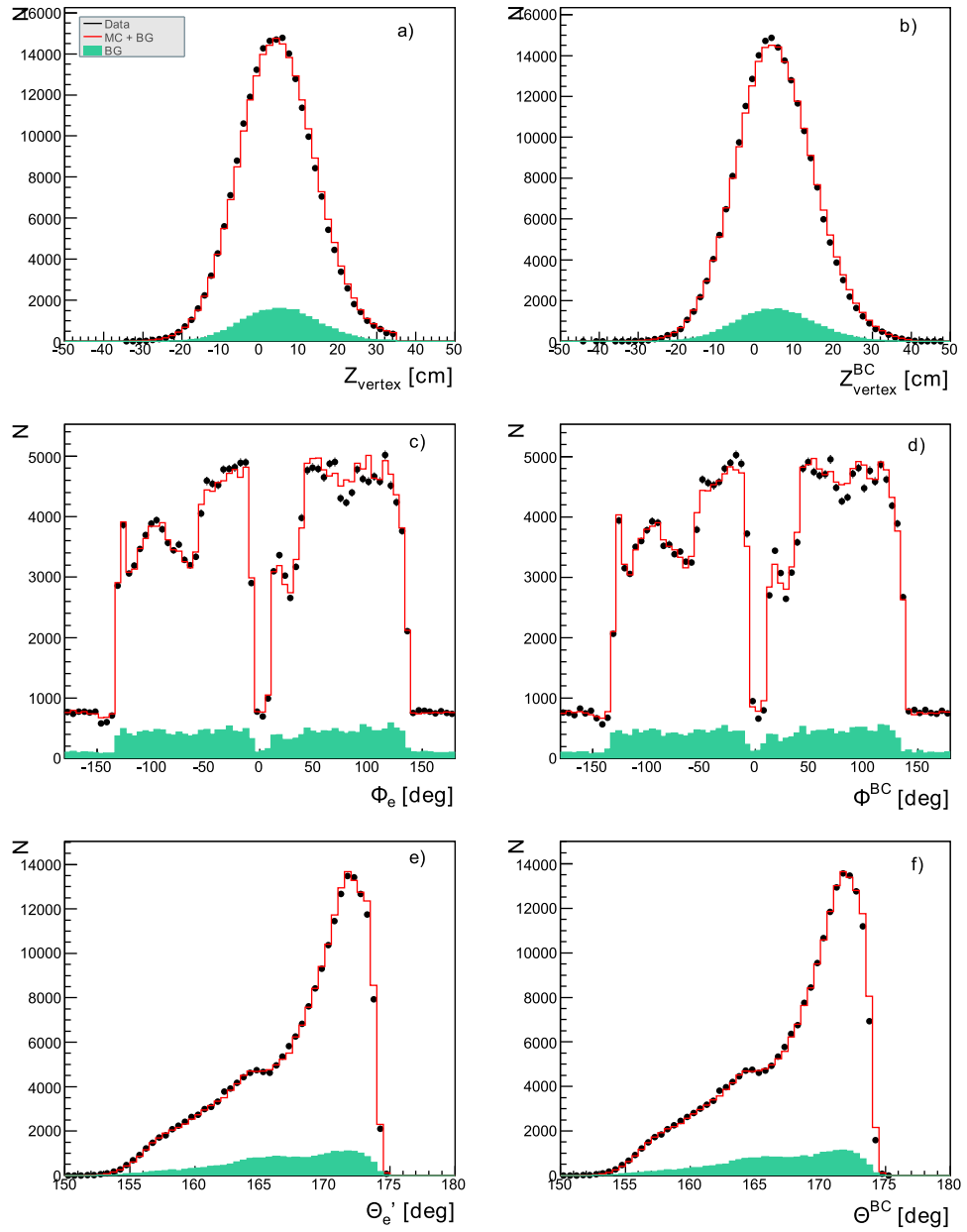


Figure 5.20: Control distributions of other basic observables for the medium energy running period. Dots represent the data, the full histograms depict the prediction of the simulation, the green histograms denote background determined with the wrong sign tracks. The normalisation is adjusted to the luminosity. a) Z_{vertex} distribution, c) azimuthal angle of the electron, e) polar angle of the electron. Histograms b), d) and f) show distributions of the corresponding variables determined with the combined electron finder.

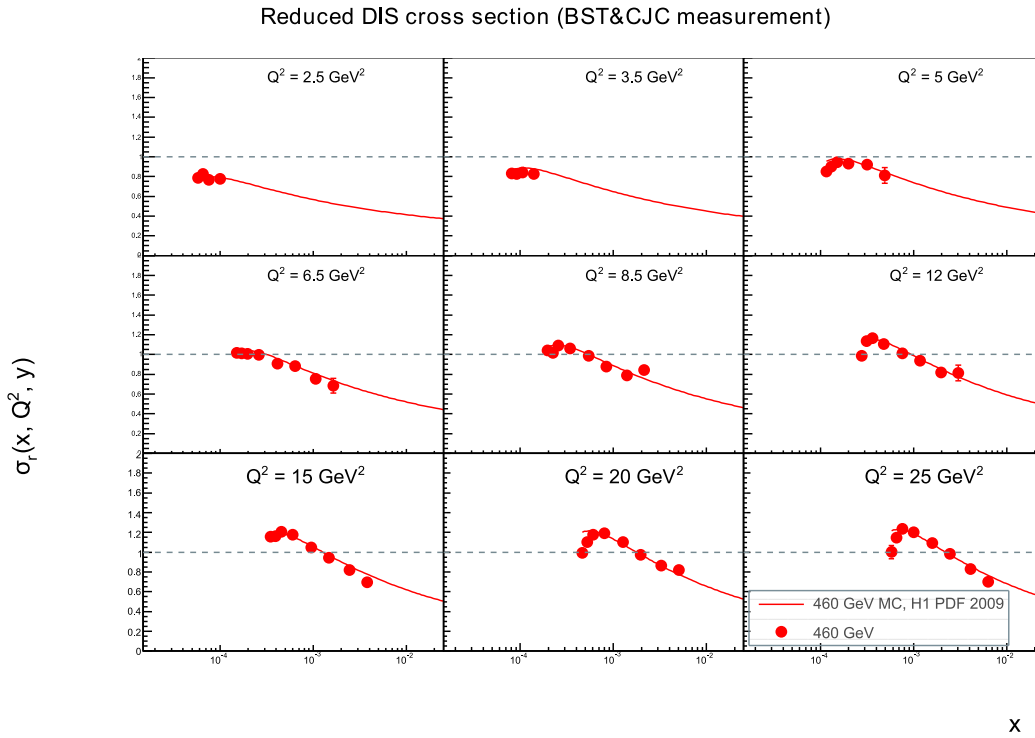


Figure 5.21: The measurement of the reduced cross section σ_r as a function of Bjorken- x for various Q^2 bins for the low energy running period. The error bars represent the statistical uncertainties. The data is compared with the H1 PDF 2009 parameterization.

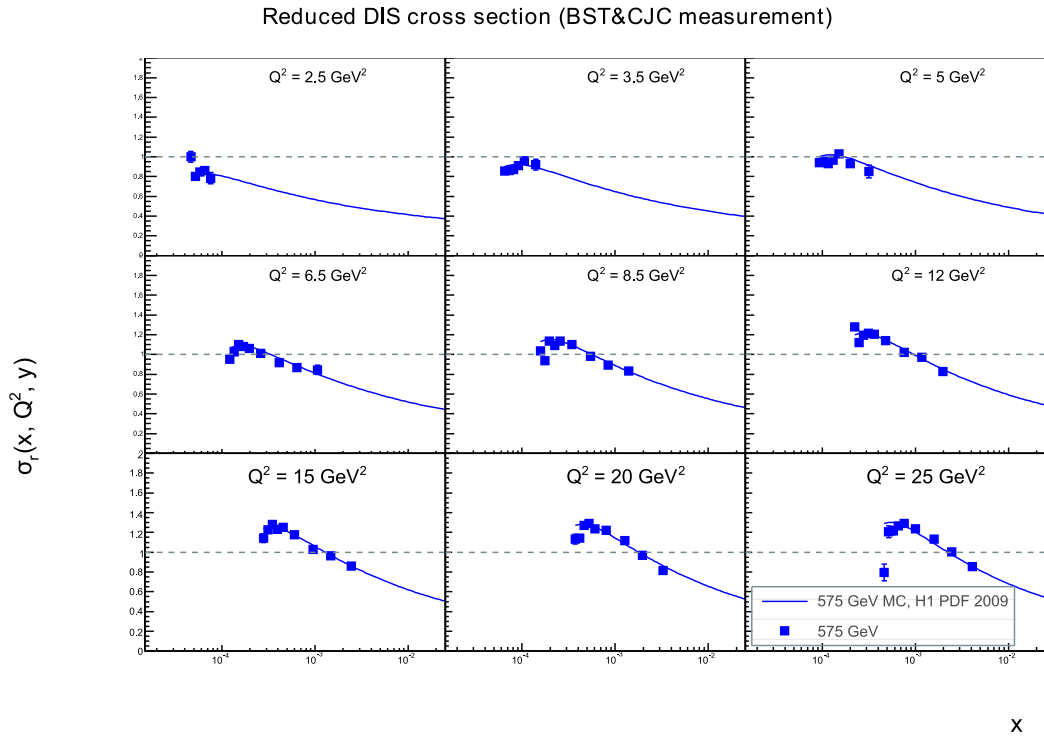


Figure 5.22: The measurement of the reduced cross section σ_r as a function of Bjorken- x for various Q^2 bins for the medium energy running period. The error bars represent the statistical uncertainties. The data is compared with the H1 PDF 2009 parameterization.

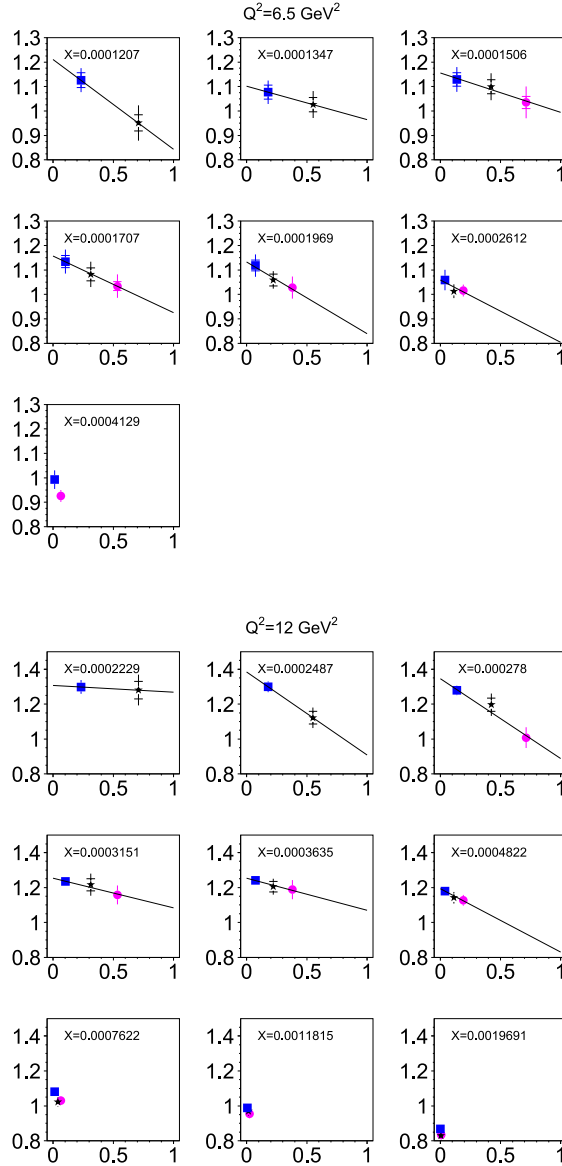


Figure 5.23: The reduced DIS cross section plotted as a function of y^2/Y_+ for different values of x at $Q^2 = 6.5 \text{ GeV}^2$ and $Q^2 = 12 \text{ GeV}^2$, measured for the proton beam energies of 920 (square), 575 (star) and 460 (circle) GeV. For the first six bins in x , which corresponds to large y , a straight line fit is shown. The y -intercept of the fit determines $F_2(x, Q^2)$, the slope of the fit determines $F_L(x, Q^2)$.

5 Data Selection and Treatment

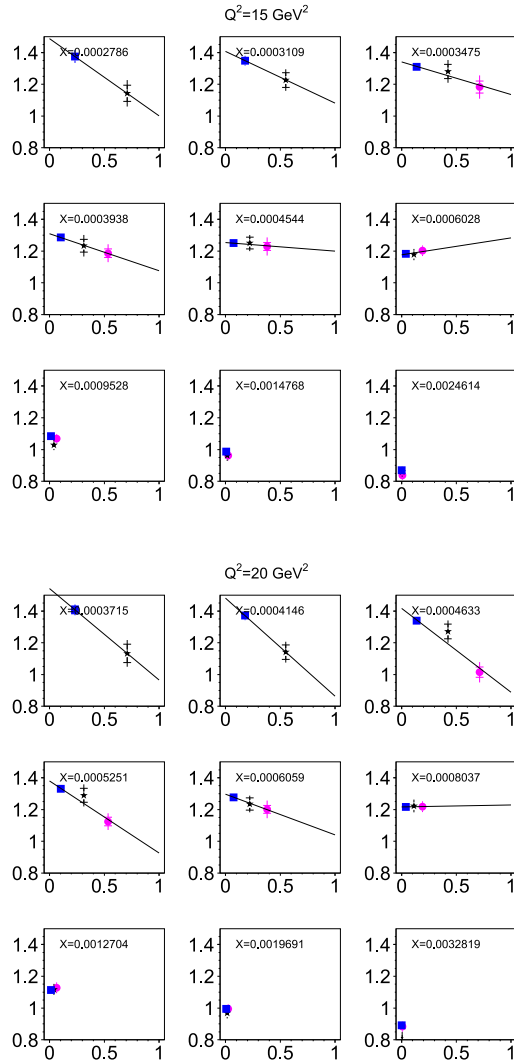


Figure 5.24: The reduced DIS cross section plotted as a function of y^2/Y_+ for different values of x at $Q^2 = 15 \text{ GeV}^2$ and $Q^2 = 25 \text{ GeV}^2$, measured for the proton beam energies of 920 (square), 575 (star) and 460 (circle) GeV. For the first six bins in x , which corresponds to large y , a straight line fit is shown. The y -intercept of the fit determines $F_2(x, Q^2)$, the slope of the fit determines $F_L(x, Q^2)$.

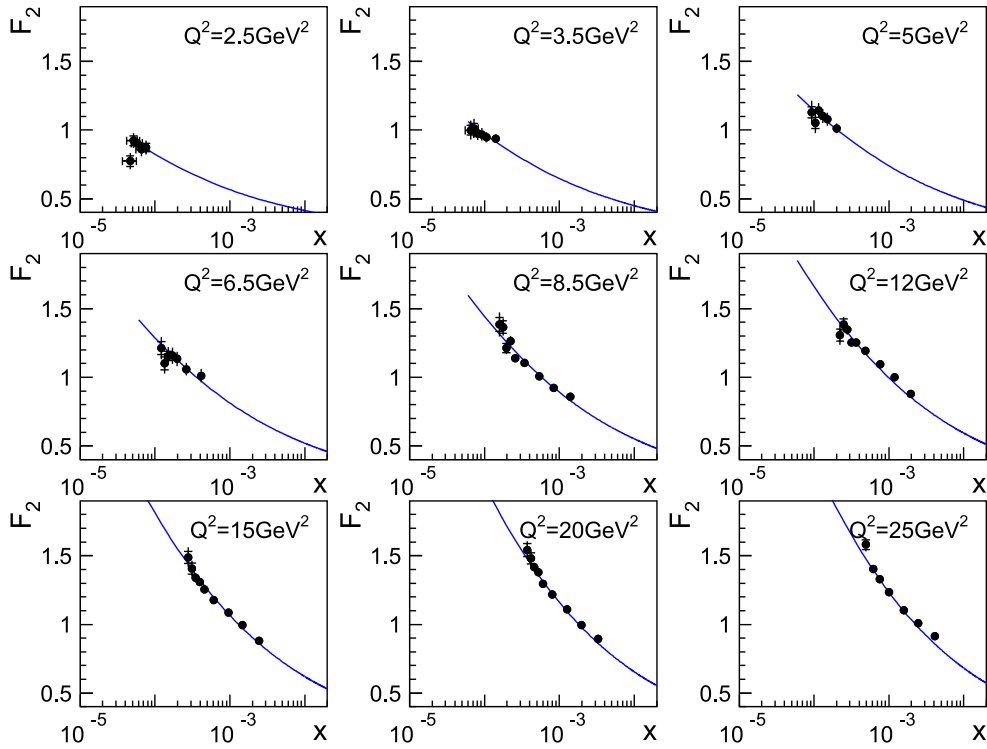


Figure 5.25: The proton structure function F_2 determined using the DIS cross section measurements for the three different centre-of-mass energies. The function is compared with the H1 PDF 2009 parameterization.

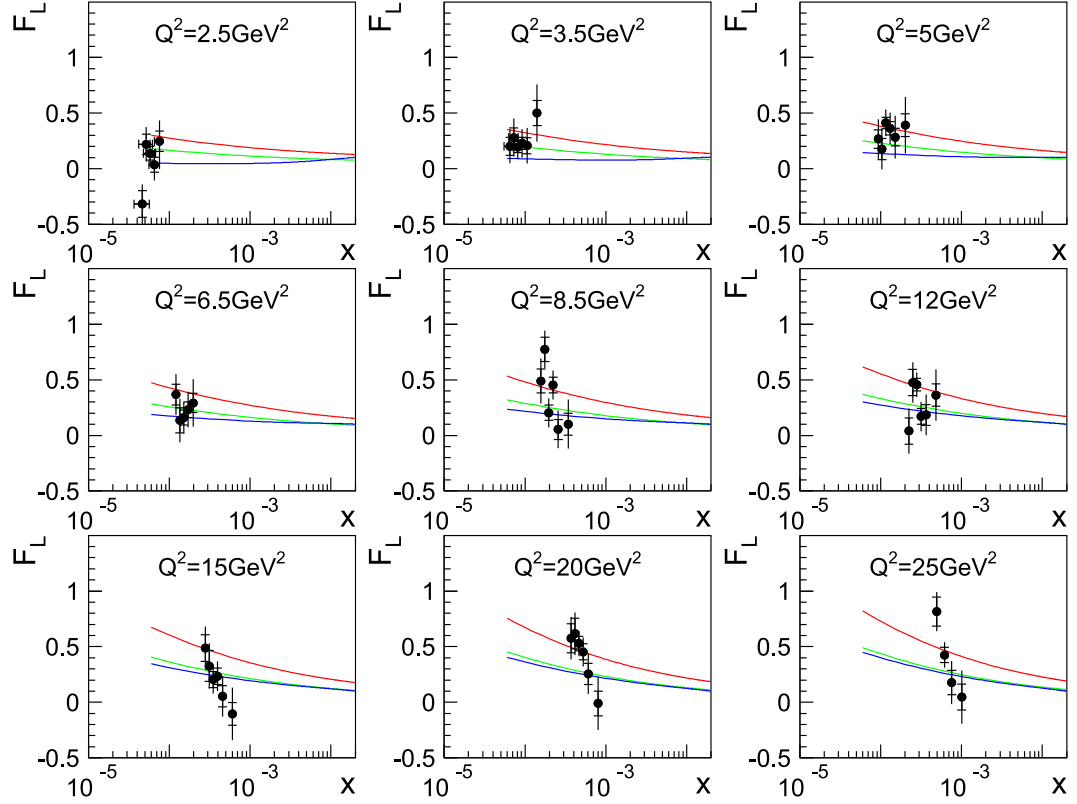


Figure 5.26: The longitudinal proton structure function $F_L(x, Q^2)$ for nine different Q^2 bins. The inner error bars denote the statistical errors. The full error bars depict the total uncertainty of the measurement. The blue curve represents the H1 PDF 2009 parameterization, the red one F_2 H1 PDF 2009 ($R = 0.5$), the green curve shows F_2 H1 PDF 2009 ($R = 0.25$).

6 Summary

In this thesis measurements of the inclusive e^+p neutral current deep-inelastic scattering cross section and the longitudinal proton structure function $F_L(x, Q^2)$ have been presented. The data used in the analysis were collected during special low energy running period in the year 2007, when two runs with lowered proton beam energies of $E_p = 460$ GeV and $E_p = 575$ GeV were taken. The measurements were performed in the range $2.5 \text{ GeV}^2 \leq Q^2 \leq 25 \text{ GeV}^2$.

The measurement of F_L is extended compared to the H1 publication [1] to low $2.5 \text{ GeV}^2 \leq Q^2 \leq 8.5 \text{ GeV}^2$ using the data from the Backward Silicon Tracker. A uniform analysis of cross section data became possible using BST/CJC electron finder developed for this measurement and described in the thesis. The finder permits efficient validation of the electron candidate and an accurate measurement of the electron candidate charge, which is used for the background estimation. The complete chain of the cross section analysis and the finder were integrated with the H1 experiment standard software.

The cross section measurements at different E_p were used to extract the structure functions F_2 and F_L using a linear fit (see chapter 2). This determines both functions without model assumptions. The measured structure functions are compared to the prediction obtained from H1 PDF 2009 fit. A good agreement is observed for F_2 .

The new measurement of the structure function F_L shows good consistency with NLO QCD for $Q^2 \geq 12 \text{ GeV}^2$ data. This provides an independent cross check of DGLAP validity for this range and ensures that gluon parton density extracted using DGLAP fits to F_2 data can be applied to other observables. The precise knowledge of the gluon density for $x \approx 0.005$, corresponding for HERA kinematics to $Q^2 > 10 \text{ GeV}^2$ range, is used for the prediction of W , Z as well as light Higgs production rates at the LHC. The measurements for $2.5 \text{ GeV}^2 \leq Q^2 \leq 8.5 \text{ GeV}^2$ access the region where the higher order QCD corrections become large and various models give different predictions [39]. The precision of the cross section measurement is on the level of 2-5% and the overall precision of the longitudinal proton structure function F_L determination is about 0.1.

Tables of the Experimental Results

Q^2 GeV ²	y	x	σ_r	δ_{stat} %	δ_{sys} %	δ_{tot} %	δ_{uncor} %	δ_{cor} %	$\gamma_{E'_e}$ %	γ_{θ_e} %	γ_{Had} %
2.5	0.85	5.79e-05	0.788	3.38	6.33	7.17	3.72	5.12	2.82	0.88	0.26
2.5	0.75	6.56e-05	0.8247	2.05	4.9	5.31	3.57	3.36	2.34	-0.83	0.22
2.5	0.65	7.57e-05	0.7651	1.78	5	5.3	4.16	2.77	0.21	-1.83	0.19
3.5	0.85	8.11e-05	0.8291	2.52	5.82	6.34	3.56	4.6	1.54	1.04	0.15
3.5	0.75	9.19e-05	0.828	1.67	4.27	4.58	3.38	2.6	1.15	0.81	0.18
3.5	0.65	0.000106	0.8386	1.54	4.19	4.47	3.4	2.45	1.3	-0.45	0.17
3.5	0.49	0.0001407	0.826	1.56	3.06	3.44	2.36	1.95	0.2	-0.19	0.15
5	0.85	0.0001158	0.8502	1.98	5.95	6.27	3.49	4.82	1.08	1.31	0.18
5	0.75	0.0001313	0.9014	1.59	4.32	4.6	3.32	2.76	1.13	1.31	0.18
5	0.65	0.0001515	0.9446	1.49	4.14	4.4	3.3	2.5	1.21	0.82	0.14
5	0.49	0.0002009	0.9287	1.13	2.08	2.37	1.86	0.94	0.68	-0.2	0.08
6.5	0.85	0.0001506	1.0144	2.46	5.88	6.37	3.5	4.72	0.88	1.16	0.2
6.5	0.75	0.0001707	1.0135	1.76	4.29	4.64	3.32	2.72	1.25	1.15	0.15
6.5	0.65	0.0001969	1.0078	1.52	4.12	4.39	3.28	2.49	0.58	1.33	0.17
6.5	0.49	0.0002612	0.9954	0.91	2.21	2.39	1.81	1.27	0.95	0.8	0.05
6.5	0.31	0.0004129	0.907	1.09	2.36	2.6	1.86	1.46	1.43	-0.31	0
8.5	0.85	0.0001969	1.042	2.74	6.49	7.04	3.49	5.47	2.23	0.42	0.19
8.5	0.75	0.0002232	1.0151	1.88	4.39	4.77	3.34	2.85	1.19	1.41	0.15
8.5	0.65	0.0002575	1.0895	1.69	4.11	4.44	3.29	2.45	0.87	1.09	0.18
8.5	0.49	0.0003416	1.0623	0.91	2.56	2.72	1.8	1.82	1.26	1.24	0.06
8.5	0.31	0.0005399	0.9876	0.93	2.49	2.66	1.82	1.71	1.31	1.1	0
8.5	0.2	0.0008369	0.8779	0.93	2.68	2.84	1.84	1.96	1.77	0.83	0
8.5	0.12	0.0013948	0.7897	1.01	2.66	2.85	1.89	1.87	1.81	0.49	0

Table 1: The reduced cross section σ_r for the low energy running period, as measured with the data sample for $2.5 \text{ GeV}^2 \leq Q^2 \leq 8.5 \text{ GeV}^2$. The uncertainties are quoted in per cent relative to σ_r . δ_{tot} is the total uncertainty determined as the quadratic sum of systematic and statistical uncertainties. $\gamma_{E'_e}$, γ_{θ_e} and γ_{Had} denote individual components of the total correlated systematic uncertainty and correspond respectively to the uncertainty on the electron energy scale, polar angle and hadronic scale.

Tables of the Experimental Results

Q^2 GeV ²	y	x	σ_r	δ_{stat} %	δ_{sys} %	δ_{tot} %	δ_{uncor} %	δ_{cor} %	$\gamma_{E'_e}$ %	γ_{θ_e} %	γ_{Had} %
12	0.85	0.000278	0.9874	2.34	5.51	5.99	3.49	4.26	1.31	1.05	0.15
12	0.75	0.0003151	1.1346	2.03	4.2	4.66	3.36	2.52	1.15	0.64	0.16
12	0.65	0.0003635	1.1647	1.88	4.29	4.68	3.31	2.72	0.44	1.75	0.22
12	0.49	0.0004822	1.1047	0.99	2.62	2.8	1.81	1.9	0.95	1.64	0.06
12	0.31	0.0007622	1.0099	0.92	2.4	2.57	1.81	1.57	1.04	1.18	0
12	0.2	0.0011815	0.936	0.92	2.62	2.77	1.83	1.88	1.67	0.86	0
12	0.12	0.0019691	0.8186	0.99	3.08	3.23	1.86	2.45	2.26	0.94	0
15	0.85	0.0003475	1.1593	3.19	5.34	6.22	3.59	3.96	1.95	1.09	0.16
15	0.75	0.0003938	1.1621	2.27	4.12	4.71	3.36	2.39	0.47	1.02	0.18
15	0.65	0.0004544	1.2045	2.07	4.21	4.69	3.34	2.55	1.24	0.92	0.21
15	0.49	0.0006028	1.1775	1.15	2.55	2.8	1.83	1.78	1.07	1.42	0.05
15	0.31	0.0009528	1.0479	1	2.59	2.78	1.82	1.84	1.12	1.46	0
15	0.2	0.0014768	0.9438	0.92	3.09	3.22	1.83	2.49	1.85	1.67	0
15	0.12	0.0024614	0.8217	0.91	3.31	3.43	1.86	2.74	2.21	1.62	0
20	0.85	0.0004633	0.9944	3.28	5.46	6.37	3.75	3.97	2.28	0.56	0.17
20	0.75	0.0005251	1.1014	2.38	4.04	4.69	3.37	2.22	0.55	0.57	0.18
20	0.65	0.0006059	1.1767	2.12	4.2	4.71	3.34	2.55	0.79	1.33	0.18
20	0.49	0.0008037	1.1936	1.27	2.47	2.78	1.84	1.64	0.78	1.44	0.03
20	0.31	0.0012704	1.1047	1.14	2.79	3.02	1.84	2.1	1.35	1.61	0
20	0.2	0.0019691	0.9753	1.04	2.75	2.94	1.85	2.04	1.26	1.6	0
20	0.12	0.0032819	0.8653	1.03	3.38	3.53	1.89	2.8	2.16	1.78	0
25	0.8	0.0006154	1.11744	3.03	4.13	5.12	3.43	2.29	0.58	0.77	0.16
25	0.65	0.0007574	1.2359	2.47	4.11	4.79	3.37	2.36	1.03	0.64	0.23
25	0.49	0.0010047	1.1995	1.32	2.44	2.77	1.85	1.59	1.13	1.06	0.08
25	0.31	0.001588	1.0937	1.27	2.89	3.16	1.87	2.21	1.6	1.52	0
25	0.2	0.0024614	0.982	1.18	2.81	3.05	1.88	2.09	1.29	1.64	0
25	0.12	0.0041023	0.8304	1.08	3.37	3.54	1.92	2.77	2.26	1.6	0
25	0.12	0.0041023	0.8304	1.08	3.37	3.54	1.92	2.77	2.26	1.6	0

Table 2: The reduced cross section σ_r for the low energy running period, as measured with the data sample for $12 \text{ GeV}^2 \leq Q^2 \leq 25 \text{ GeV}^2$. The uncertainties are quoted in per cent relative to σ_r . δ_{tot} is the total uncertainty determined as the quadratic sum of systematic and statistical uncertainties. $\gamma_{E'_e}$, γ_{θ_e} and γ_{Had} denote individual components of the total correlated systematic uncertainty and correspond respectively to the uncertainty on the electron energy scale, polar angle and hadronic scale.

Q^2 GeV ²	y	x	σ_r	δ_{stat} %	δ_{sys} %	δ_{tot} %	δ_{uncor} %	δ_{cor} %	$\gamma_{E'_e}$ %	γ_{θ_e} %	γ_{Had} %
2.5	0.848	4.64e-05	1.0003	5.36	5.78	7.89	3.73	4.43	2.05	0.43	0.2
2.5	0.76	5.18e-05	0.8017	3.32	4.9	5.92	3.67	3.26	2.28	-0.44	0.16
2.5	0.68	5.79e-05	0.8446	2.94	5.08	5.87	3.95	3.2	1.83	-1.59	0.27
3.5	0.848	6.5e-05	0.8563	3.67	5.88	6.93	3.57	4.67	2	1.52	0.22
3.5	0.76	7.25e-05	0.859	2.75	4.44	5.22	3.45	2.79	1.59	0.54	0.17
3.5	0.68	8.11e-05	0.8697	2.46	4.51	5.14	3.44	2.91	2.03	0.35	0.21
3.5	0.6	9.19e-05	0.9088	2.74	4.09	4.92	3.56	2.02	0.09	-0.05	0.14
3.5	0.52	0.000106	0.9578	3.56	4.59	5.81	3.04	3.44	2.55	2.3	0.18
5	0.848	9.29e-05	0.9412	3.07	6.35	7.05	3.52	5.28	2.36	0.83	0.23
5	0.76	0.0001036	0.9565	2.62	4.38	5.11	3.37	2.8	1.03	1.39	0.18
5	0.68	0.0001158	0.9314	2.35	4.14	4.76	3.33	2.46	1.21	0.66	0.2
5	0.6	0.0001313	0.9644	2.44	4.02	4.7	3.34	2.24	0.94	0.23	0.14
5	0.52	0.0001515	1.0304	2.65	2.65	3.75	2.03	1.71	1.35	-0.49	0.13
5	0.392	0.0002009	0.9312	2.29	2.61	3.47	2.01	1.67	1.62	-0.42	0
6.5	0.848	0.0001207	0.9505	3.47	6.74	7.58	3.52	5.75	1.34	1.24	0.15
6.5	0.76	0.0001347	1.0265	2.86	4.54	5.36	3.37	3.03	1.4	1.59	0.2
6.5	0.68	0.0001506	1.0992	2.6	4.29	5.02	3.32	2.72	0.95	1.55	0.15
6.5	0.6	0.0001707	1.0815	2.4	4.2	4.84	3.3	2.6	1.33	0.97	0.11
6.5	0.52	0.0001969	1.0594	2.23	2.5	3.35	1.95	1.57	1.1	0.9	0.06
6.5	0.392	0.0002612	1.0134	1.44	2.39	2.79	1.83	1.55	1.35	0.75	0
8.5	0.848	0.0001579	1.0373	3.92	6.79	7.84	3.51	5.81	1.02	0.95	0.22
8.5	0.76	0.0001762	0.9393	2.98	4.34	5.27	3.4	2.7	0.88	1.29	0.15
8.5	0.68	0.0001969	1.1361	2.89	4.4	5.26	3.34	2.86	1.27	1.57	0.2
8.5	0.6	0.0002232	1.0889	2.48	4.25	4.92	3.3	2.68	0.56	1.67	0.17
8.5	0.52	0.0002575	1.1363	2.31	2.49	3.39	1.93	1.57	0.71	1.39	0.1
8.5	0.392	0.0003416	1.0986	1.35	2.37	2.72	1.81	1.53	1.24	0.89	0
8.5	0.248	0.0005399	0.9801	1.37	2.42	2.78	1.83	1.59	1.35	0.83	0
8.5	0.16	0.0008369	0.8901	1.39	2.7	3.04	1.85	1.97	1.84	0.71	0
8.5	0.096	0.0013948	0.8345	2.06	3.98	4.49	2.1	3.38	3.38	0.22	0

Table 3: The reduced cross section σ_r for the medium energy running period, as measured with the data sample for $2.5 \text{ GeV}^2 \leq Q^2 \leq 8.5 \text{ GeV}^2$. The uncertainties are quoted in per cent relative to σ_r . δ_{tot} is the total uncertainty determined as the quadratic sum of systematic and statistical uncertainties. $\gamma_{E'_e}$, γ_{θ_e} and γ_{Had} denote individual components of the total correlated systematic uncertainty and correspond respectively to the uncertainty on the electron energy scale, polar angle and hadronic scale.

Tables of the Experimental Results

Q^2 GeV ²	y	x	σ_r	δ_{stat} %	δ_{sys} %	δ_{tot} %	δ_{uncor} %	δ_{cor} %	$\gamma_{E'_e}$ %	γ_{θ_e} %	γ_{Had} %
12	0.848	0.0002229	1.2796	3.93	5.67	6.9	3.5	4.46	1.61	1.22	0.19
12	0.76	0.0002487	1.1216	3.25	4.18	5.3	3.43	2.4	0.26	0.83	0.2
12	0.68	0.000278	1.1972	3.14	4.3	5.33	3.37	2.67	1.34	1.11	0.21
12	0.6	0.0003151	1.216	2.9	4.28	5.17	3.33	2.68	0.88	1.54	0.15
12	0.52	0.0003635	1.2051	2.53	2.82	3.79	1.96	2.03	0.75	1.3	0.04
12	0.392	0.0004822	1.1416	1.39	2.54	2.9	1.81	1.78	1.05	1.45	0
12	0.248	0.0007622	1.0227	1.33	2.39	2.73	1.82	1.55	1	1.18	0
12	0.16	0.0011815	0.9697	1.34	2.58	2.91	1.84	1.82	1.55	0.95	0
12	0.096	0.0019691	0.8296	2.22	3.71	4.33	2.03	3.11	2.71	1.53	0
15	0.848	0.0002786	1.1433	4.5	5.73	7.29	3.58	4.47	2.4	0.34	0.18
15	0.76	0.0003109	1.2273	3.77	4.11	5.58	3.41	2.29	0.19	0.84	0.23
15	0.68	0.0003475	1.2812	3.5	4.41	5.64	3.39	2.82	1.53	1.22	0.13
15	0.6	0.0003938	1.2334	3.21	4.46	5.5	3.37	2.92	1.34	1.63	0.16
15	0.52	0.0004544	1.2511	2.97	2.75	4.05	2	1.89	0.85	1.68	0.1
15	0.392	0.0006028	1.1777	1.55	2.55	2.98	1.82	1.78	1.09	1.41	0
15	0.248	0.0009528	1.0281	1.38	2.65	2.99	1.83	1.92	1.03	1.63	0
15	0.16	0.0014768	0.9619	1.32	3.18	3.45	1.84	2.6	1.76	1.92	0
15	0.096	0.0024614	0.8613	1.83	3.15	3.64	2.02	2.41	2.06	1.26	0
20	0.848	0.0003715	1.1329	5.08	5.38	7.39	3.74	3.86	1.97	0.91	0.11
20	0.76	0.0004146	1.1415	3.98	4.12	5.72	3.44	2.26	0.69	0.51	0.18
20	0.68	0.0004633	1.2715	3.65	4.16	5.53	3.39	2.41	0.8	1.03	0.2
20	0.6	0.0005251	1.2887	3.45	4.19	5.42	3.39	2.47	0.91	1.07	0.22
20	0.52	0.0006059	1.2349	3.18	2.87	4.28	2.06	2	0.94	1.76	0.08
20	0.392	0.0008037	1.2228	1.8	2.69	3.24	1.84	1.96	1.11	1.62	0
20	0.248	0.0012704	1.1168	1.61	2.71	3.15	1.85	1.98	1.14	1.62	0
20	0.16	0.0019691	0.9684	1.47	3.1	3.43	1.86	2.48	1.95	1.53	0
20	0.096	0.0032819	0.8139	1.97	3.78	4.26	2.07	3.16	2.46	1.98	0
25	0.8	0.0004923	1.07551	4.87	4.3	6.49	3.53	2.46	0.95	0.83	0.21
25	0.64	0.0006154	1.24667	2.75	4.07	4.91	3.39	2.24	0.42	0.88	0.17
25	0.52	0.0007574	1.2934	3.35	2.31	4.07	2.06	1.04	0.87	0.55	0.09
25	0.392	0.0010047	1.2356	1.93	2.52	3.17	1.86	1.69	0.69	1.54	0
25	0.248	0.001588	1.1322	1.85	2.91	3.45	1.88	2.22	1.62	1.52	0
25	0.16	0.0024614	1.0053	1.68	3.15	3.57	1.89	2.52	1.98	1.56	0
25	0.096	0.0041023	0.8535	1.98	3.38	3.92	2.15	2.6	1.94	1.73	0
25	0.096	0.0041023	0.8535	1.98	3.38	3.92	2.15	2.6	1.94	1.73	0

Table 4: The reduced cross section σ_r for the medium energy running period, as measured with the data sample for $12 \text{ GeV}^2 \leq Q^2 \leq 25 \text{ GeV}^2$. The uncertainties are quoted in per cent relative to σ_r . δ_{tot} is the total uncertainty determined as the quadratic sum of systematic and statistical uncertainties. $\gamma_{E'_e}$, γ_{θ_e} and γ_{Had} denote individual components of the total correlated systematic uncertainty and correspond respectively to the uncertainty on the electron energy scale, polar angle and hadronic scale.

Q^2 GeV ²	x	y	F_2	$\delta_{stat}^{F_2}$ %	$\delta_{tot}^{F_2}$ %	F_L	$\delta_{stat}^{F_L}$ %	$\delta_{tot}^{F_L}$ %
2.5	5.79e-05	0.850226	0.9031	2.71	5.19	0.1388	6.03	12.13
2.5	6.56e-05	0.750428	0.8603	2.79	5.27	0.0351	6.53	14.22
2.5	7.57e-05	0.650305	0.874	3.03	5.02	0.2453	9.12	18.82
3.5	8.11e-05	0.849807	0.9737	2.5	4.69	0.1946	5.19	11.15
3.5	9.19e-05	0.749938	0.9694	2.29	4.6	0.2273	5.49	12.71
3.5	0.000106	0.650182	0.9478	2.21	3.85	0.2062	7.27	16.14
3.5	0.0001407	0.489832	0.9389	1.49	3.25	0.5003	11.42	25.57
5	0.0001158	0.850226	1.1449	2.8	5.39	0.412	5.12	12.09
5	0.0001313	0.749857	1.1035	2.54	5.15	0.3614	6	14.16
5	0.0001515	0.649876	1.0786	2.37	4.82	0.2833	7.92	19.34
5	0.0002009	0.490076	1.0132	1.41	3.67	0.3911	10.15	25.53
6.5	0.0001506	0.849888	1.1553	3.31	6.35	0.1611	6.57	14.41
6.5	0.0001707	0.749813	1.1569	2.87	5.86	0.2319	7.04	16.06
6.5	0.0001969	0.650041	1.1334	2.58	5.33	0.2929	8.74	21.26
6.5	0.0002612	0.490019	1.0586	1.49	4.43	–	–	–
6.5	0.0004129	0.309986	1.0109	1.54	4.9	–	–	–
8.5	0.0001969	0.850054	1.2127	3.31	4.38	0.2037	6.92	13.1
8.5	0.0002232	0.74989	1.2646	2.86	3.61	0.4529	7.17	12.9
8.5	0.0002575	0.650002	1.1386	2.46	3.13	0.0534	9.06	16.91
8.5	0.0003416	0.489975	1.1054	1.4	2.17	0.1021	9.85	22.12
8.5	0.0005399	0.310012	1.0057	1.4	2.34	–	–	–
8.5	0.0008369	0.199995	0.9235	1.42	2.57	–	–	–
8.5	0.0013948	0.12	0.8571	1.54	3.05	–	–	–

Table 5: The proton structure functions $F_2(x, Q^2)$ and $F_L(x, Q^2)$ as measured with the data sample for $2.5 \text{ GeV}^2 \leq Q^2 \leq 8.5 \text{ GeV}^2$. The uncertainties are quoted in per cent. $\delta_{tot}^{F_2}$ and $\delta_{tot}^{F_L}$ are the total uncertainties determined as the quadratic sum of systematic and statistical uncertainties. The measurements of F_L with the total uncertainty higher than 30% are not listed in the table.

Tables of the Experimental Results

Q^2 GeV ²	x	y	F_2	$\delta_{stat}^{F_2}$ %	$\delta_{tot}^{F_2}$ %	F_L	$\delta_{stat}^{F_L}$ %	$\delta_{tot}^{F_L}$ %
12	0.000278	0.849982	1.3462	2.75	3.63	0.4572	5.63	10.98
12	0.0003151	0.749905	1.2541	2.46	3.2	0.1704	7.1	13.29
12	0.0003635	0.650055	1.2536	2.28	3.04	0.1849	9.38	18.22
12	0.0004822	0.490035	1.193	1.29	2.18	0.3631	9.92	23.17
12	0.0007622	0.310017	1.0934	1.25	2.26	–	–	–
12	0.0011815	0.199996	0.999	1.27	2.64	–	–	–
12	0.0019691	0.120002	0.8775	1.27	3.05	–	–	–
15	0.0003475	0.849982	1.3399	2.62	3.46	0.2042	7.2	12.53
15	0.0003938	0.750047	1.3094	2.18	3.01	0.2334	7.28	13.47
15	0.0004544	0.650019	1.2544	1.93	2.72	0.054	9.47	18.37
15	0.0006028	0.489994	1.1767	1.07	2.01	-0.1058	10.26	23.63
15	0.0009528	0.310001	1.087	1.06	2.2	–	–	–
15	0.0014768	0.200006	0.9941	1.06	2.53	–	–	–
15	0.0024614	0.12	0.8802	1.07	3.12	–	–	–
20	0.0004633	0.850043	1.4158	2.57	3.33	0.5279	6.62	11.34
20	0.0005251	0.75	1.3795	2.22	3.03	0.453	7.31	12.98
20	0.0006059	0.649983	1.2956	1.9	2.68	0.2552	9.43	18.19
20	0.0008037	0.490015	1.2174	1.03	1.99	-0.011	10.98	23.89
20	0.0012704	0.310001	1.1099	0.99	2.15	–	–	–
20	0.0019691	0.200002	0.9937	0.94	2.49	–	–	–
20	0.0032819	0.119999	0.8938	0.95	3.24	–	–	–
25	0.0006154	0.799937	1.4032	1.78	2.69	0.4247	6.88	11.54
25	0.0007574	0.649962	1.33	2.02	2.86	0.1776	11.03	19.28
25	0.0010047	0.489978	1.2349	1.09	2.02	0.0461	11.53	24.07
25	0.001588	0.310001	1.1019	1.05	2.14	–	–	–
25	0.0024614	0.2	1.0096	0.96	2.59	–	–	–
25	0.0041023	0.120001	0.9138	0.9	3.01	–	–	–

Table 6: The proton structure functions $F_2(x, Q^2)$ and $F_L(x, Q^2)$ as measured with the data sample for $12 \text{ GeV}^2 \leq Q^2 \leq 25 \text{ GeV}^2$. The uncertainties are quoted in per cent. $\delta_{tot}^{F_2}$ and $\delta_{tot}^{F_L}$ are the total uncertainties determined as the quadratic sum of systematic and statistical uncertainties. The measurements of F_L with the total uncertainty higher than 30% are not listed in the table.

Combined BST and CJC Electron Finder

The following chapter is devoted to the important task of the electron track reconstruction. The main selection criterion used in the present analysis is the existence of the track associated with the electron cluster in the SpaCal calorimeter. Furthermore, the sign of charge of the reconstructed track is used for the background determination. For these purposes a dedicated reconstruction submodule BCREC exploiting information from two independent tracking detectors BST and CJC has been designed and implemented as a part of the H1BSTREC module of the standard H1 reconstruction software HIREC. The algorithm has been used since 2007 and first results are available for DST4 data.

1 Motivation

In the backward region of the H1 detector two tracking subdetectors are typically used, these are the Central Jet Chamber and the Backward Silicon Tracker. The geometrical acceptance of the CJC is limited to the approximate range of $R_{SpaCal} \gtrsim 40$ cm. On the other hand the reliable measurements provided by the BST tracker are limited to $R_{SpaCal} \lesssim 30$ cm. Figure 1 depicts the track linking efficiency for the BST and CJC trackers as a function of radius in the SpaCal.

In the range of $R_{SpaCal} \gtrsim 40$ cm standalone CJC measurements are reliable with the high linking efficiency on the level of 90%. In the BST acceptance range the efficiency exceeds 80%. However in the transition range $30 \text{ cm} \lesssim R_{SpaCal} \lesssim 40$ cm considerable drop of the track linking efficiency is observed. To solve this problem the track reconstruction procedure combining information from both detectors has been developed.

In sum, the main motivation of the combined electron finder is to recover the observed efficiency drop and develop uniform tracking algorithm, which can be used in the full Θ_e range considered in this analysis.

2 Description of the Algorithm

The algorithm used in the BCREC module is a two step procedure, based on the method of deformable templates [40, 32]. In the first phase a circular fit to the hits, using the fast circle fitting procedure [25], is performed. As an output three parameters of the track are given, these are the track curvature κ , azimuthal angle ϕ and the distance to the closest approach DCA.

In the uniform magnetic field tracks are helices. Therefore in SZ plane, where S is the path along the track in the XY plane, tracks are straight lines. Typically the following

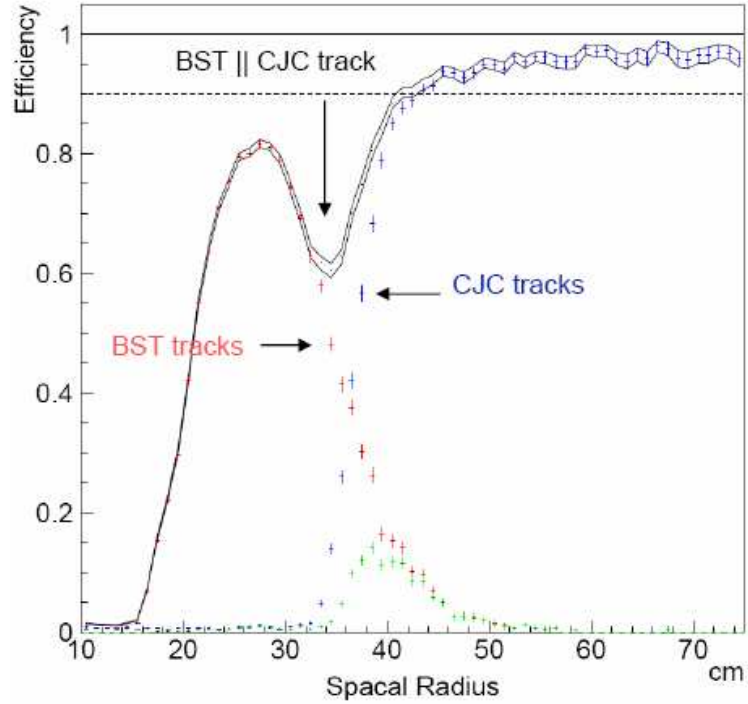


Figure 1: Track linking efficiency for the BST and the CJC plotted as a function of radius in SpaCal calorimeter. The blue histogram depicts the efficiency of the CJC, the red one of the BST. The green histogram denotes events where tracks are measured by both detectors.

parameterization is used:

$$Z(S) = Z_0 + a \cdot S, \quad (1)$$

where Z_0 is the Z position of the track at $S = 0$ and a is its slope. Remaining parameters of the trajectory (Θ and Z_0) are determined using the straight line fit in SZ plane. Eventually the main concern of the algorithm is the determination of the hits which belong to the track, i.e. are linked.

Usually several hits lie in the acceptance region around the track. Therefore it is not possible to determine immediately which space points belong to it. To deal with this problem for each space point i a probability W_i that it is produced by this track can be defined. The probability or weight should be greater for points lying closer to the current track. Distribution of the weight is assumed to be Gaussian with the width defined by

the track error σ_{track} . The weight of the point i can be defined as:

$$W_i^j \sim \exp\left(-\frac{D_{ij}^2}{T\sigma_j^2}\right). \quad (2)$$

Here D_{ij} is the distance from the space point i detected in the tracker $j \in (BST, CJC)$ to the current track approximation, parameter σ_j is the resolution of the detector j , T denotes the so-called temperature – a parameter which smears the value of the weight. Weights W_i are used in the track fit. After the fit one obtains an updated set of the track parameters with smaller errors. The temperature is decreased and the procedure is repeated until the temperature is less than some fixed value T_{final} . For the BCREC module the initial and final temperatures are taken to be 10000 and 0.004, respectively.

It is clear that the value of weight W_i should be smaller, if some other point in the wire (for CJC) or ϕ -sector (for BST) was already assigned to the track. This can be achieved by normalizing weights over all hits which belong to the wire or ϕ -sector. Moreover, to allow the possibility, when all the weights in the considered region are equal to 0, one should add so called cut-off parameter λ to the equation 2. Eventually the following formula for the space point weight is obtained:

$$W_i^j = \frac{\exp\left(-\frac{D_{ij}^2}{T\sigma_j^2}\right)}{\sum_{\alpha} \exp\left(-\frac{D_{i\alpha}^2}{T\sigma_j^2}\right) + \exp\left(-\frac{\lambda}{T}\right)}, \quad (3)$$

where the summation \sum_{α} is done for all space point in the considered region.

For the high temperatures weights of all space points are small, therefore track parameters obtained in the next iteration are not far from the initial approximation. At the end of each iteration the temperature T is reduced as $T/\Delta T$, where $\Delta T = 1.2$. For a fixed temperature weights of the space points are recalculated according to equation 3, afterwards the new track parameters are obtained. If the changes of the parameters of the trajectory are small enough, the procedure is stopped.

3 Implementation

As already mentioned the algorithm has been developed as a part of the H1BSTREC module of the H1REC package. It was implemented in C++ programming language [38], using containers and algorithms from the Standard Template Library [24].

The listing below outlines the main steps performed by the procedure in a C++-like notation:

```

1: T = T_init;
2: CalcInitialTrack();
3:
4: while ( T > T_final ) {
```

```

5:   RecalcPoints ();
6:   while( iter < Max_iter ) {
7:     RecalcBstW ();
8:     RecalcCjcW ();
9:     FitTrack ();
10:  }
11:  T = T / T_step;
12:  FitTrackFinal ();
13: }

```

At first stage the temperature $T = T_{init}$ satisfying the following condition:

$$T_{init} \approx \left(\frac{\sigma_{track}}{\sigma_{BST}} \right)^2, \quad (4)$$

where the parameters σ_{track} and σ_{BST} denote resolution of the track and the BST, respectively.

Subsequently procedure *CalcInitialTrack()*, responsible for the calculation of the initial approximation of the track parameters, is called. For the purposes of the current algorithm a straight line connecting SpaCal cluster with the vertex, determined by the central tracker, is used. Furthermore, the procedure *CalcInitialTrack()* is responsible for the determination of the event vertex weight used in the final fit, taking into account multiple scattering in the beam pipe.

The main part of the algorithm is a loop over temperatures (line 4 of the listing). A few tasks are performed in each iteration:

- coordinates of the space points are recalculated according to the current track approximation,
- for each temperature step internal loop, responsible for the hit linking, is executed. In each internal iteration weights of the space points are determined according to the distance from the current track (see equation 2), subsequently the track is refitted to the hits with non-zero weight. The internal loop is stopped if changes of the track parameters between iterations are small (i.e. linking procedure converged),
- the temperature is reduced according to the simple scheme: $T = T/T_{step}$,
- the final fit to the linked hits, the vertex and the SpaCal cluster is performed.

The result of the procedure are updated tracks and a list of linked hits. A hit is assumed to be linked to the track if its weight at the final temperature exceeds a fixed value $W_{point} > 0.5$. As an output of the BCREC module three BOS banks are produced, these are:

- **BCTR** – DCA parameters of the combined BST/CJC track with uncertainties and number of linked BST and CJC hits,

- **BCBH** – bit packed information about BST hits linked to the track (ϕ -sector, z -disk, strip number, etc.)
- **BCJH** – information about CJC hits linked to the track (CJC wire number, drift time, etc.).

4 Results and Comparisons

As mentioned in chapter 5, overall track linking efficiency of the algorithm was determined to be around 85% for the data and 92% for the Monte Carlo simulation. The efficiency in the transition region between BST and CJC is slightly below these values. This behaviour comes mainly from the relative misalignment between both detectors.

The algorithm showed stable behaviour for both the data and the Monte Carlo. It was observed that about 10 internal iterations are necessary for the hit linking loop to converge.

The performance of the algorithm has been compared with the standard reconstruction. Figure 2 depicts the correlation between Z_{vertex} position and Θ_e reconstructed according to the position of the electron cluster in the SpaCal calorimeter and by the combined BST/CJC finder. In general good agreement between both reconstruction schemes is observed, which confirms reasonable behaviour of the algorithm.

In figure 3 E_e/p distribution, with energy determined by the SpaCal calorimeter and the momentum of the electron measured by the combined finder, as a function of the electron energy E_e , is depicted. As expected the distribution shows peak at $E_{SpaCal}/p_{BST} = 1$ coming from the positive charge particles and a secondary peak at -1 corresponding to the negative charge. Tracks with the positive sign represent the DIS signal superimposed on positive background, while tracks with a negative charge correspond to almost pure background. Due to the good momentum resolution distributions for negative and positive charges are well separated, which allows for reliable background identification and subtraction.

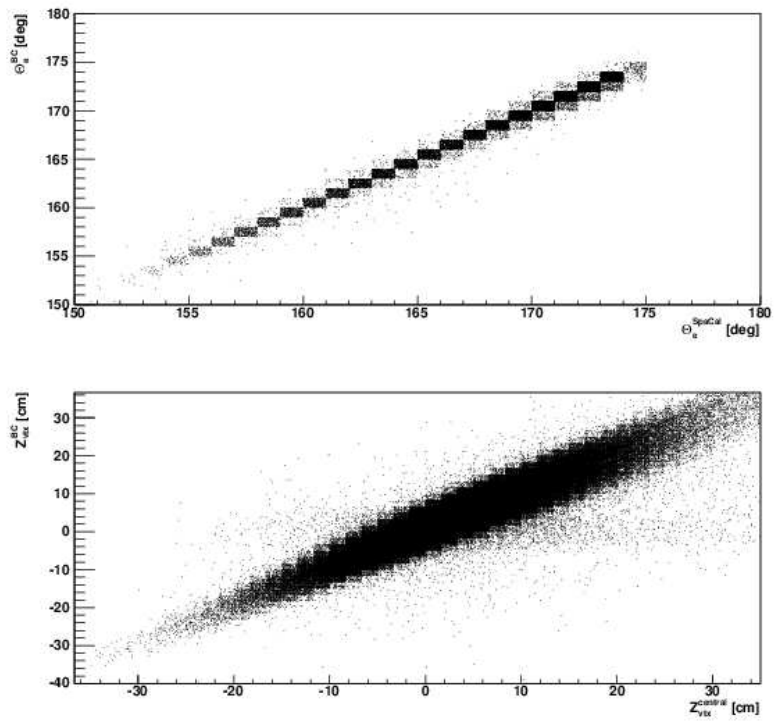


Figure 2: Correlation between Z_{vertex} , Θ_e reconstructed by the SpaCal and the combined BST/CJC finder.

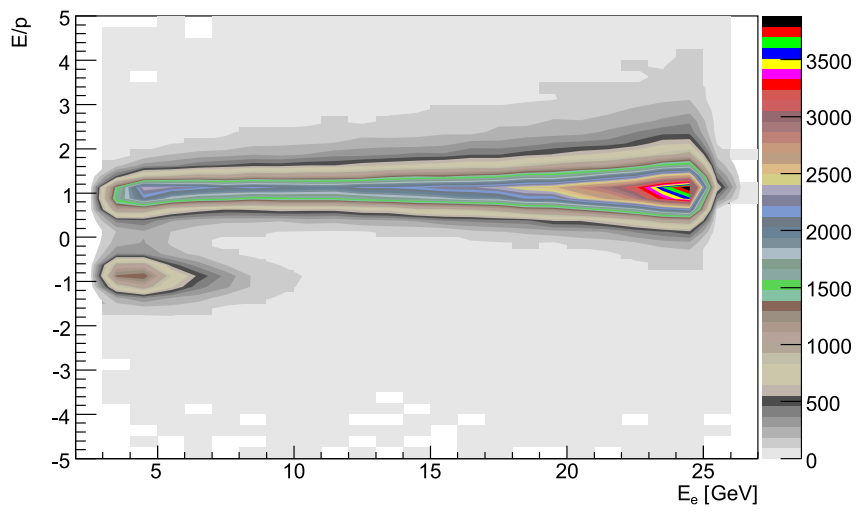


Figure 3: E/p distribution of energy over momentum for tracks linked to clusters in the SpaCal.

Bibliography

- [1] F. D. Aaron et al. Measurement of the Proton Structure Function $F_L(x, Q^2)$ at Low x . *Phys. Lett. B*, 665:139–146, 2008.
- [2] F. D. Aaron et al. Measurement of the Inclusive ep Scattering Cross Section at Low Q^2 and x at HERA. *Eur. Phys. J. C*, 63:625, 2009.
- [3] C. Adloff et al. Deep-Inelastic Inclusive ep Scattering at Low x and a Determination of α_s . *Eur. Phys. J. C*, 21:33, 2001.
- [4] C. Adloff et al. Measurement and QCD analysis of neutral and charged current cross sections at HERA. *Eur. Phys. J. C*, 30:1–32, 2003.
- [5] G. Altarelli and G. Parisi. Asymptotic Freedom In Parton Language. *Nucl. Phys. B*, 126:298, 1977.
- [6] B. Andersson et al. Coherence Effects in Deep Inelastic Scattering. *Z. Phys. C*, 43:625, 1989.
- [7] A. Arbuzov et al. HECTOR 1.00 - A program for the calculation of QED, QCD and electroweak corrections to ep and IN deep inelastic neutral and charged current scattering. *Comput. Phys. Commun.*, 94:128–184, 1996.
- [8] J. Bjorken. Applications of the Chiral $U(6) \otimes U(6)$ Algebra of Current Densities. *Phys. Rev.*, 148:1467, 1966.
- [9] J. D. Bjorken. Asymptotic Sum Rules at Infinite Momentum. *Phys. Rev.*, 179:1547–1553, 1969.
- [10] V. Blobel. The BOS System, 2001. A description available via <http://www.desy.de/~blobel>.
- [11] R. Brun et al. GEANT3 User's Guide. CERN, 1987.
- [12] A. Capella et al. Dual Parton Model. *Phys. Rept.*, 236:225–329, 1994.
- [13] Y. L. Dokshitzer. Calculation Of The Structure Functions For Deep Inelastic Scattering And e^+e^- Annihilation By Perturbation Theory In Quantum Chromodynamics (In Russian). *Sov. Phys. JETP*, 46:641, 1977.
- [14] R. Engel and J. Ranft. Hadronic Photon-Photon Interactions at High Energies. *Phys. Rev.*, D54:4244–4262, 1996.

Bibliography

- [15] H. Fesefeld. The Simulation of Hadronic Showers—Physics and Applications. RWTH Aachen, 1985.
- [16] R. P. Feynman. Very high-energy collisions of hadrons. *Phys. Rev. Lett.*, 23:1415–1417, 1969.
- [17] A. A. Glazov. *Measurement of the Proton Structure Function F_2 and F_L with the H1 Detector at HERA*. PhD thesis, Humboldt-Universität zu Berlin, 1998.
- [18] V. N. Gribov and L. N. Lipatov. Deep inelastic e p scattering in perturbation theory. *Sov. J. Nucl. Phys.*, 15:438, 1972.
- [19] G. Grindhammer, M. Rudowicz, and S. Peters. The Fast Simulation of Electromagnetic and Hadronic Showers. *Nucl. Instrum. Meth.*, A290:469, 1990.
- [20] G. Gustafson and U. Pettersson. Dipole Formulation of QCD Cascades. *Nucl. Phys.*, B306:746, 1988.
- [21] H1oo. H1oo System, 2009. A description available via <https://www-h1.desy.de/icas/oop/current/oo/>.
- [22] H1rec. H1rec System, 2009. A description available via <https://www-h1.desy.de/icas/manuals/h1rec/h1rec9/h1rec.html>.
- [23] L. N. Hand. Experimental investigation of pion electroproduction. *Phys. Rev.*, 129:1834–1846, 1963.
- [24] N. M. Josuttis. *The C++ Standard Library*. Addison-Wesley U.S.A., 1999.
- [25] V. Karimaki. Fast code to fit circular arcs, 1991. A description available via http://www.helsinki.fi/~seft_www/ps/hu_seft_91_10.ps.
- [26] J. Kretzschmar. *A Precision Measurement of the Proton Structure Function F_2 with the H1 Experiment*. PhD thesis, Humboldt-Universität zu Berlin, 2007.
- [27] J. Kretzschmar. F_2 at medium Q^2 and the PDF determination for H1 HERA I data, 2009. presented at DIS 2009, Madrid.
- [28] A. Kwiatkowski, H. Spiesberger, and H.-J. Mohring. HERACLES: an event generator for ep interactions at HERA energies including radiative processes. *Comp. Phys. Comm.*, 69:155, 1992.
- [29] L. Lönnblad. ARIADNE Version 4: A Program for Simulation of QCD Cascades Implementing the Color Dipole Model. *Comput. Phys. Commun.*, 71:15–31, 1992.
- [30] A. Mücke, R. Engel, J. P. Rachen, R. J. Protheroe, and T. Stanev. Monte Carlo Simulations of Photohadronic Processes in Astrophysics. *Comput. Phys. Commun.*, 124:290–314, 2000.

- [31] M. Nožička. *Forward Silicon Tracker of the H1 Experiment: Hardware and Study of D^* Meson Detection*. PhD thesis, Prague, Charles University, 2006.
- [32] M. Ohlsson. Track Finding with Deformable Templates - The Elastic Arms Approach. *Comput. Phys. Commun.*, 1991. Lund University Preprint LU TP 91-27.
- [33] M. Peez, B. Porthault, and S. E. An Energy Flow Algorithm for Hadronic Reconstruction In OO: Hadroo2. H1 Internal Note H1-01/05-616, 1999.
- [34] N. Raicevic. Charge Asymmetry. Presentation at the nELAN meeting, March 2009.
- [35] G. A. Schuler and H. Spiesberger. DJANGO: The Interface for the event generators HERACLES and LEPTO. In W. Buchmüller and G. Ingelman, editors, *Physics at HERA, vol. 3*, pages 1419–1432, 1991.
- [36] T. Sjöstrand. High-Energy Physics Event Generation with PYTHIA 5.7 and JETSET 7.4. *Comput. Phys. Commun.*, 82:74–90, 1994.
- [37] G. Sterman. Handbook of Perturbative QCD. *Rev. Mod. Phys.*, 67, 1995.
- [38] B. Stroustrup. *The C++ Programming Language (Special Edition)*. Addison-Wesley U.S.A., 2008.
- [39] R. Thorne. The Longitudinal Structure Function at HERA, 2009. presented at DIS 2008, London.
- [40] A. L. Yuille, T. Yang, and D. Geiger. Robust Statistics, Transparency and Correspondence. Harvard Robotics Laboratory Technical Report 90-7, 1990.

List of Figures

2.1	Feynman diagram of deep-inelastic electron-proton scattering	6
2.2	Data on F_2 from fixed target experiments and the HERA collider	11
2.3	The lowest order splitting functions for the DGLAP equations	12
2.4	Lowest order diagrams for the process $ep \rightarrow eX\gamma$	14
2.5	Cross section measurement	16
3.1	The HERA accelerator with the system of pre-accelerators	18
3.2	3D view of the H1 detector	20
3.3	The H1 Central Tracker	21
3.4	The Liquid Argon Calorimeter	24
3.5	The H1 trigger system	25
3.6	The backward section of the H1 experiment	27
3.7	Electromagnetic part of the SpaCal calorimeter	28
3.8	The Backward Silicon Tracker (BST)	32
3.9	The BST ϕ module	33
3.10	The BST wheel	34
3.11	BST Hit Finder	35
4.1	Kinematics coverage	40
4.2	A view of a high y event reconstructed in the H1 detector	43
4.3	E/p distribution	44
4.4	Charge asymmetry	46
4.5	Purity for the low energy running period	49
4.6	Stability for the low energy running period	50
4.7	Purity for the medium energy running period	51
4.8	Stability for the medium energy running period	52
5.1	Total luminosity provided by the HERA	54
5.2	Total luminosity collected by the H1	55
5.3	Event yield for the low energy running period	57
5.4	Event yield for the medium energy running period	58
5.5	The efficiency of the trigger $s0$	59
5.6	The inefficiency of the trigger $s8$	60
5.7	The inefficiency of the combination of triggers $s7$ and $s8$	60
5.8	SpaCal alignment check for the low energy running period	62
5.9	SpaCal alignment check for the medium energy running period	63
5.10	Distribution of hadronic fraction and cluster radius	65

List of Figures

5.11	Z_{vertex} reweighting	65
5.12	Mean of Z_{vertex} as a function of run number.	66
5.13	Spread of Z_{vertex} as a function of run number.	66
5.14	Distribution of cluster position in the SpaCal	68
5.15	Track link efficiency for the low energy running period	69
5.16	Track link efficiency for the medium energy running period	70
5.17	Control distributions for $E_p = 460$ GeV	75
5.18	Control distributions for $E_p = 460$ GeV	76
5.19	Control distributions for $E_p = 575$ GeV	77
5.20	Control distributions for $E_p = 575$ GeV	78
5.21	Reduced cross section for the low energy running period	79
5.22	Reduced cross section for the medium energy running period	80
5.23	Rosenbluth plots for $Q^2 = 6.5$ GeV and $Q^2 = 12$ GeV	81
5.24	Rosenbluth plots for $Q^2 = 15$ GeV and $Q^2 = 20$ GeV	82
5.25	The proton structure function F_2	83
5.26	The longitudinal proton structure function F_L	84
1	Track linking efficiency for BST and CJC	94
2	Z_{vertex} and Θ_e reconstructed by BCREC	98
3	E_e/p distribution as a function of energy in SpaCal	99

List of Tables

3.1	The HERA accelerator parameters	18
3.2	The geometrical parameters of the FST tracker	23
3.3	The geometrical parameters of the BST tracker	29
4.1	Tagged photoproduction events selection	45
4.2	Q^2 binning	47
4.3	y binning for the low energy running period	47
4.4	y binning for the medium energy running period	47
5.1	Data samples used in the analysis	54
5.2	Definition of subtriggers used in the analysis	57
5.3	QED Compton events selection	61
5.4	SpaCal alignment	61
5.5	Summary of the cuts used to select DIS events	63
5.6	Number of DIS events	64
5.7	Sources of systematic errors	72
5.8	Sources of systematic y -dependent errors	72
1	The reduced cross section for the low energy running period	87
2	The reduced cross section for the low energy running period	88
3	The reduced cross section for the medium energy running period	89
4	The reduced cross section for the medium energy running period	90
5	The proton structure functions $F_2(x, Q^2)$ and $F_L(x, Q^2)$	91
6	The proton structure functions $F_2(x, Q^2)$ and $F_L(x, Q^2)$	92

Acknowledgements

I want to thank Dr. Peter Kostka and Prof. Dr. Max Klein for the opportunity to work and study at DESY. I am deeply grateful to Dr. Alexander Glazov for his constant support, ideas, fruitful discussions and large contribution to the final results. This analysis would not be possible without his help. I would like to express my gratitude to Prof. Dr. Hermann Kolanoski who took the responsibility for my thesis and evaluated the work.

For a friendly atmosphere in the H1 Zeuthen group and help with various aspects of my work I owe thanks to Mirek Nožička, Jan Kretzschmar, Alexey Petrukhin, Ivan Glushkov, Sergey Gorbounov and Ilia Tsurin. I also wish to thank Jasna Perović for the friendship.

Many thanks to Ewelina Lobodzinska who first suggested me a possibility of writing PhD and for her help with many aspects of my stay in Germany. I also would like to thank Bogdan and Antonia for the adventurous cruise on the Baltic Sea.

I want to thank Olaf Behnke, Alan Campbell, Peter Kostka, Tim Namssoo and Eram Rizvi for their comments and suggestions on the draft of the thesis.

Wreszcie chcialbym podziekowac przyjaciolom za ich obecność w moim zyciu oraz rodzicom i siostrze za wsparcie i wiare we mnie.

Selbständigkeitserklärung

Hiermit erkläre ich, die vorliegende Arbeit selbständig ohne fremde Hilfe verfasst und nur die angegebene Literatur und Hilfsmittel verwendet zu haben.

Sebastian Piec
Hamburg, den 24.06.2009